MULTIMODAL INTRA- AND INTER-SUBJECT NONRIGID REGISTRATION OF SMALL ANIMAL IMAGES

By

Xia Li

Dissertation

Submitted to the Faculty of the

Graduate School of Vanderbilt University

in partial fulfillment of the requirements

for the degree of

DOCTOR OF PHILOSOPHY

in

Electrical Engineering

December, 2007

Nashville, Tennessee

Approved:

Professor Benoit M. Dawant

Professor J. Michael Fitzpatrick

Professor Thomas E. Yankeelov

Professor Bobby Bodenheimer

Professor John C. Gore

ACKNOWLEDGEMENTS

This dissertation would not have been possible without the great support and assistance from my professors and colleagues from the Medical Image Processing (MIP) lab and VUIIS. Many people have helped me and encouraged me consistently throughout these years to complete this work.

First of all, I would like to thank my advisors and mentors, Dr. Benoit Dawant and Dr. J. Michael Fitzpatrick, for their advice, encouragement, help, and patience. Dr. Dawant offered me the great opportunity to study at Vanderbilt University in 2002. Since then, he not only teaches me the research, but also shows me the way to analyze the research problems and the need to be persistent to accomplish the goals. In the past five and half years, he spent so many evenings and weekends to help me on my papers and projects. He always encourages me to try out new ideas and to solve challenging problem, with his excellent guidance and support. Dr. J. Michael Fitzpatrick gave me so many excellent lectures on medical imaging topics. It really helps me a lot for my research. Whenever help is needed either on my homework or research projects, he always extends the most helpful advice and assistance.

Special thanks to Dr. John Gore and Dr. Tom Yankeelov for their full support of my research. Without their continuous support, I would have not accomplished this study. They spent lots of time reading and commenting on my manuscripts and helping me solve the tough problems in my projects. Tom's passion and humor directly impact my life for the better. It is really great to keep working with them in the near future.

Finally, warm acknowledgement to Dr. Bobby Bodenheimer for his great support on both my projects and dissertation. His excellent suggestions since my doctoral

proposal stage really help me a lot and I sincerely thank him for his time and advice to me.

I also have a great time with all members of our Medical Image Processing lab. Many thanks to them for their friendship and help, especially to Rui Li, Yong Li, Ning Xu, Qingyang Shang.

I also would like to thank Lin Tang and Jing Wang for their wonderful friendship. They always care for me and help me, no matter how far apart we are.

Finally, I would like to express my deep gratitude to my parents and my beloved husband, Weiwei Qian. Their infinite love and support help me through a lot. They always give confidence to me. I love them.

TABLE OF CONTENTS

LIST OF FIGURES

LIST OF TABLES

Table Page

CHAPTER I

INTRODUCTION

According to the American Cancer Society, there will be approximately 559,650 cancer death in the United States in 2007, making it the second leading cause of premature death. Additionally, nearly 1.4 million people will develop some form of cancer next year. Beyond the devastating personal losses inflicted by cancer, the National Institutes of Health estimates that the overall costs for cancer in 2006 were $206.3 billion. Cancer is thus a major national (and international) health problem. As early detection greatly improves cancer outcome, in 1996 the National Cancer Institute (NCI) established the Diagnostic Imaging Program to encourage research into improving ways to detect and diagnose cancer noninvasively. The name of the program has changed twice during this time, from the Diagnostic Imaging Program to the Biomedical Imaging Program in 2001 and finally to the Cancer Imaging Program in 2003. As the Institute's website states: the mission of the Cancer Imaging Program is to promote and support cancer-related basic, translational and clinical research in imaging sciences and technology, and integration and application of these imaging discoveries and developments to the understanding of cancer biology and to the clinical management of cancer and cancer risk.

In order to support cancer-related research, various anatomical and functional imaging modalities have been developed. While current clinically employed imaging methods are most frequently used to report qualitative information (e.g., tumor location,

size, extent, etc.), imaging science has the potential to revolutionize medicine as it will ultimately provide quantitative, accurate, and noninvasive metrics on the underlying pathophysiology of tumor growth and treatment response. The major imaging modalities currently under investigation include ultrasound (US), magnetic resonance imaging (MRI), X-ray computed tomography (CT), positron emission tomography (PET), and single photon emission computed tomography (SPECT). Each of these methods has its own strengths: US is relatively fast, inexpensive, and can provide very high spatial resolution (~35 microns in small animals) of blood flow in 3D; MRI is extremely flexible offering high resolution (~100 microns) as well functional metrics on a variety of variables including blood flow, vessel permeability, tissue volume fractions, cell density, pH, and pO2; CT offers very high spatial resolution (35 microns) and can be used for angiography with an intravascular contrast agent; PET and SPECT have less spatial resolution (~1.5 mm) but are extremely sensitive and can report on, e.g., glucose metabolism and cell proliferation.

Since no one modality answers all the relevant questions concerning tumor status, methods which seek to combine the strengths of each modality are of great importance. For example, it could be very insightful to show how the US measure of blood flow correlates to the MRI measure of cell density and how these relate to the PET measure of glucose metabolism. To truly perform quantitative multi-modality cancer imaging studies, one would wish to consider all metrics obtained from all modalities simultaneously. To accomplish this goal, several registration issues must be considered.

First, inter-modality registration techniques need to be developed, tested, and automated. This is a non-trivial problem since, for example, the spatial resolution of the

above modalities spans almost two orders of magnitude. Moreover, different modalities show different image features. For example, CT images have low contrast between soft tissues and US images are affected by noise and artifacts. These issues make the registration task challenging. Second, if we consider the classic experimental design consisting of a control and treatment group, it is also of importance to see how these various metrics are changing between groups and therefore inter-subject registration methods need to be developed, tested, and automated. Inter-subject registration is more difficult than intra-subject registration, because of the large variations among subjects. The beauty of obtaining these metrics *via* noninvasive imaging is that this type of procedure can be done serially — especially in small animal models of cancer. Thus, longitudinal registration methods also need to be developed, tested, and automated. Since imaging methods are by their very nature indirect metrics of tumor status, they need to be validated by comparison to the gold-standard of histology. Thus, the final registration issue that needs to be addressed is the registration of stained histological sections with *in vivo* images. This issue is of significance because if the imaging metrics are shown to correspond to histology, they can be used as surrogate biomarkers of tumor status and therefore be employed in clinical trials with confidence.

1. Background on image registration

The work presented herein involves the following three registration tasks: registration of intra- and inter-subject tomographic head images, registration of tomographic images with histological images, and intra- and inter-subject registration of whole body tomographic images. A complete coverage of registration methods developed over the last

decade would be outside the scope of this document. The interested reader is referred to the chapter by Fitzpatrick et al. in the Handbook of Medical Imaging [1] or to the book by Hajnal [2]. However, to put our work within the appropriate context, we present a brief review of published methods for the major tasks that we will address.

1.1 Methods developed to register tomographic head images

As early as 1989, Pelizzari et al. [3] used a surface matching technique to register CT, MR, and PET head images. Henri et al. [5] proposed a method to integrate a projection angiogram and a translucent volume rendered CT or MR images, which created a composite of 3D anatomic and vascular images. Woods et al. [6] in 1993 proposed an automated algorithm to align MR and PET human brain images. This method aligned the images through minimizing the standard deviation of the PET pixel intensities that corresponded to MRI pixel intensities. In the same year, Mangin et al. [26] proposed an extension of the chamfer matching technique to align 3D PET and MRI data for human brain data. They used a shape-independent surface matching technique to compute the rigid body transformation. Elsen et al. [7] registered CT and MR brain images, through generating CT and MR feature images depicting 'ridgeness'. These feature images can be matched using an automatic hierarchical correlation scheme. Yan et al. [8] proposed a surface based registration algorithm which combined the minimization of average point-to-surface distance and iterative principal axes fitting, for MR and PET brain images, in 1994. Hui et al. [9] proposed a 3D MRI-PET brain image registration algorithm, in 1994, which was based on the matching of feature curves defined by the intersections of the interhemispherical fissure plane and the skull surface. Ardekani et al. [10] presented an automatic algorithm for

multimodality image registration that relied on minimizing the K-means variance criterion in 1995. Phohjonen et al. [15] developed a method to register 99mTc-hexamethylpropyleneamine oxime SPECT and 1.0 T MRI of the brain in 1996. This registration algorithm followed a noniterative least-squares method using singular value decomposition of a 3 × 3 covariance matrix. Both Wells et al. [12][13] and Maes et al. [14] used Mutual Information (MI) as a similarity measure between images to be registered. Following the registration validation project headed by Fitzpatrick at Vanderbilt [99], MI has become the most popular similarity measure for rigid body registration problems. Studholme et al. [17] also evaluated five similarity measures in 1997: cross correlation, minimization of corresponding PET intensity variation, moments of the distribution of values in the intensity feature space, entropy of the intensity feature space and mutual information, and showed that MI was the most robust measure among those for multimodal registration. Meyer et al. [18] evaluated the MI algorithms for a broad spectrum of multimodal volume data sets. In 1998, Thirion et al. [87] proposed a nonrigid registration algorithm, called the demons algorithm, to register the inter-patient MR brain images. Pluim et al. [22] proposed an algorithm in 2000, which combines MI and gradient information. In this study, the registration algorithm was evaluated for MR-T_1 and T_2, MR-T_1 and CT, MR-T_1 and PET registration tasks. The following year, Rohr et al. [21] presented an approximating thin-plate spline algorithm based on a set of corresponding anatomical point landmarks. This algorithm took into account landmark localization errors and could cope with isotropic and anisotropic landmark errors. This algorithm was used in MR-CT human brain image registration. Guimond et al. [88] also used the demons algorithm, combined with the correction of differences between images. They showed results obtained on several

imaging modalities, i.e., T_1 and T_2 MR images, proton density (PD) MR, and CT images. Both [87] and [88] used a stationary Gaussian filter to smooth the deformation field after each iteration of the demons registration algorithm. Christensen et al. [89] presented a consistent image registration algorithm. Just as its name implies, this algorithm estimated the forward and reverse transformations jointly, and produced a consistent transformation that have low pairwise registration errors. Hellier et al. [90] presented a nonrigid registration method, based on a 3D estimation of the optical flow. This algorithm modified the cost function to include a brightness constancy constraint term and a smoothness term. This method was used for inter-subject registration of T1-weighted MR images. Rueckert et al. [48] proposed a nonrigid registration algorithm, which was based on Free-Form Deformations (FFD), to maximize the normalized mutual information between breast MR images. In this algorithm, the second derivative of the deformation field was added to the cost function to constrain the transformation to be smooth. They also applied the algorithm to MR brain images [91]. Rohde et al. [59] proposed the Adaptive Basis Algorithm (ABA), in which the combination of basis functions was used to estimate the deformation field through maximizing the normalized mutual information. The regularization of deformation field was kept through constraining the difference between the coefficients of adjacent basis function. Others have used elastic [92][93][94] or fluid [95][96] transformations to register brain images. Both of these models were nonparametric and derived from the theory of elasticity and deformation. In those models, the image is an elastic grid, and an external force and an internal force were both applied to the image grid. Related work also includes the one proposed by Periaswamy et al. [25]. These authors modeled the transformation between images as locally affine but globally smooth, using a general-purpose elastic

registration algorithm. This algorithm incorporated both a geometric and intensity transformation, and was used for MRI T_1/T_2, MRI-T_1/MRI-Proton Density, photograph/MRI-T_2, and CT/photograph.

The aforementioned methods have been mostly applied to human data but they also start to be applied to small animal images. For instance, Vaquero et al. [23] evaluated the automated image registration (AIR) of Woods *at al.* [53] with a mutual information (MI) similarity measure to register PET images of the rat skull and brain to CT or MR images of the same animal. Hayakawa et al. [20] modified the algorithm proposed by Ardekani et al. [10] to register PET and MR images of rat brains.

As this brief review suggests, a large body of work exists that aims at automating the registration of head images. In our opinion, rigid body registration of head images is a relatively mature area and the most successful methods rely on some variation of voxel intensity similarity measure and more specifically on mutual information. The non-rigid registration problem remains more open and an active area of research.

1.2 Methods developed to register histological images with tomographic images

Despite great advances in *in vivo* imaging technology, the spatial resolution of histological images remains unmatched. There is thus great interest in combining information gathered from histology with *in vivo* information provided by MR, CT, or PET imagers. Several methods have been proposed. Some of these relied on a manual, interactive alignment [27][28][29] of these images, which is not practical. Others used features extracted from the images, such as the contour of the histological slices [31][32][33]. But a large amount of information included inside the images was ignored

in this type of approaches. Goldszal et al. [30] created a marker that can be used for registration by sticking needles in the structure before cutting. Then they used a fiducial-based registration algorithm to align the objects. Ali et al. [34] used a set of local absolute affine invariants to register histological coronal 2D rat brain images with a 3D rat brain atlas. These invariants were derived from a set of ordered inflection points on the external contour. Ourselin et al. [35][36] proposed a strategy, called a blockmatching algorithm, to compute the local transformation for several small windows in the histological images, to estimate the global rigid transformation. Mega et al. [38] co-registered a stained whole-brain sections to premortem fluorodeoxyglucose positron emission tomography (FDG-PET) using an elastic warping algorithm proposed by Thompson et al. [39]. Ourselin et al. [40] also used the blockmatching algorithm to fuse the histological sections with MR images. They used the same algorithm for the reconstruction of histological volumes and the registration of histological images with MRI. Bardinet et al. [41] presented a method for the registration of reconstructed post mortem optical data with MR scans. A rigid Iterative Closest Point (ICP) was first performed between the brain surface extracted from both the MR and an optical volume. Then 3D affine registration was used, using a variant of the correlation ratio as the similarity measure. Bardinet et al. [42] also presented a study for the registration of histological, optical and MR data of the human brain. In this study, the blockmatching algorithm and the feature-based registration algorithm were used. Gefen et al. [43] proposed a 3D wavelet-based algorithm for nonlinear registration. In this work, an elastic body model was used for the rat brain and a multi-resolution wavelet expansion is used to represent the deformation field. A cost function that includes the sum of squared surface distances and the elastic energy was

minimized to calculate the deformation field. Malandain et al. [54] followed the scheme presented by Ourselin et al. [35] to realign 2D autoradiographic sections. The authors also provided an intensity correction method for the reconstructed autoradiographic volumes. Chakravarty et al. [44] used the Automatic Nonlinear Image Matching and Anatomical Labeling (ANIMAL) registration scheme to reconstruct the histological volume. Auer et al. [45] presented an automatic nonrigid registration method for stained histological sections. The mutual information was used as the similarity measure for the rigid body registration algorithm and the nonrigid transformation was based on the elastic thin-plate spline (TPS) interpolations. Nevertheless, the TPS algorithm was sensitive to the control points and the mis-conrrespondence of the points would have a very negative influence on the registration result. Moreover, the work did not show any reconstruction result for the multiple stained slices. Arsigny et al. [46] recently proposed a novel geometrical transformation, called polyrigid and polyaffine, for the registration of histological slices. Using this transformation, large rigid or affine movements can be described. A differential equation averaged the influence of rigid or affine components. Hence, the displacement can be defined by a continuous trajectory. Yushkevich et al. [61] applied the approach in which the histological volume was reconstructed through fine-scale alignment, and the MRI and the histological volume were registered through coarse-scale alignment. The coarse and fine approaches were then combined to produce a coarse-to-fine reconstruction. However, several parameters in this algorithm must be determined empirically and finding the optimal values for these parameters was a hard task. In general, the most promising approaches follow a procedure similar to the one proposed by Ourselin et al. [35][36]. Chapter II describes this approach in more detail.

In addition to the reconstruction of the histological volumes, the creation of an atlas is of great importance. Atlases can be constructed so that anatomical data obtained from multiple specimens can be quantitatively compared to understand both normal (i.e., inter-specimen) variability as well as pathological states within an organ of interest. Atlases can provide a framework to synthesize structure and function at multiple scales and characterize inter- and intra-animal variation, thereby providing new insights into biology. In particular, brain atlases have added much to our knowledge of brain development, connectivity, and function, especially in determining the relationships between genotype and phenotype. Thus, there is great and continued interest in developing methods for improving methods to construct and analyze brain atlases.

So far, only a limited amount of literature can be found on the generation of mice brain histological atlas and small animal atlas-based segmentation approaches. MacKenzie-Graham et al. [69] developed a digital atlas of the adult C57BL/6J mouse brain as a comprehensive framework for the mouse brain. Several different imaging techniques, i.e., magnetic resonance microscopy, blockface imaging, classical histology and immunohistochemistry, were used to construct the mouse brain atlas. Regarding the image processing, they applied the blockmatching algorithm proposed by Ourselin et al. [35][36] to register two image volumes. Bock et al. [86] created a MRI mouse brain atlas to segment different tissues in the brains. Two different types of mice were compared through analyzing their tissues. Chakravarty et al. [44] created a brain atlas using serial histological data. Chan et al. [67] built a surgical atlas of the murine head through aligning a mouse brain MR and the corresponding CT images. However, none of these efforts creates an atlas of histology using the multiple individual histological volumes. Their “atlas”

came from only one single subject and can not reflect the characteristic of one certain population. Ma et al. [68] developed a 3D digital atlas for the C57BL/6J mouse brains, based on averaging multiple MR mouse brain images. Although the excellent results were presented in the work introduced above, the creation of histological atlas remains lacking.

In summary, a review of the current literature shows that registering tomographic images with histological images has been done but also that the process is not as straightforward as registering tomographic images alone. The reconstructed histological volumes, which are part of this process, often suffer from a number of artifacts generated during the staining procedure. Moreover, the creation of a histological atlas for the histology is still an active area of research. Chapter II of this thesis proposes solutions for these difficulties.

1.3 Methods developed to register whole body tomographic images

The main difference between head and whole body images is that the former typically contain a few structures (the brain and skull) while the latter contain a combination of articulated structures (the bones) and soft tissue, which complicates the problem. Non-rigid registration methods have been proposed for specific applications outside the head such as the registration of breast, abdomen, lung, or prostate images. Kramer et al. [4] used external and internal markers for CT and SPECT using radio-labeled, anti-carcinoembryonic antigen monoclonal antibody (MoAb) to fuse these types of images, which were obtained from eight subjects with suspected colorectal adenocarcinoma. Yu et al. [11] conducted a study to develop an accurate, retrospectively applicable procedure

for registering thoracic studies from different modalities in a short amount of time and with minimal operator intervention. In this paper, a sum of least squares fitting approach for the pleural surfaces was used for the registration of CT and PET images. Pereault et al. [16] adapted a superimposition method to the nonrigid thoraco-abdominal region from SPECT and CT slices, in order to detect tumor sites. Chow et al. [19] proposed an improved Genetic algorithm for finding the transformation between two free-form partially overlapping surfaces. This method was validated in the human heart model, human vertebrae model and fetus model. Mattes et al. [24] combined a rigid body deformation with localized cubic B-splines to capture the significant nonrigid motion in the chest between PET and CT images, using the mutual information as a similarity criterion. Rueckert et al. [48] used a non-rigid registration algorithm for breast MR images. They model the global motion with an affine transformation and describe the local breast motion with a free-form deformation (FFD) based on B-splines. Camara et al. [47] used free-form deformation guided by a gradient vector flow combined with a grey-level MI non-linear registration algorithm for thoracic and abdominal applications.

However, the registration of whole body images, and especially of small animal whole body images, remains a challenge. This is so because non-rigid registration methods typically need to be initialized with a rigid body transformation. Because whole body images contain many articulated joints and because it is extremely difficult to reposition small animals from acquisition to acquisition, a single rigid body transformation is typically insufficient for this initialization step. Despite these difficulties, several approaches have been proposed to partially address the problem ([49][50][51][52][72][73][78]). Chapter III of this thesis proposes a method to automatically register whole body images and a detailed

discussion of these papers will be presented in this chapter. In summary, registration of whole body images, including head images, can range from easy to very difficult, depending on the image acquisition procedure. For the whole body images, if the animal is positioned in a holder and the various imaging modalities can be acquired within the same holder, a simple rigid body registration method may be sufficient. Fig. 1 shows results we have obtained when registering CT and PET images of a mouse kept in the same holder in both scanners. However, if the animal can not be kept in the same holder, or if images are acquired longitudinally, the problem is more difficult. The goal of this work is to provide solutions to these problems. In the next sections we will summarize our main goals and contributions.

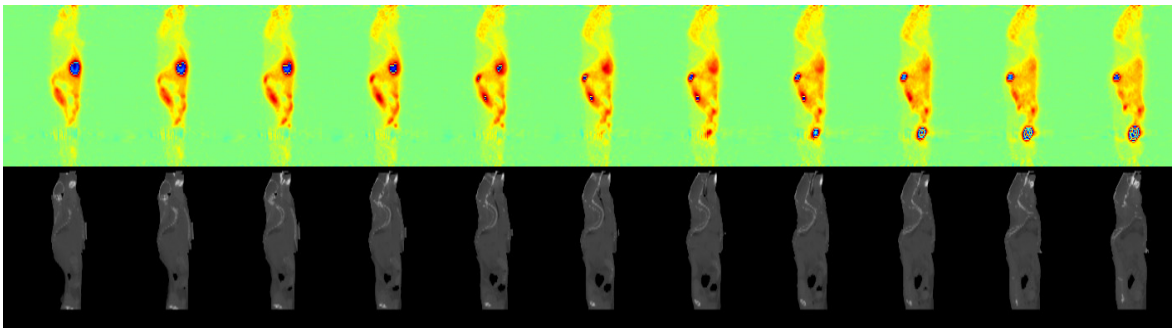

Fig. 1: PET and CT mouse whole body registration.

2. Goals and Contributions

As discussed above, a large body of work exists that deals with various aspects of medical image registration, but the vast majority of this work focuses on images from humans and, more specifically, on head images. While registering tomographic head images is of great importance for neuroimaging studies, it is also one of the easiest registration problems. This is so because the head is enclosed in the skull, which greatly

minimizes the amount of deformation observable between subjects. Also, when dealing with intra-subject registration problems, a rigid-body registration transformation is often sufficient. This further simplifies the problem. However, whole body registration problem remains a challenge because one single rigid body registration is insufficient for the registration of articulated structures. Hence, the overarching goal of the work presented herein is to adapt, modify, extend, and evaluate current registration methods to develop techniques applicable to the rigid and non-rigid registration of whole body small animal images.

The main contributions of this research are as follows.

We propose a solution to enhance the histological volumes reconstructed from 2D histological slices through averaging individual histological volumes. Histological images are usually considered as the gold standard, which is used to complement and/or validate the *in vivo* data. Automatic registration of the histology and other imaging modalities is a critical component of the overall analysis process. Due to the acquisition procedure of histological images, reconstruction of 3D volumes from a series of 2D images is required. A number of methods have been proposed recently in the literature to address this issue, but deformation or tearing during the slicing process often produces reconstructed volumes with visible artifacts and imperfections. In this work, we present a solution to this problem, through working with several histological volumes, reconstructing each of these separately, and then computing an average. We also propose an original and robust approach to normalize intensity values across slices, a required pre-processing step when reconstructing histological volumes. Finally, we use the histological volumes we have created to validate segmentation results obtained with an atlas-based method that uses

only MR volumes. The accuracy of the segmentation results we obtain demonstrates that automatic segmentation of brain structures and substructures in brain MR images of small animal is achievable.

Next, we present a fully automatic registration algorithm for whole body computed tomography volumes. Whole body images typically contain a large number of articulated structures, which makes registration more difficult. This study proposes a new method for the automatic registration of whole body CT images, which consists of two main steps. Skeletons are first brought into approximate correspondence with a robust point-based method. Transformations so obtained are refined with an intensity-based nonrigid registration algorithm that includes spatial adaptation of the transformation's stiffness. The approach has been applied to whole body CT images of mice, to CT images of the human upper torso, and to human head and neck CT images. To validate our method on soft tissue structures, which are difficult to see in CT images, we use co-registered MR images. We demonstrate that the approach we propose can successfully register image volumes even when these volumes are very different in size and shape or they have been acquired with the subjects in different positions.

Although the aforementioned algorithm provides acceptable results, it also suffers from one weakness: bones can be deformed inaccurately under the influence of surrounding soft tissues. Our final contribution is to propose a solution to this problem.

3. Overview

This chapter introduced the significance and the background and related work of our research. The main goals and contributions are also summarized. The reminder of the

thesis is organized as follows. Chapter II presents the methods we propose to reconstruct 3D histological volumes, to eliminate or reduce artifacts in each of the reconstructed volumes, and to build a virtual histological volume that is better than any of the volumes used to build it. Chapter III details our new algorithm for whole body image registration. Qualitative and quantitative validations are also provided. Chapter IV presents a modified algorithm for the whole body image registration, which solves the bone deformation problem. Chapter V concludes the work presented in this thesis and provides possible directions for future work.

CHAPTER II

ENHANCEMENT OF HISTOLOGICAL VOLUMES THROUGH AVERAGING AND THEIR USE FOR THE VALIDATION OF ATLAS-BASED SEGMENTATION METHODS

1. Introduction

Intra- and inter-subject registrations of medical images are important for a number of applications including assessment of therapy response, population comparison, or atlas-based segmentation. Moreover, the development of various imaging modalities such as ultrasound, magnetic resonance imaging, X-ray computed tomography, positron emission tomography, single photon emission computed tomography, or histology, each with its own strengths, demands the development of methods by which the information they provide can be combined.

A number of methods have been proposed to register tomographic images, especially human head images (see, for instance, [9][17][21][23][53]), which can be adapted to small animal images. Registering the histological images, which display a level of anatomical details far superior to the other imaging modalities, does, however, require first creating a 3D volume from a series of 2D images. Several authors have proposed semi-automatic methods to reconstruct these histological volumes (see, for instance, [27][29][31][32][33]). In general, the most promising approaches follow a procedure similar to the one proposed by Ourselin et al. [35] or Malandain et al. [54]. Sequential 2D images are first registered to each other using a 2D registration algorithm, intensities are normalized, and the 3D histological volume is registered to the corresponding tomographic volume, which is generally an MR volume. Because registering sequential 2D histological

volumes to each other may result in a brain whose shape is different from the true shape, a series of 2D and 3D registration steps are used to register the histological volume to the tomographic volume. First, a 3D transformation is computed and the two volumes are registered to each other. Then, the tomographic volume is resampled to correspond to the histological slices. Next, each histological slice is registered in 2D to its corresponding MR image in the resampled volume. A new histological volume is subsequently created and the process is repeated until convergence. In this paper, we use a similar strategy for the reconstruction of individual histological volumes with some variations that will be described in the methods section.

Intensity normalization is required because individual slices can absorb more or less of a particular histological stain during the slice preparation. Because of this, the overall intensity and contrast of these slices can vary. A number of algorithms of varying complexity have been proposed to address this problem. For instance, Dauguet et al. [63] rely on a segmentation of the images into several classes and the mapping of intensities for each class between slices. Segmentation is performed based on peaks detected in the intensity histograms of each slice following scale-space analysis. It requires a number of heuristics developed for their application (baboon brain images). In [44], Chakravarty et al. use a two-step process in which images are first normalized globally using third order polynomials to fit histograms of adjacent slices. The second step involves the computation of local scaling factors. These are computed for a preselected number of neighborhoods and subsequently interpolated over the entire image. Malandain et al. use an approach in which histograms in consecutive slices are matched using low order polynomials [54], which requires an iterative optimization step. They comment on the fact that a standard

histogram specification approach was inadequate for their data set (brain images). In this paper, we propose a modification to this method. Results will show that the method we have developed is less complex than some of the techniques proposed in the literature, and is fast, non-iterative, parameter free, and robust for the mouse brain histological images we have dealt with in this study.

Results will also show that although individual 3D histological volumes can be reconstructed, they suffer from undesirable defects caused during the slicing process which are difficult to correct. We propose a solution to this problem, which relies on the creation of a virtual 3D histological volume obtained with several 3D real histological volumes through non-rigid registration. The results we have obtained show that the virtual volume possesses clearer internal structures than any of the individual experimentally measured volumes, with fewer defects and superior spatial resolution.

Finally, we use the created histological volumes to validate atlas-based segmentation results we have obtained. In this study, we use MR atlases to segment brain structures. We then use our histological atlases to verify the accuracy of our segmentation results on structures that are difficult to visualize in the MR images.

The remainder of this chapter is organized as follows. First, the method to acquire the histological and MR images is described. We then describe the method used to create the individual 3D histological volumes and register those to their corresponding MR volume. In particular, our new intensity normalization scheme is discussed. Next, the method used to create our virtual histological volume is introduced and we show that the obtained volume is superior to any of the individual volumes used to construct it. Finally, we report our findings on our atlas-based segmentation validation study.

2. Methods

2.1 Image acquisition

The MR image acquisition protocol we have used is as follows. Four male C57/BL mouse (22 g) were fed a standard diet in a controlled environment with a 12/12 h light/dark cycle. Just prior to imaging, anesthesia was induced *via* a 5%/95% isofluorane/oxygen mixture and maintained *via* a 2%/98% isofluorane/oxygen mixture. The temperature of the animal was maintained at 37^{o} C *via* a flow of warm air through the magnet bore. The respiratory rate was monitored throughout the experiments and remained between 35 and 45 breaths per minute for all animals. The mice were imaged in a Varian 7.0 T scanner equipped with a 38 mm quadrature birdcage coil. Two data sets were acquired for each mouse. 200 μm × 200 μm × 500 μm images were acquired for 30 contiguous (i.e., no gap) slices with a standard spin echo sequence with TR = 2000 ms, TE = 35 ms, NEX = 8, and a 128^2 matrix acquired over a 25.6 mm^2 field of view. All procedures adhered to our institution's Animal Care and Use Committee's guidelines.

The method used to create the histological images is detailed elsewhere [55]. Here, we only provide a brief summary of the technique. Generating these images involves five main steps. First, the brains are dehydrated in ethanol; second, the dehydrated brains are then embedded in 12% celloidin; third, the brains are removed from the embedding mold and mounted on embedding blocks; fourth, after being immersed for 24 hours in 80% ethanol, the blocks are cut coronally on a sliding microtome at 30 μm; fifth, sections are stained with cresyl violet and are mounted on

slides. This procedure leads to about eight slides per mouse brain, with each slide holding approximately 40 contiguous cross-sections.

To create the histological images, which can be processed, we scanned these glass slides using a HP ScanJet 5470c scanner with a resolution of 2400 × 2400 dpi and a color depth of 24 bits. This resulted in 800 × 800 pixels images with a pixel resolution of 10 μm × 10 μm. Fig. 2 shows one of the glass slides with one high resolution histological image.

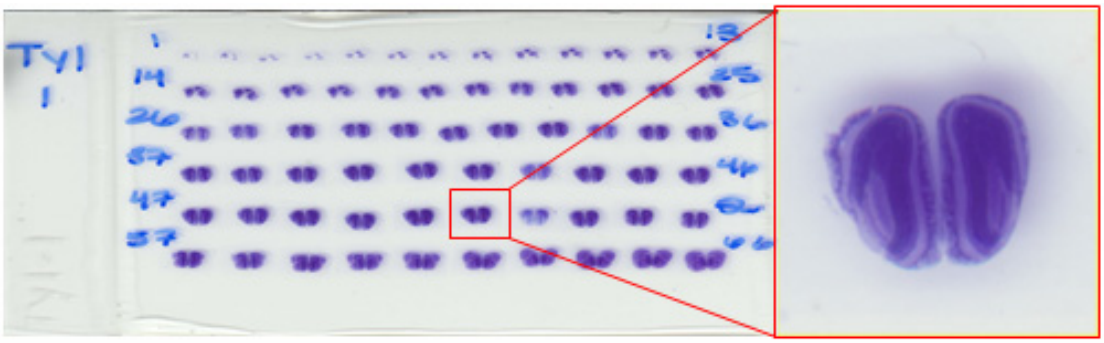

Fig. 2: An example of a histological glass slide.

2.2 3D Histological volume reconstruction

To reconstruct the 3D volume from the histological cross-sections, four steps are applied to the digitized images: image segmentation, center alignment, rigid body alignment, and color normalization. The following sections explain those steps in detail.

Image segmentation

The first step in the process is to extract sub-images, which contain a single cross section from the digitized slides. The connected components on the slides are detected and labeled first, with one individual component containing a single cross-section. Next, sub-images are extracted and ordered, using their position on the slide. Finally, the brain

is extracted from each of the sub-images. To achieve this, we have used a level-set method with a dynamic speed function that we have proposed for the segmentations of images with weak edges [56]. Initial contours are placed outside the brain area and evolve toward the brain edges. The left panel of Fig. 3 illustrates a typical histological image with the initial contours (the blue circles). The middle panel shows the mask extracted with our segmentation algorithm. The right panel shows the brain extracted from the image.

Fig. 3: A histological image with the initial contours (left), the mask extracted with the level-set method (middle), and the extracted image (right).

Center alignment

In this step, the segmented histological slices are registered to each other sequentially, starting from the first image to the last one, by realigning the center of the slices. This step generates a coarse result and provides a good initialization for the next step. The left panel of Fig. 4 shows the result after this step.

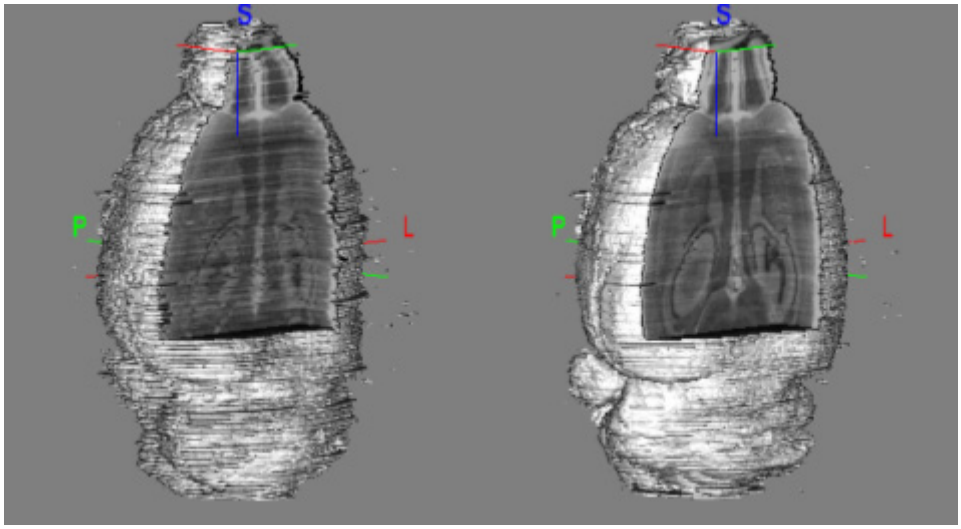

Fig. 4: The reconstructed histological volume before registration (left) and after rigid body registration (right).

Rigid body alignment

Next, the slices are registered rigidly using a Mutual Information-based algorithm. A rigid body transformation only includes three parameters: one rotation angle ***R*** and a translation vector $\boldsymbol{t} = [t_x, t_y]$. The algorithm calculates the optimal parameters ***R*** and ***t*** through maximizing the Normalized Mutual Information (NMI) using Powell's algorithm [57]:

$$F_{\text{cost}} = -\frac{H(A)+H(B')}{H(A,B')}, \tag{1}$$

where ***A*** and ***B'*** are the target image and the transformed image, respectively, and $H(\cdot)$ is the Shannon entropy of the image, which measures the amount of information in this image *via* Eq. (2),

$$H(I) = -\sum_{i\in A} p_i(i)\log p_i(i), \tag{2}$$

where $p_i(i)$ is the probability of an intensity value i in the image ***A***.

Although most of the slices can be registered successfully using this method, failures happen because the algorithm converges to a local minimum. For our data sets, we have observed a 10% error rate. We have also observed that the most critical parameter in our registration algorithm is the number of bins used to compute the joint histograms from which MI is evaluated. Based on this observation, we have developed an algorithm that modifies the number of bins if it is determined that the registration is stuck in a local minimum. Whether or not this happens is determined from the value of the MI between slices. Based on successful registrations, we have determined a normal range for the MI between two histological slices. We have then fixed a minimum MI value that needs to be attained for a registration to be successful. If the registration algorithm terminates and returns a final MI value that does not reach this threshold, the registration is automatically repeated with histograms computed with 8, 16, 32, 64, and 128 bins. The registration that leads to the largest MI value is then selected as the correct one. In the current study this approach reduced the error rate to 1.5%. The remaining mis-registered cases were identified visually and realigned manually. The right panel of Fig. 4 shows the reconstructed volume after this step.

Color normalization

As discussed earlier, not only spatial normalization, but also color normalization is necessary to reconstruct the histological volumes. This is so because individual slices can absorb more or less cresyl violet stain during the histological slice preparation. This, in turn, affects the overall intensity of a slice as well as the contrast between structures.

In this work, we use a weighted histogram specification method on each of the R (red), G (green) and B (blue) channels of the histological images. The standard histogram

specification algorithm consists in computing an intensity transformation $\boldsymbol{T}$ that minimizes the difference between the cumulative histogram of a source image to be corrected and a target histogram:

$$T = \arg \min_{T} \left(\left| C\left(T\left(I_s\right)\right) - C\left(I_t\right) \right| \right), \tag{3}$$

where $\boldsymbol{C}$ is the cumulative histogram function, and $\boldsymbol{I_s}$ and $\boldsymbol{I_t}$ are the reference and target images, respectively.

But, a global optimal intensity histogram (the target histogram) is difficult to find. This is so because different structures are visible in different slices. These slices thus have different intensity distributions and one single target histogram is insufficient to capture the characteristics of all the slices. One solution is to choose a number of target slices spread over the volume and to normalize the intensities block by block. As will be seen, this leads to results that are satisfactory locally but it also produces banding artifacts (i.e., variation in image appearance from one block to the other). Here we propose a method that solves this problem. We start by selecting a number of target slices across the volume. Typically, we choose one target slice every 30 slices (this number was chosen experimentally for our data set) and we normalize slices between these target slices using the intensity histograms of both target slices as follows. Let $\boldsymbol{S_t}$ be the target slice. For every slice $S_i \in \left\{S_t, S_{t+1}\right\}$, we compute the intensity transformations between S_i and S_t, and between S_i and S_{t+1}:

$$T_1 = \arg \min_{T} \left(\left| C\left(T\left(S_i\right)\right) - C\left(S_t\right) \right| \right)$$

$$T_2 = \arg \min_{T} \left(\left| C\left(T\left(S_i\right)\right) - C\left(S_{t+1}\right) \right| \right). \tag{4}$$

The final transformation $\boldsymbol{T}$ for S_i is then computed as:

$$T = \omega_1 T_1 + \omega_2 T_2 \tag{5}$$

where $\omega_1 = \frac{D(S_i, S_{t+1})}{v}$, and $\omega_2 = \frac{D(S_i, S_t)}{v}$, with $\boldsymbol{D}$ the distance between the current slice and one target slice, and v is the distance between two adjacent target slices, which is selected as 30. This technique is simple, non-iterative, fully automatic, and we found it to be robust.

Fig. 5 illustrates results obtained with the various intensity normalization schemes we have discussed. Panel (a) shows the stacked slices prior to segmentation and registration in the horizontal orientation. Hence, every column in this panel represents one coronal histological slice. Panel (b) shows the histological volume after registration but before intensity normalization. Panel (c) shows the intensity normalization results obtained when only one reference histogram is used. Here, the middle slice has been selected as target and all the other intensity values have been normalized sequentially moving to the left and to the right of the central slice. Clearly, this leads to suboptimal contrast for some of the slices (see for example the reduction in contrast in the cerebellum's region). Panel (d) shows the results when several target histograms are selected and the images normalized block by block. This leads to good results within a block but also to noticeable differences across blocks. Panel (e) shows results obtained with our method. These results show that we have been able to remove intensity and contrast differences between nearby slices while preserving good contrast across the entire volume. To show the robustness of our approach, Fig. 6 illustrates the four

histological volumes we have used in this study before (left column) and after (right column) color normalization with our algorithm.

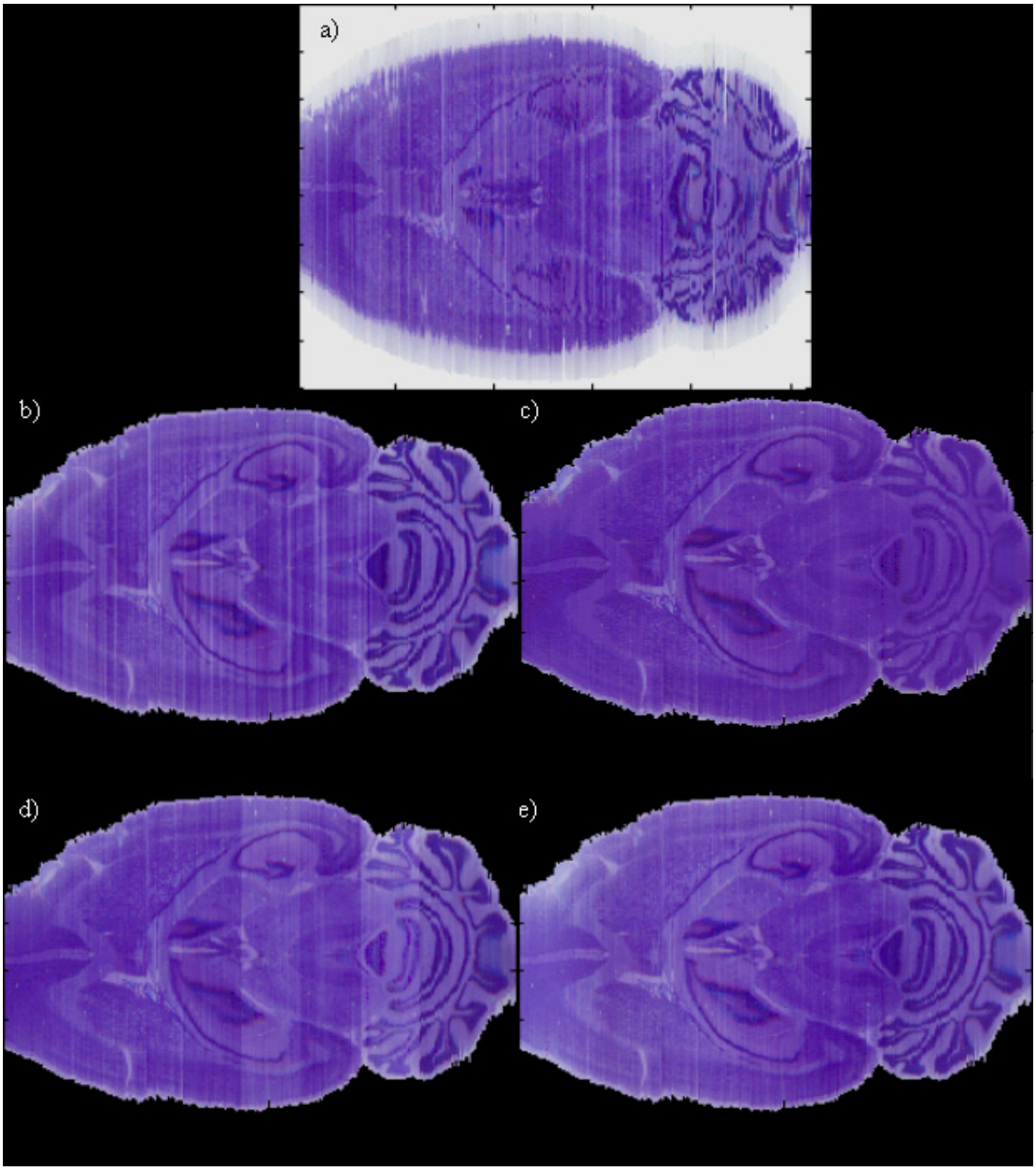

Fig. 5: One slice in the 3D reconstructed histological volume a) after stacking the original histological images, b) after segmentation and registration, c) after color normalization using one single target histogram for the whole volume, d) one target histogram per interval, and e) the method we propose.

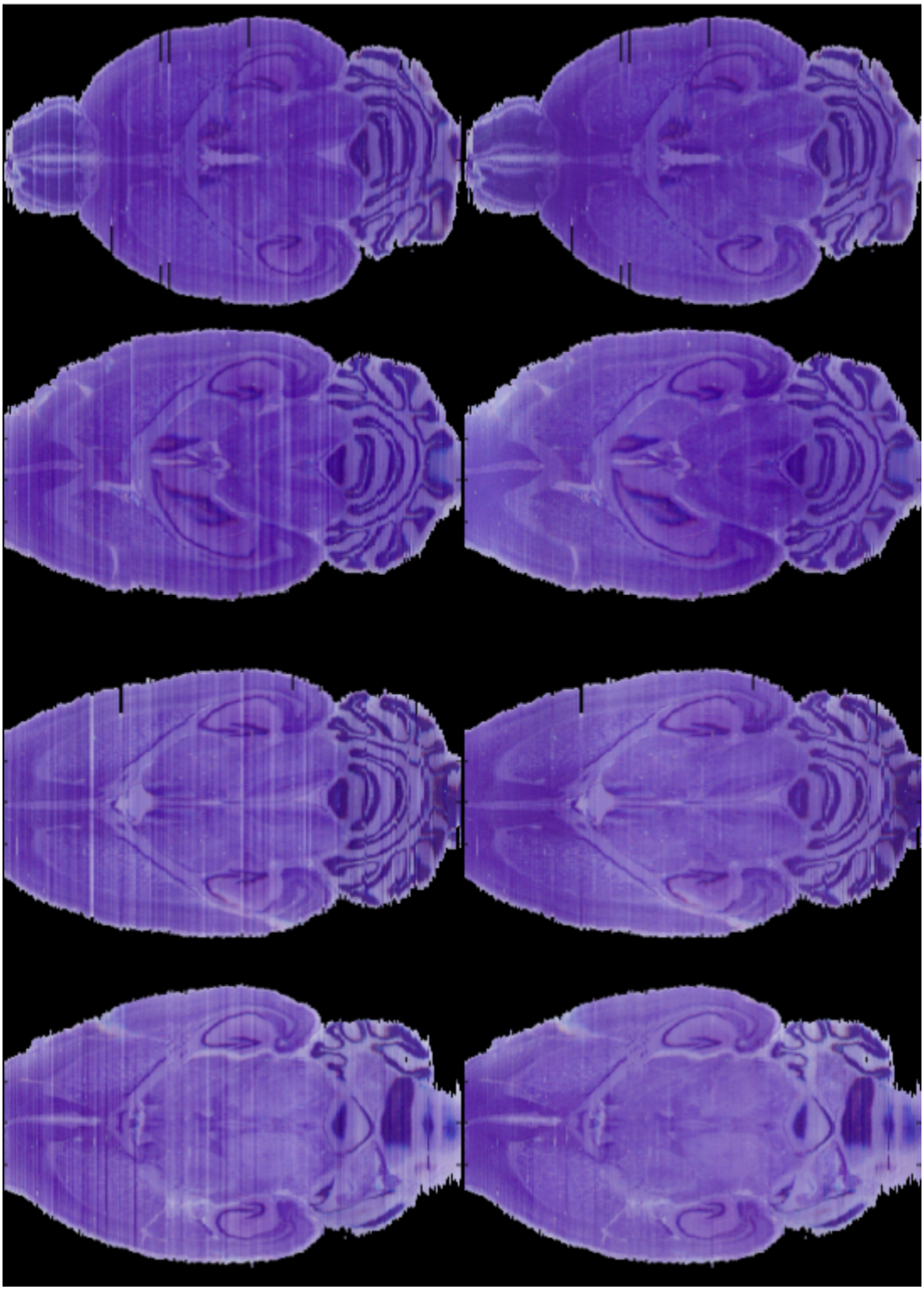

Fig. 6: Four reconstructed histological volumes before (left column) and after (right column) color normalization.

Theoretically, the continuous or discrete transformation of histogram specification is single-valued and monotonic in an interval. However, in practice, after the discrete transformation, the transformed intensities in one image need to be quantized into integers in the range of [0, 255] to generate a new image. It will result that multiple intensities in the source image are mapped into a single intensity in the target image. Moreover, when we calculate the mutual information between two images, usually the number of bins is selected as 32 or 64. It may happen that histogram specification changes the probability of intensities in each bin. Consequently, the mutual information between these two images will be changed indirectly. We investigated whether or not this procedure can influence the mutual information based rigid body registration algorithm. Hence, color normalization was applied to images before and after the step of rigid body alignment, respectively. The results we obtained show that normalizing the images prior to registration did not change the number of times the registration algorithm converged to local minima. This also indicates that MI is largely immune to intensity differences between the slices.

2.3 Registration of histological volumes to their corresponding MR volume

The next step in the process involves registering histological volumes to their corresponding MR volumes. First, brains are extracted from the MR images using the same level-set algorithm we have used to separate background and brain regions in the histological images. Next, the two brain volumes are registered. This requires several steps because of the difficulty mentioned in the Introduction section. Namely, when we reconstruct the histological volumes, we stack images consecutively, while maximizing

the MI between these slices. This leads to histological volumes (the middle panel of Fig. 7) whose overall shape does not match exactly the shape of the MR volume (the left panel of Fig. 7). To address this issue, we first register the MR volume to its histological volume using a rigid body registration technique. When this is done, we translate each slice in the histological image such that its center of mass coincides with the center of mass of the corresponding MR slice. This is similar to what has been done by Yushkevich et al. [61] and Malandain et al. [54]. We note that these authors added one component to insure a smooth transition between successive transformations. They also used transformations with more degrees of freedom. We did not find this necessary with our data set. This is probably due to the fact that we are dealing with mouse MR images that have a much lower spatial resolution than the monkey and human brain MR images they are using in their studies. The result of this operation is shown on the right panel of Fig. 7. Finally, when the individual slices have been registered to the MR volumes, the new histological volume is registered in 3D to the MR volumes using a non-rigid registration algorithm [59], which is described in Section 2.4.

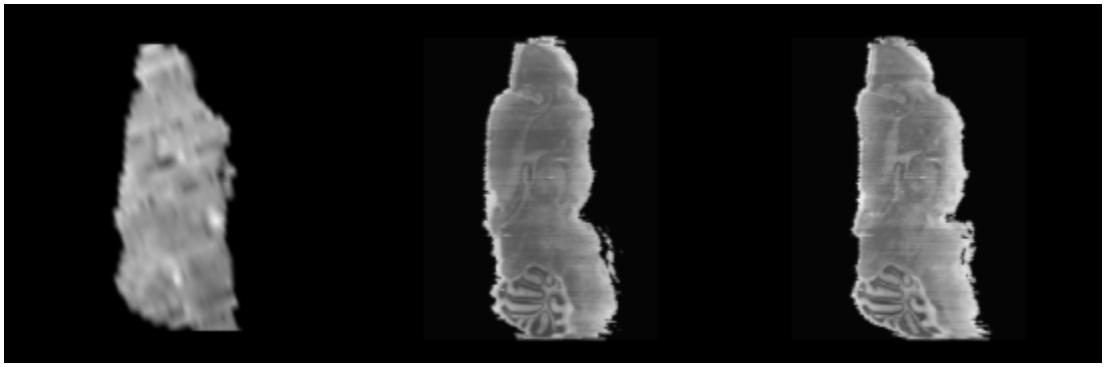

Fig. 7: One sagital slice in one MR volume (left), histological volume after rigid body registration (middle), and histological volume after rigid body registration and realignment of each slice to the corresponding one in the MR volume (right).

Unfortunately, the individual histological volumes we obtain with the aforementioned techniques suffer from a series of defects such as tearing or missing segments. One approach is to try to develop more sophisticated reconstruction techniques that can deal with these issues but these are challenging problems. Automatic, robust, and practical solutions will thus be difficult to develop. A practical alternative is to try to combine several individual volumes and generate one synthetic volume that suffers from fewer defects, which is the approach we have investigated.

2.4 Creation of the average histological volume

The method we have used is a technique that has been proposed for the creation of population averages [58]. In this context, one computes one image volume (e.g., a human brain volume), which is representative of a population as a whole. These averages can then be used to compare populations. Even though our immediate objective is not to compare populations, averaging image volumes can help alleviate defects in individual histological volumes, as these defects are random and occur at different locations in each volume.

The averaging method we have used is illustrated in Fig. 8. First, one histological volume is selected as a reference (the work presented in [58] shows the selection of the reference does not affect the average result) and all the other volumes are registered to this reference image, using a non-rigid registration algorithm. Two deformations fields, which are inverses of each other, are produced by the registration algorithm. The first, which we call the forward field, permits the registration of a volume to the reference volume. The second, which we call the reverse field, permits the registration of the

reference volume to one of the other volumes. Once the deformation fields have been computed, an intensity average is computed. This is done by applying the forward fields to each of the volumes and averaging the resulting volumes. Next, an average shape volume is computed. This is done by first averaging the reverse deformation field. The average reverse deformation field is then applied to the intensity average to produce a new reference. Note that this new reference volume is a "virtual volume"; i.e., it is different from all the original histological volumes. All the volumes are again registered to this new reference volume and the process is repeated until convergence. The experiments we conducted show that after 3 or 4 iterations, both the intensity and the deformation field of the average model remain constant, and the process converges.

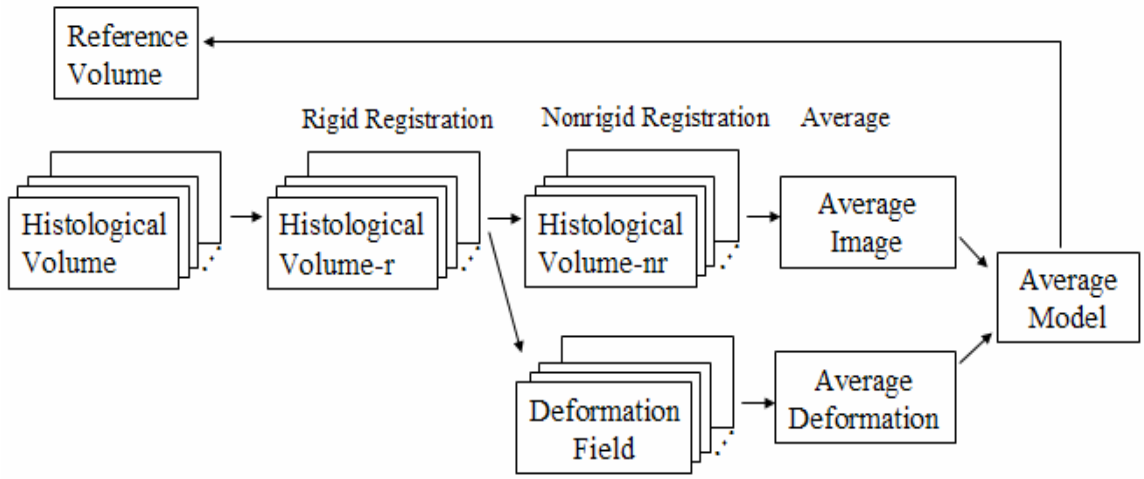

Fig. 8: Flow chart of the algorithm used to generate the average volume.

As is the case for inter-slice intensity normalization, we use a histogram specification method to normalize intensities across volumes. Here, a single target histogram is computed from the target volume; the intensities in the other reconstructed volumes are normalized to match the target one.

The algorithm we have used to compute the non-rigid registration is an MI-based algorithm we have proposed, which we call ABA for adaptive bases algorithm [59]. This algorithm models the deformation field that registers the two images as a linear combination of radial basis functions (RBFs) with finite support:

$$\mathbf{v}(\mathbf{x}) = \sum_{i=1}^{N} \mathbf{c}_i \Phi(\mathbf{x} - \mathbf{x}_i) \tag{6}$$

where x is a coordinate vector in $\Re^d$, with d being the dimensionality of the images. Φ is one of Wu's compactly supported positive radial basis functions:

$$\Phi(\mathbf{x}) = \phi\left(\frac{\|\mathbf{x}\|_2}{s}\right) \tag{7}$$

with

$$\phi(r) = (1-r)_+^4 \left(3r^3 + 12r^2 + 16r + 4\right) \tag{8}$$

where $(1-r)_+ = \max(1-r, 0)$. s is the support size of the basis function, and $\|\bullet\|_2$ is the Euclidean norm. The $\mathbf{c}_i$'s are the coefficients of these basis functions. The coefficients of the basis functions are computed through maximizing the Normalized Mutual Information.

The algorithm is applied using multiscale and multi resolution approach. The resolution is related to the spatial resolution of the images. The scale is related to the region of support and the number of basis functions. Typically, the algorithm is started on a low-resolution image with few basis functions with large support. The image resolution is then increased and the support of the basis function decreased. Following this approach, the transformations become more and more local as the algorithm progresses. The

algorithm progresses until the highest image resolution and highest scale are reached. Hence, the final deformation field is computed as:

$$\mathbf{v}(\mathbf{x}) = \mathbf{v}_1(\mathbf{x}) + \cdots + \mathbf{v}_M(\mathbf{x}) \tag{9}$$

with M the total number of levels.

With this algorithm, it is possible to spatially adapt the stiffness characteristics of the transformation. In previous work [60], we have shown this to be of value for registering brain volumes with large space-occupying lesions or with extremely large ventricles. We found it to be useful for this application as well. Looking at Fig. 9, one observes that the images are made of two distinct regions. The first one is the cerebellum in which layers of white and gray matter are clearly visible; these create distinct features that can guide a non-rigid, intensity-based, registration algorithm. The second region encompasses the rest of the brain. In this region, contrast is weaker and internal structures and substructures do not show clearly defined edges. It is well known that intensity-based algorithms as the one we use need to be regularized more over uniform regions than they need to be on regions with a lot of edge information. In our algorithm, regional stiffness properties can be defined using what we call a stiffness map (i.e., a file that has the same dimensions as the images and that specifies stiffness values at every pixel). In this study, we have used a simple binary map. Stiffness is smaller over the cerebellum region than it is over the rest of the brain region. In other words, the deformation field is regularized more over regions in which edge information is not very reliable (the brain) and less over regions in which edge information is more reliable (the cerebellum).

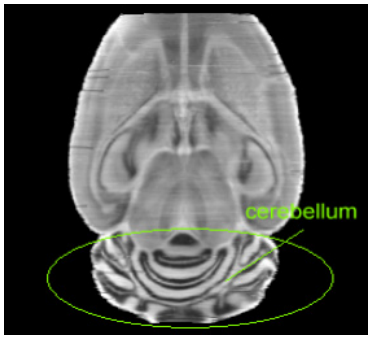

Fig. 9: One slice in a histological volume showing the cerebellum.

The effect of using two stiffness values is shown in Fig. 10. The left panel in this figure shows one slice in the reference volume. To create the middle panel, another volume was first registered to the reference volume using one single stiffness value, which produces good results over the brain region. The reference volume and the registered volume were then averaged. The middle panel shows one slice in this average volume. The right panel shows the same but when two stiffness values are used (the transformation is more elastic over the region of cerebellum). This figure shows that the average volume is aligned more accurately over the region of cerebellum when two stiffness values are used, thus suggesting a better registration.

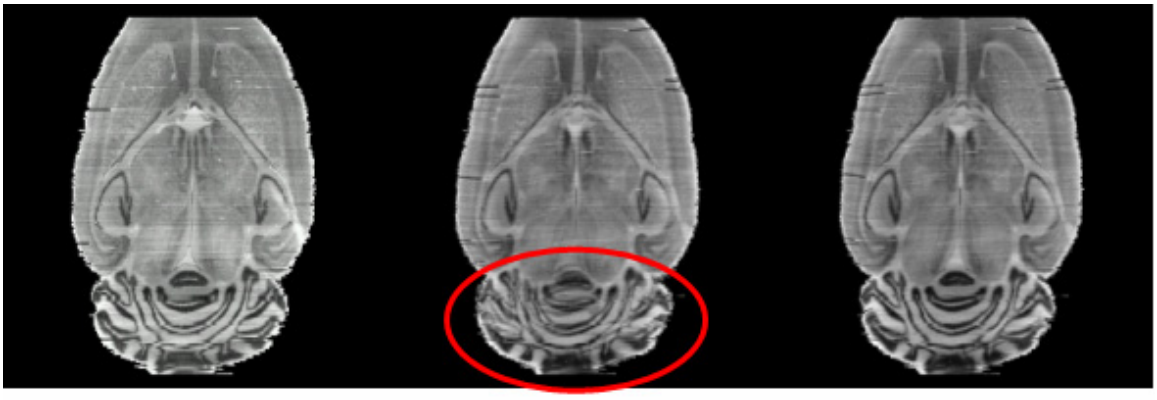

Fig. 10: One slice in the reference volume (left), in the average of two volumes registered with one single stiffness value (middle), and in the average of two volumes registered with two stiffness values (right).

2.5 Creation of the average MR volume

A single MR volume can be created from the four MR volumes acquired in this study in two ways. The first one involves repeating the procedure described above for the creation of the average histological volume. The second one involves creating this average indirectly, through the histological average. In this approach, the transformation that register the MR volume to its histological volume and the transformation that registers the histological volume to the average are combined. The two methods will be compared in the next section.

3. Results

3.1 Results of the averaged volumes

Fig. 11 shows the improvement one can expect when using several histological volumes. The left panel shows an average obtained with two histological volumes, the middle panel is the average obtained with three histological volumes, and the right panel is the average obtained with all four volumes. Green marks show some defects appeared in the first two averages, but disappeared in the third average. The red mark shows one artifact existing in the third average. Although new defects may be brought into the average, clearly, increasing the number of volumes used to compute the average generally reduces the defects visible in the average and increases its overall signal-to-noise ratio (SNR).

Fig. 12 and Fig. 13 illustrate the results we have obtained with our averaging method. In these figures, the top panel shows one slice in the average. The other panels

show the same slice in the four individual volumes used in this study. These figures show two important things. First, defects that are apparent in the individual volumes have virtually disappeared from the average volume. Second, small structures, such as the medial terminal nucleus of the accessory optic tract, the nigrostriatal fibers, or the lateral geniculate body, are clearly visible in the average volume despite being barely visible in the individual image volumes.

Fig. 14 compares average MR volumes obtained with the two approaches described in Section 2.5. The left panel in the image shows one slice in one of the original volumes. The middle panel shows one slice in the average MR volume obtained when the histological images are used and the right panel a slice in the average MR volume obtained when MR images alone are used. The right panel is blurrier than the middle one, suggesting that using the histological image volumes improves the registration process. This finding is not very surprising. Indeed, contrast and visibility of internal brain structures are substantially lower in MR images than they are in the histological images. Accurate inter-subject non-rigid registration is thus more difficult for MR images than it is for histological images. When the histological images are used for atlas creation, the only non-rigid registration applied to the MR images is the last step in the intra-subject MR-histological registration process. Typically, this only requires small displacements that improve the results obtained with the rigid-body step. This is a much simpler non-rigid registration problem than the inter-subject registration step required to register MR volumes to each other directly.

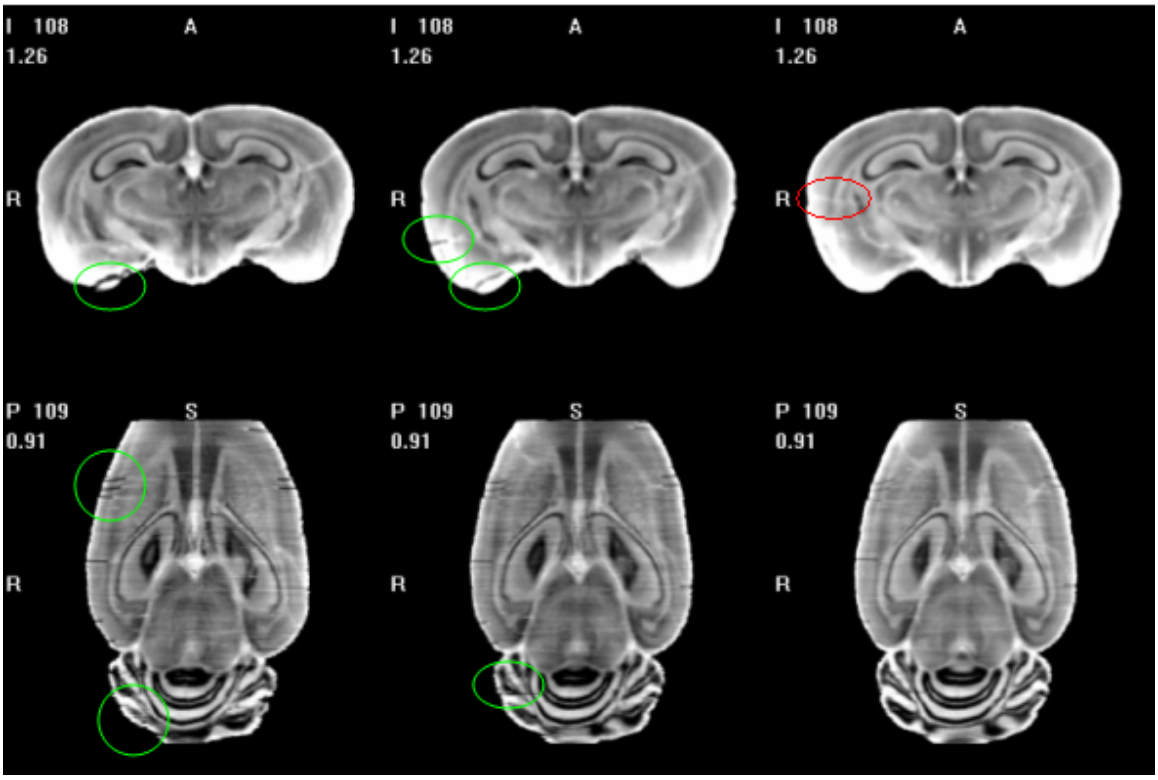

Fig. 11: Slices in the average volumes generated using two (left), three (middle) and four (right) individual volumes.

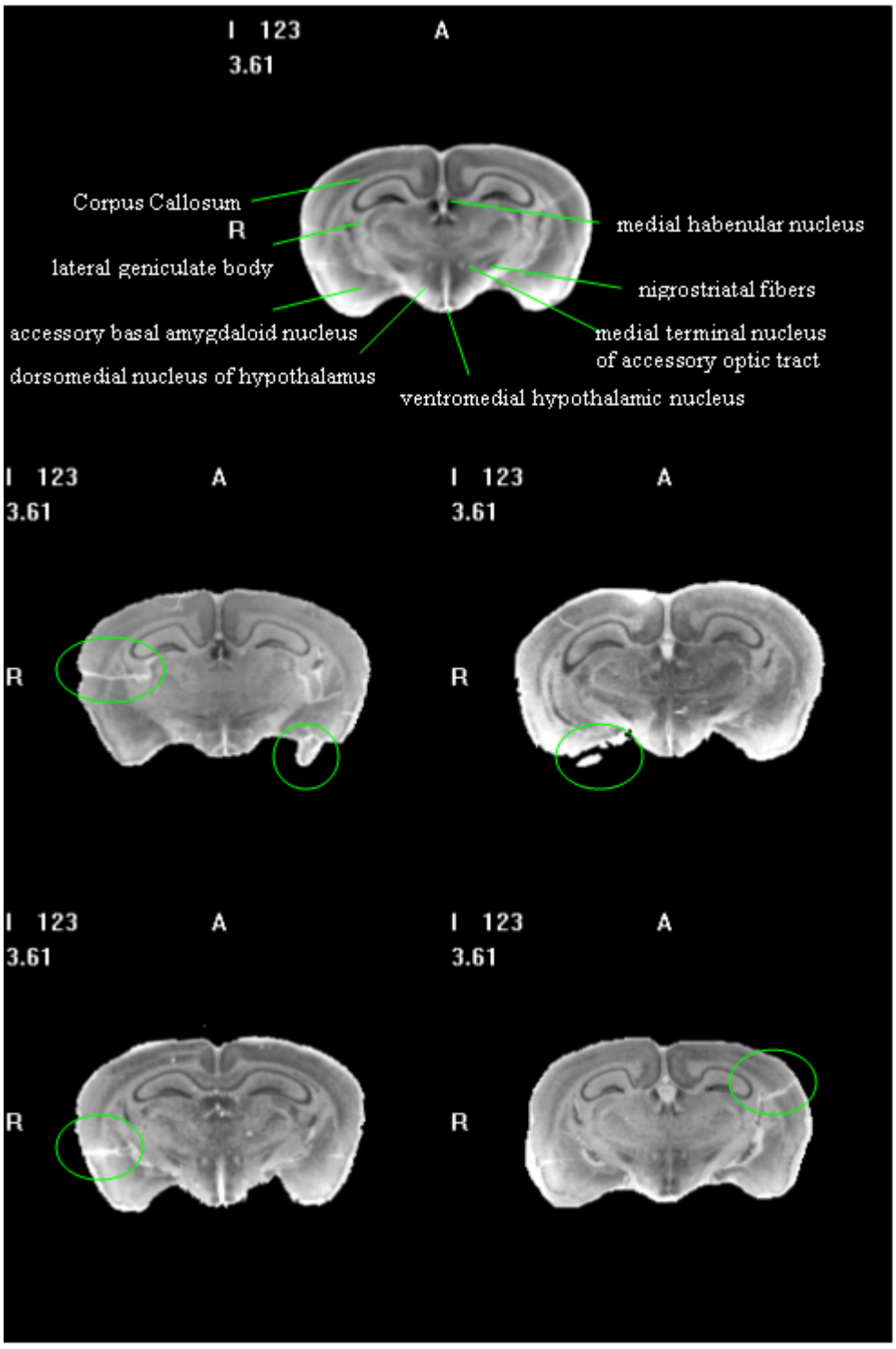

Fig. 12: One axial slice from the averaged histological volume (1st row) with labeled structures, and individual volumes (2nd – 3rd rows). Green circles mark some defects in the individual volumes.

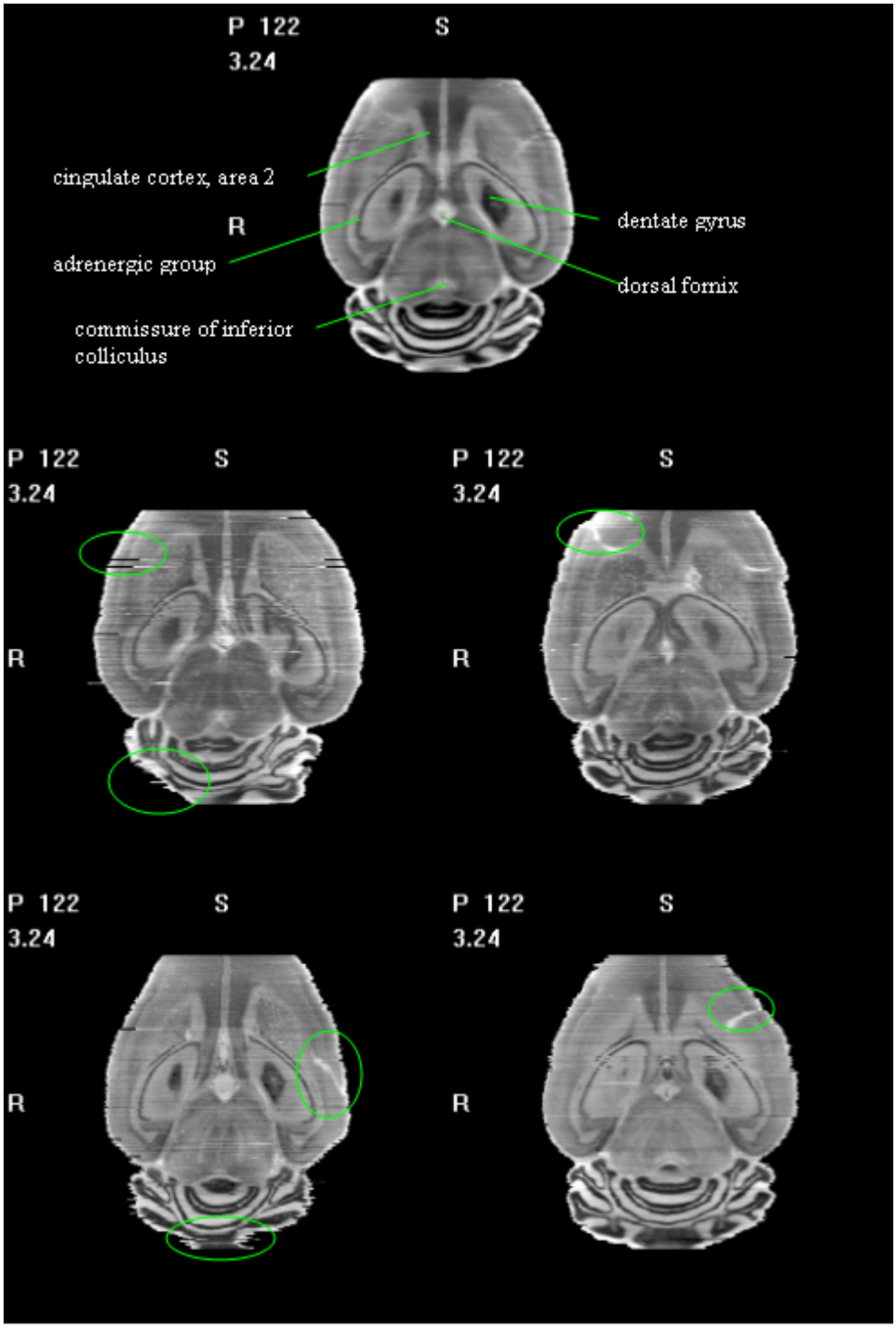

Fig. 13: One coronal slice in the averaged histological volume (1st row) with labeled structures, and individual volumes (2nd – 3rd rows). Green circles mark some defects in the individual volumes.

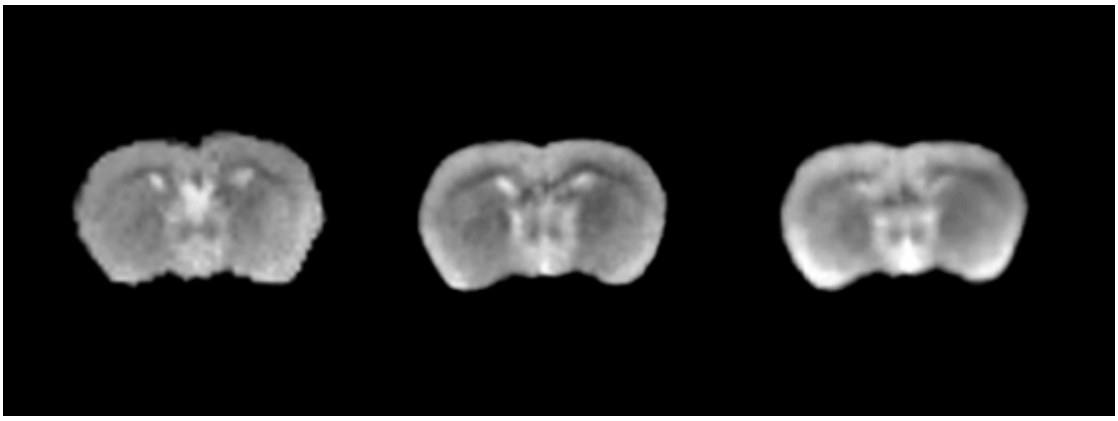

Fig. 14: One slice in the original MR volume (left), in the average MR volume obtained using the histological volumes (middle), and the average MR volume obtained by registering MR volumes directly (right).

3.2 Validation of atlas-based segmentation

Atlas-based segmentation refers to a segmentation method in which structures of interest are segmented through registration. The structures are first delineated in one image volume, usually referred to as the atlas. The atlas is then registered to the volume to segment, and labels assigned to voxels in the atlas are projected from the atlas to the other volume with the deformation field. As is the case with any segmentation algorithm, validation of the results is difficult. It is even more so with mice MR images in which structures and substructures are difficult to visualize. Here we have taken advantage of our histological volumes to validate segmentation results on structures that are not very well resolved in MR images. We have complemented this study with another one in which we have validated the segmentation results on structures visible in the MR images. Results obtained with both these studies are presented in the next subsections.

Validation using the existing histological volumes

To evaluate our segmentation approach, we have used a "leave-one-out" method. We have created four MR atlases as described in section 2.5. Each of these atlases was created using only three of the four MR-histological volume pairs and tested on the fourth one as follows. First, the hippocampus was delineated manually in each of the histological atlases. Next, the MR atlases (created with three volumes) were registered to the fourth MR volume, which is registered to its own histological volume. The deformation field computed using this method was then used to project the hippocampus contours from the histological atlas onto the fourth histological volume. This approach permits evaluating the accuracy of our atlas-based segmentation method in four volumes. Fig. 15 shows hippocampus contours we have obtained automatically and manually superimposed on the MR volume not used to create the atlas (left column) and on the corresponding histological volume (right column). The histological images including abundant anatomical details make it straightforward to judge the segmentation results and this figure demonstrates visually that our atlas-based segmentation approach is accurate. To validate the results quantitatively, manual and automatic contours were compared using the Dice similarity index [62] defined as follows:

$$\text{Dice Similarity} = 2 \times \frac{n\{A \cap M\}}{n\{A\} + n\{M\}} \tag{10}$$

where $n\{.\}$ indicates the number of voxels within a region and A and M are the automatic and manual contours. Fig. 16 shows this Dice similarity result. Dice values above 0.7 are customarily considered indicative of a good agreement between contours [80]. Hence, Fig. 16 demonstrates an excellent atlas-based segmentation result.

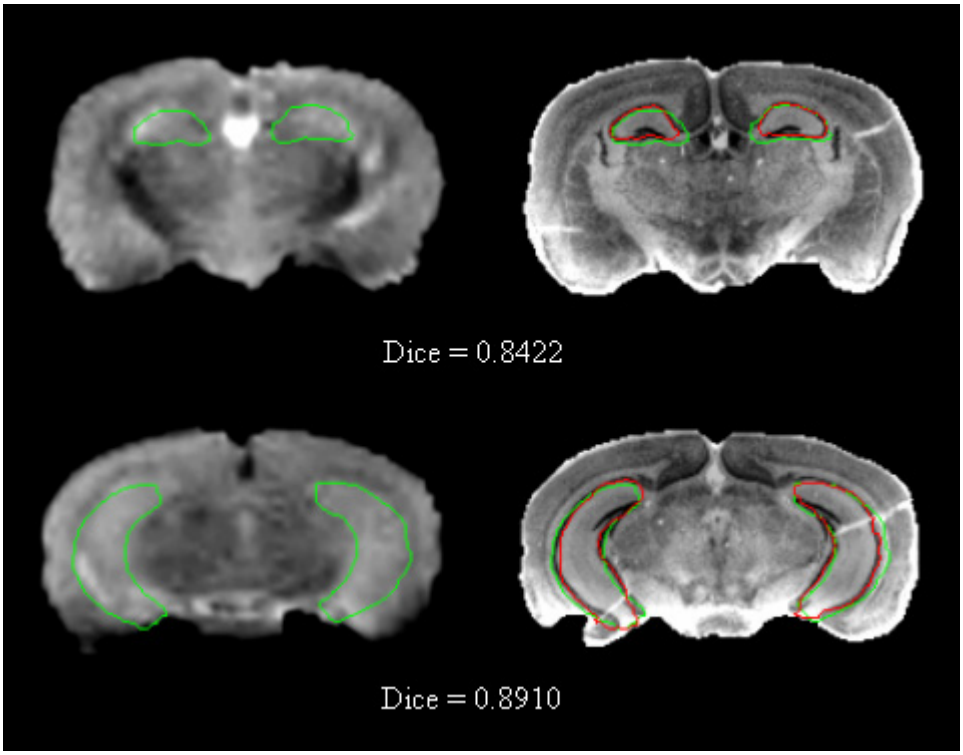

Fig. 15: Hippocampus contours superimposed on the MR volume (left column) and on the corresponding histological volume (right column).

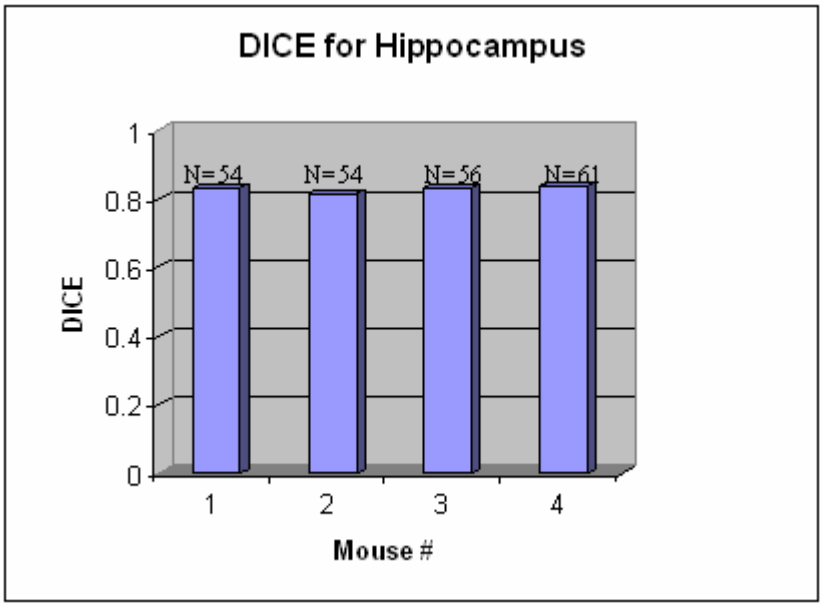

Fig. 16: The Dice similarity index for hippocampus structures (N: the number of slices).

Validation using new mouse brains

To evaluate further the potential of atlas-based techniques for the analysis of mice brain images, we have acquired another ten image volumes (i.e., these volumes were not used to create our average). The same protocol used to acquire the atlas images has been followed to acquire these images (a standard spin echo sequence with TR = 2000 ms, TE = 35 ms, NEX = 8), with voxels dimension of 200 μm × 200 μm × 500 μm. Three structures were segmented manually in the atlas created with the method described in section 2.5: the left lobe, the right lobe, and the cerebellum. These three structures were also segmented manually in the 10 new volumes. We limited our study to these structures because these could be easily visualized in the MR volumes. The atlas was registered to all the other volumes and 3D structures delineated in the atlas were deformed with the computed deformation field. Contours obtained automatically were compared to the manual contours using the Dice similarity. Table I shows the Dice values for all ten mice. The mean values for all three structures are above 0.9, which indicates an excellent agreement between the automatic contours and the manually segmented contours. Those mean values are larger than the Dice values of hippocampus contours in the previous validation experiment. The reason is that, compared with the regions of hippocampus, these three structures have clear edges in the MR images, which leads to the more accurate registration results.

Table I: Dice coefficients of three structures of mouse brains.

	Left lobe	Right lobe	Cerebellum	# of slices (left/right)	# of slices (cerebellum)
# 01	0.9589	0.9578	0.9377	15	3
# 02	0.9695	0.9643	0.9351	16	3
# 03	0.9729	0.9707	0.9310	17	3
# 04	0.9687	0.9621	0.9135	16	3
# 05	0.9600	0.9587	0.9004	15	3
# 06	0.9653	0.9560	0.9144	14	3
# 07	0.9603	0.9597	0.9291	16	3
# 08	0.9705	0.9663	0.9192	14	3
# 09	0.9724	0.9658	0.9109	15	4
# 10	0.9722	0.9700	0.8750	16	3
Mean	**0.9671**	**0.9632**	**0.9166**	**15.4**	**3.1**

4. Conclusion

Defects in individual histological slices are unavoidable and difficult to correct because they involve tearing, missing parts, or folding. The study we have conducted has shown that a very practical solution to reconstruct 3D histological volumes of high quality is to use more than one reconstructed histological volume and to create one single volume from these through non-rigid registration. The accuracy of our non-rigid registration is such that the average it produces has a higher signal-to-noise ratio than any of the individual volumes used for its creation. This permits the clear visualization of structures that are not easily discernable in the individual volumes. Also, defects in individual volumes become less apparent in the average one because of the intensity averaging we perform. Although one could expect even better results with more than four volumes, our study has shown that four is sufficient to produce visually satisfying results. As noted in the introduction, intensity normalization is an important component for the reconstruction of histological volumes. Others have proposed methods that are somewhat

complex, often requiring iterative optimization steps and parameter adjustments. The new method we propose is based on a standard histogram specification technique. With the modification we have developed it leads to satisfactory results while being simple, fast, and parameter free (except for the selection of the number of target histograms, which is not critical). Using our histological atlases, we have shown that atlas-based segmentation methods lead to accurate results for mice MR images both on structures that are visible in these images and on structures that are difficult to discern. This suggests the use of these methods for the automatic analysis of small animal images. An immediate and promising application of this technique involves the segmentation of brain structures in mouse populations that have been, for example, genetically manipulated—an area of active investigation to understand the adult and developing mammalian central nervous system (see for instance [64][65][66]). Others have developed digital MR atlases (for instance [67][68][69]). These are built directly from 3D tomographic volumes that are acquired with very long acquisition sequences. While results obtained with these approaches are excellent, there remains a place for histological atlases. Indeed, histology can still provide a spatial resolution that is far superior to what is achievable with MR and numerous histology strains can be used to visualize nuclei or cell surface receptors that can not be seen in MR images. It is thus likely that histology will remain the standard for many years to come. But, the creation of good quality histological cross-sections is a difficult task that requires experience and skills. The method proposed herein permits the reconstruction of high quality volumes even if the raw data is less than perfect.

CHAPTER III

FULLY AUTOMATIC INTRA- AND INTER-SUBJECT REGISTRATION OF WHOLE BODY CT IMAGES

1. Introduction

Image registration is essential to quantitatively follow disease progression, to assess response to therapy, to compare populations, or to develop atlas-based segmentation methods. The first two applications typically involve several image volumes acquired serially from the same subject and require intra-subject registration methods. The last two, which involve images acquired from different subjects, require inter-subject registration techniques. In both cases, non-rigid registration methods are required as soon as the structures of interest are more complex than a single rigid body object. A number of methods and techniques have been developed to achieve this; chief among them are intensity-based techniques and, in particular, methods that rely on Mutual Information (MI) [22][12]. However, most automatic methods that have been proposed have been applied to head images only. This is no doubt due to the fact that whole body image data sets present a set of difficulties not found in head data sets. Head images contain one single major identifiable structure (the brain) as opposed to whole body images that contain many articulated structures (the skeleton and organs). Despite the fact that a number of methods have been proposed for extra-cranial applications such as breast, lung, or prostate images [47][48][70], very few have been proposed to attack issues associated with images that contain many articulated structures, the relative position of which changes between acquisitions.

This type of image remains challenging because, in practice, non-rigid registration algorithms need to be initialized with a rigid or affine transformation. If the image volumes do not contain articulated structures, as is the case, for example, for head images, one global rigid or affine transformation is sufficient to initialize the non-rigid registration algorithms. If, on the other hand, these image volumes contain a number of skeletal structures, which are rigid but whose relative position changes from acquisition to acquisition, one global rigid or affine transformation is insufficient and more local approaches have to be used. We now briefly review the methods designed to address this problem.

A typical approach that is used is to rely on a number of local transformations, each one computed for one element in the articulated structure. These transformations are then combined. This is the approach followed by Little et al. [49]. These authors present a technique designed for the intra-subject registration of head and neck images. Vertebrae are registered to each other using rigid body transformations (one for each pair of vertebrae). Transformations obtained for the vertebrae are then interpolated to produce a transformation for the entire volume. One limitation of this approach is that it requires segmenting and identifying corresponding vertebrae in the image volumes. Because corresponding vertebrae are registered with rigid-body transformations, the approach is also applicable only to intra-subject registration problems.

Martin-Fernandez et al. [50] proposed a method, which they term “articulated registration”. This approach requires the labeling of landmarks to define wire models that represent the bones. A series of affine transformations are computed to register the rods, which are the elements of the wires. The final transformation for any pixel in the image is

obtained as a linear combination of these elementary transformations with a weighting scheme that is inversely proportional to the distance to a specific rod.

Arsigny et al. [51] also present an approach in which local rigid or affine transformations are combined. They note that simple averaging of these transformations leads to lack of invertibility, and they propose a scheme that permits the combination of these local transformations, while producing an overall invertible one. Their method, which is applied to the registration of histological images, has not been tested on whole body images.

Recently, Papademetris et al. [52] put forth an articulated rigid registration method that is applied to the serial registration of lower-limb mouse images. In this approach, each individual joint is labeled and the plane in which the axis of rotation for each joint lies is identified. A transformation that blends piecewise rotations is then computed. Their approach produces a transformation that is continuous at these interfaces but requires manual identification of joint segments. The authors have applied their method to the registration of lower limbs in serial mouse images. The same authors have also presented an integrated intensity and point-feature non-rigid registration method that has been used for the registration of sulcal patterns and for the creation of mice population averages [71]. While similar to our own approach, it has not been used for the registration of skeletons.

A. du Bois d'Aische et al. [72] deal with the articulated rigid body registration problem using a three-step strategy: (1) articulated registration which combines a set of rigid body matrices, (2) mesh generation for the image, and (3) propagating the

displacement to the whole volume. This work has only been applied to intra-subject registration problems.

Johnson et al. [73] presented two algorithms called Consistent Landmark Thin-Plate Spline Registration (CL-TPS) and Consistent Intensity-based Thin-Plate Spline Registration (CI-TPS). Then they extend these to the Consistent Landmark and Intensity Registration Algorithm (CLI-TPS), in order to match both landmarks and the areas away from the landmarks. In this algorithm, the landmarks need to be selected and their correspondences need to be identified manually.

Baiker et al. [78] introduced a hierarchical anatomical model of the mouse skeleton system for the articulated registration of 3D whole body data of mice. But their model does not include the ribs, which we have found important to guarantee the accurate registration of structures such as the heart or the lungs.

In summary, a survey of the literature shows that only a few methods have been proposed to register images including articulated structures. Most approaches compute piecewise rigid or affine transformations and somehow blend and combine these transformations. Unfortunately, these approaches are often not practical because they require identifying various structures in the images such as joints or individual bones and are therefore not automatic. In this paper we propose a fully automatic method that does not require structure labeling. We demonstrate its performance on small animal and human images. The data used in this study is described in Section 2 of this chapter. In the method section, we introduce the whole body image registration method we propose which includes three main steps. The experiments we have performed and results we have obtained are presented in Section 4. Both our algorithm and results are discussed in Section 5.

2. Data

Two types of images have been used in the study presented herein: images acquired from small animals and images acquired from humans. The small animal data sets include CT and MR images while the human data sets only include CT images. MR images have been acquired for the small animals to permit validation of the method we propose, which is primarily designed for CT images, on soft tissue structures. Soft tissue contrast in CT images is poor but the additional MR image volumes we have acquired permits us to indirectly validate our method, as will be described in more detail in the Experiment section.

To permit long MR acquisition times with high signal to noise and without motion artifacts, mice were first sacrificed, and then imaged in a Varian 7.0T MR scanner equipped with a 38mm quadrature birdcage coil. A T_1-weighted spoiled gradient recalled echo sequence with a TR/TE of 20 ms/5ms and a flip angle of 5^o was employed. The acquisition matrix was 500×128×128 over a 90×32×32 field of view yielding a spatial resolution of approximately $0.176\times0.25\times0.25mm^3$. Next the mice were imaged within the same holder using an Imtek MicroCAT II small animal scanner to generate the CT images. CT imaging was at a voltage of 80kvp with an anode current of 500μA. Acquisition parameters of 360 projections in 1^o steps, exposure time 600ms, and acquisition matrix 512×512×512 were employed. Total scan time is just over eight minutes, and images have $0.2\times0.2\times0.2$ mm^3 isotropic voxels. The mice posture was then changed arbitrarily and a second set of MR and CT scans were acquired. This process was repeated in four mice. The CT and corresponding MRI scans for each mouse can

easily be co-registered with a rigid body transformation, because the mouse was in the same holder during CT and MR acquisitions.

Although our main domain of application is small animal images, we have also used human data sets to show the generality of our algorithm. Two pairs of inter-subject human upper torso images were acquired. One pair of images consists in a 512×512×170 and a 512×512×198 CT volumes with a voxel resolution of $0.9375\times0.9375\times3mm^3$. The other pair of images consists in a 512×512×184 and a 512×512×127 CT volumes with a resolution of $0.9375\times0.9375\times3mm^3$ as well.

3. Methods

The methods we propose involve one pre-processing step and three main registration steps (shown in Fig. 17): intensity-based rigid body registration, point-based nonrigid registration, and intensity-based nonrigid registration. The three registration steps are discussed in detail in the following sections.

3.1. Step one: intensity-based rigid body registration

First, a standard Mutual-Information (MI) based rigid body registration algorithm [22] is applied to the source and target CT volumes. A rotation matrix $\boldsymbol{R}$ and a translation vector $\boldsymbol{t}$, which maximize the normalized mutual information [79] (NMI) between the images are computed using Powell's conjugate direction method [57]. The normalized mutual information is defined as:

$$NMI = \frac{H(A)+H(B)}{H(A,B)}, \tag{11}$$

where A and B are two images, and $H(\cdot)$ is the Shannon entropy of the image which measures the amount of information in this image:

$$H(A) = -\sum_{i \in A} p_i(i) \log p_i(i), \tag{12}$$

with $p_i(i)$ is the probability of an intensity value i in the image A.

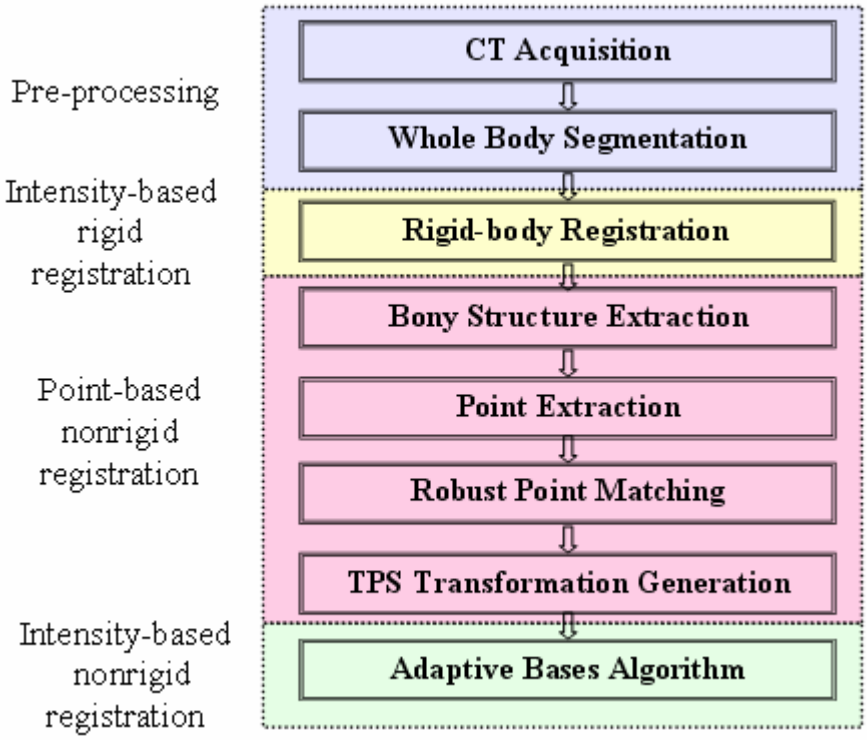

Fig. 17: The flowchart of the algorithm, which includes three main steps: intensity-based rigid body registration, point-based nonrigid registration and intensity-based nonrigid registration.

3.2. Step two: nonrigid point-based registration

Next, a set of points is extracted from the skeletons in the images to be registered. In CT images, the bones have a higher intensity than soft tissues. The bony structures can thus be segmented easily in CT images with one single threshold. Here, a simple manual

method has been used to select this threshold. Iso-intensity surfaces were generated with various thresholds and the intensity value that produced the best surface was chosen. Points are then selected automatically in the thresholded image as follows. For each axial slice in the skeleton volume, the connected areas are detected and the center of each of these areas is located. The set of points used for registration is the set of central points, which approximately corresponds to the centerline of the skeletons.

The sets of points extracted from the source and the target images are then registered using the Robust Point Matching (RPM) algorithm proposed by Chui et al. [74]. This algorithm takes two sets of points as input and iteratively computes a correspondence between these points and the transformation that registers them.

First, a correspondence matrix is calculated. Instead of assigning a binary value for every pair of points, a continuous value in the interval [0, 1] is calculated, according to the softassign algorithm proposed by Gold et al.[75]:

$$m_{ai} = \frac{1}{T}\exp\left(-\frac{(x_i - f(\upsilon_a))^T (x_i - f(\upsilon_a))}{2T}\right), \tag{13}$$

where V: $\{\upsilon_a,\ a = 1, 2, \ldots, K\}$ and X: $\{x_i,\ i = 1, 2, \ldots, N\}$ are two sets of points from the source and target images. f is the transformation or mapping function, which is used to register the images (more details on this mapping function are provided below). T is called the temperature parameter, which is introduced to simulate physical annealing. In the original paper, the suggested initial value for T is 0.5. The annealing schedule for T is $T = T \cdot r$, with r the annealing rate. A recommended value for r is 0.93. In this work, we have used the recommended values for every volume. The fuzzy correspondence matrix is normalized at each iteration, so that the sum of each row and each column is kept as

one. Thus, equation (13) establishes a fuzzy correspondence between points in the set V and points in the set X; the fuzziness of the assignment decreases as the algorithm progresses. Major advantages of this fuzzy assignment are that the cardinality of the sets X and V does not need to be equal and that a virtual correspondence between points in these sets can be established using this fuzzy matrix, as explained next.

At each iteration, after the correspondence is determined, a thin plate spline-based non-rigid transformation f is computed, which solves the following least-squares problem:

$$\min_f E(f) = \min_f \sum_{a=1}^{K} \|y_a - f(\upsilon_a)\|^2 + \lambda T \|Lf\|^2, \tag{14}$$

where $y_a = \sum_{i=1}^{N} m_{ai} x_i$ and y_a can be considered as a virtual correspondence for υ_a. This correspondence is computed by weighting all the points in X. L is an operator which measures the smoothness of the thin plate spline transformation. Here the integral of the mapping function f is used. λ is a regularization parameter that balances the terms. The value of λ also changes from iteration to iteration. Initially a high value is chosen for λ, leading to a smooth transformation. As the algorithm progresses, the correspondence between points becomes crisper and the smoothness constraint is relaxed to increase accuracy. As is the case for the other parameters, the value of λ is modified according to an annealing schedule:

$$\lambda = \lambda^{init} \bullet T, \tag{15}$$

A recommended value for λ^{init} is 1, which has also been used here. The correspondence and transformation steps are computed iteratively using equations (13) and (14), with the temperature T decreasing. Finally, the transformation computed based

on the points is applied to the entire image volume. This deformed volume is then used as the input to the next step.

3.3. Step three: intensity-based nonrigid registration

The last step in our approach relies on an intensity-based registration algorithm we have proposed, which we call ABA for adaptive bases algorithm [59]. This algorithm uses mutual information as the similarity measure and models the deformation field that registers the two images as a linear combination of radial basis functions (RBFs) with finite support:

$$\mathbf{v}(\mathbf{x}) = \sum_{i=1}^{N} \mathbf{c}_i \Phi(\mathbf{x} - \mathbf{x}_i), \tag{16}$$

where $\mathbf{x}$ is a coordinate vector in $\Re^d$, with d being the dimensionality of the images, Φ is one of Wu's compactly supported positive radial basis functions [76], and the $\mathbf{c}_i$'s are the coefficients of these basis functions. The goal is to find the $\mathbf{c}_i$'s that maximize the mutual information between the images. The optimization process for the coefficients includes a steepest gradient descent algorithm combined with a line minimization algorithm. The steepest gradient descent algorithm determines the direction of the optimization. The line minimization calculates the optimal step in this direction.

In our implementation, the algorithm is applied using a multilevel approach. Here, multilevel includes multiscale and multiresolution. The resolution is related to the spatial resolution of the images. The scale is related to the region of support and the number of basis functions. When an image pyramid is created, the images are down-sampled at several resolution levels, and the registration algorithm is applied at each level. The

algorithm is started on a low-resolution image with few basis functions. The basis functions are located regularly on the image and the support of basis functions is kept constant at this level. The regions of mismatch are then identified and the optimization process is performed on those regions independently. This strategy is described in detail later. Typically, as the image resolution increases, the region of support is decreased and the number of basis function is increased. As a consequence, the transformations become more and more local as the algorithm progresses.

In our experiments, all small animal CT images are down-sampled into three resolution levels: 64×64×64, 128×128×128, and 256×256×256 voxels. At the lowest level we use a matrix of 6×6×6 basis functions. At the intermediate level, we use a matrix of 10×10×10 basis functions. At the highest resolution level we start with a matrix of 14×14×14 basis functions and then use a matrix of 18×18×18 basis functions. For the two human data sets, three resolution levels are also used: 64×64×50, 128×128×99, and 256×256×198 voxels for the first data set, and 64×64×25, 128×128×51, and 256×256×102 voxels for the second data set (the dimension depend on the dimensions of the original data sets). At the lowest level, 4×4×4, and then 8×8×8 matrices of basis function were used. At the intermediate level, we used first a matrix of 12×12×10 and then a matrix of 16×16×12 basis functions. At the highest resolution, we used 20×20×14, 26×26×16, and 32×32×20 matrices of basis functions. All those parameters were selected experimentally**.** Practically, parameters are determined once for one type of image and then used without modification to register similar images.

One feature that distinguishes our algorithm from others (see for instance Rueckert et al. [48]) is the fact that we do not work on a regular grid. Rather, areas of

mismatch are identified and the deformation field is adjusted only on these identified regions. This is done as follows. When the algorithm moves from one level to the other, a regular grid of basis function is placed first on the images. The gradient of the similarity measure with respect to the coefficients of the basis functions is then computed. The location of the basis functions for which this gradient is above a pre-determined threshold is used to determine areas of mismatch. The rationale for this choice is that if the gradient is low, either the images are matched well because we have reached a maximum or the information content in this region is low. In either case, trying to modify the transformation in these regions is not productive. Optimization is then performed locally on the identified regions (more details on this approach can be found in Rohde et al. [59]).

The algorithm progresses until the highest image resolution and highest scale are reached. Hence, the final deformation field **v** is computed as:

$$\mathbf{v}(\mathbf{x}) = \mathbf{v}_1(\mathbf{x}) + \cdots + \mathbf{v}_M(\mathbf{x}), \tag{17}$$

where M is the total number of levels. Furthermore, we compute both the forward and the backward transformations simultaneously, and we constrain these transformations to be inverses of each other using the method proposed by Burr [77]. Although this cannot be proven analytically, experience has shown that the inverse consistency error we achieve with this approach is well below the voxels' dimension. In our experience, enforcing inverse consistency improves the smoothness and regularity of the transformations.

One important objective of a non-rigid registration algorithm is to produce transformations that are topologically correct (i.e., transformations that do not include tearing or folding). This is difficult to guarantee and it is often implemented by constraining the transformation (e.g., adding a penalty term that is proportional to the

second derivative of the deformations field [48]). Here, we follow the same approach, but the field is regularized by constraining the difference between the coefficients of adjacent basis functions (the $\mathbf{c}_i$'s) using a threshold ε . The concept is simple: if the coefficients of adjacent basis functions vary widely, the resulting deformation field changes rapidly. This can be useful as it permits computing transformations that require large local displacements but it may also produce transformations that are ill-behaved. Thus, the threshold ε can be used to control the regularity and the stiffness properties of the transformation. Small values produce smooth transformations that are relatively stiff. Large values lead to transformations that are more elastic but less regular.

This threshold can also be used to vary spatially the properties of the transformations, which is of importance for the application described in this paper (in the past we have used the same technique to register images with large space-occupying lesions [60]). Indeed, there are two broad categories of structures in the images we need to register: bones and soft tissues. The amount of deformation typically observed for bony and soft tissue structures is very different and the transformations should reflect this fact; they should be stiffer for bony structures than for soft tissue structures. To create spatially varying stiffness properties, a stiffness map is generated. This stiffness map has the same dimensions as the original images and associates a value for ε with each pixel. In this work, we identify bony regions by thresholding the images as described earlier. We then associate a small ε value to bony regions and a large ε value to the other areas in the stiffness map. Experimentally, we have selected 0.01 for the bony region and 0.3 for the other regions, and we use these values for all the volumes presented here.

As described before, we have tested our method on two very different sets of data: small animal images and human images. When processing the small animal images, we need to add an additional step to our processing sequence. Indeed, mice are typically scanned in some type of holder and this holder needs to be eliminated prior to registration (see Fig. 18). Manual segmentation is time-consuming and impractical, considering the fact that one CT volume usually includes 512 slices. But automatic segmentation using common techniques such as thresholding is difficult. This is so because the intensity values of the mouse and of the holder are very similar and because the body of the mouse is connected tightly to the holder. Here, we solve the problem by segmenting the holder *via* registration. An empty holder is scanned and registered to the holder that contains a mouse using a normalized mutual information based rigid body registration algorithm. After registration, the image with the empty holder is subtracted from the image with the mouse and the holder. This results in an image, which only contains the mouse. Fig. 18 shows representative results in the sagittal, axial, and coronal orientations for a typical mouse CT image volume. The green region is the result of our holder segmentation method. This method is fully automatic and robust. It can be used with any type of holder provided that one image volume with an empty holder is available.

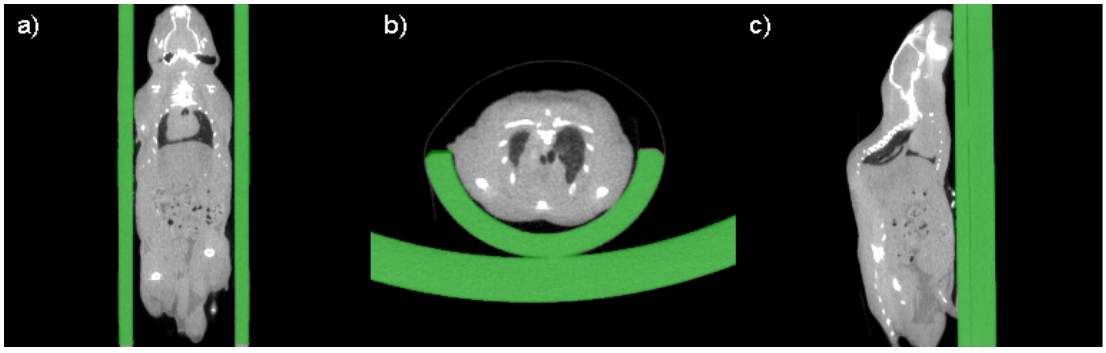

Fig. 18: The CT images with segmented holder. The holder is segmented automatically *via* a registration procedure.

4. Experiments and results

4.1 Qualitative results

Our approach has been qualitatively evaluated on three types of problems: intra-subject registration of whole body mouse images, inter-subject registration of whole body mouse images, and inter-subject registration of upper body human images. Examples of results obtained for each of these tasks are shown in this section.

Fig. 19a shows the skeletons extracted from two CT volumes. In the following text the volume deformed using our registration method is called the source volume while the other is called the target volume. Fig. 19b shows the results we obtain when we use only the ABA algorithm after the initial rigid body transformation. In this case, the algorithm is applied to the entire image volume, and the bones are extracted after registration. This figure shows that for this data set, an intensity-based nonrigid registration algorithm alone is insufficient to register the two volumes. Fig. 19c shows the results obtained after registering the skeleton with the point-based method alone. Fig. 19d shows the final results when the ABA algorithm is initialized with the results obtained in Fig. 19c. Results presented in this figure indicate that the point-based method leads to qualitatively good results, but that these results can be improved further with an intensity-based technique.

Fig. 20 presents similar results but on the entire volume; Fig. 20a shows one slice in the source volume and Fig. 20b shows the slice with the same index in the target volume. If the source and target volumes were perfectly registered, these images would be identical. To facilitate the comparison, yellow contours have been drawn on the target

image and copied on all the other ones. Fig. 20c shows the results when only ABA is used, Fig. 20d when only the point-based method is used, and Fig. 20e when both methods are combined. Comparing Fig. 20d and Fig. 20e it is clear that even if the bones are registered correctly with the point-based technique, the rest of the body is not. For instance, the contour of the lower portion of the mouse body shown in Fig. 20d is not aligned to the target accurately. Again, combining the two methods leads to results that are better than those obtained with a single method.

Fig. 21 and Fig. 22 show typical inter-subject registration results. In both these figures three pairs of images pertaining to different mice have been registered. Fig. 21 shows the registration of the skeletons. In this figure, the left column shows the skeletons in their original position. The middle and right columns show the same but after rigid body registration and after registration with the proposed method, respectively. Fig. 22 shows the results we obtain on the entire CT volume. The left column shows one slice in the source volume and the right column shows the same slice in the target volume. The middle column shows this slice in the source volume once it has been registered and reformatted to correspond to the target volume. Contours have been drawn on the target volume and superimposed on the reformatted source volume to show the quality of the registration.

Fig. 23 and Fig. 24 show results we have obtained when performing inter-subject registration of human upper torso CT images, and they illustrate the advantage of using two stiffness values. In both figures, panels a) and b) are the source images and the target images, respectively. Panels c), d) and e) show the source volume registered to the target volume using a stiff transformation, a very elastic transformation, and a transformation

with two stiffness values, respectively. In Fig. 23, only the bones are shown. In Fig. 24, the complete volumes are shown. When a stiff transformation is used, bones are deformed in physically-plausible ways. But the accuracy achieved for soft tissues is suboptimal (arrows on Fig. 24c). When a more elastic transformation is used, bones are deformed incorrectly (shown in Fig. 23d). Using two stiffness values permits transformations to be computed that lead to more satisfactory results for both the bony and soft tissue regions.

Fig. 25 illustrates results we have obtained with a set of head and neck images. Fig. 25a and b show one sagittal CT image in one of the volumes (the source) and the slice with the same index in the second volume (the target) prior to registration. The red contour has been drawn on the target image in order to facilitate comparison. Fig. 25c ~ e show results obtained with our intensity-based algorithm alone, results obtained with point-based registration alone, and results obtained when both approaches are combined, respectively. Fig. 25c shows typical results obtained when non-rigid registration algorithms can not be initialized correctly. The overall shape of the registered volume appears correct but bones have been deformed incorrectly. The result obtained with the point-based registration algorithm is relatively inaccurate, as shown in Fig. 25d. As can be seen in this panel, the shape of the head and its size are not the same as those shown in Fig. 25b. Similarly, the size of the vertebrae is incorrect. Fig. 25e shows that the best results are obtained when both approaches are combined.

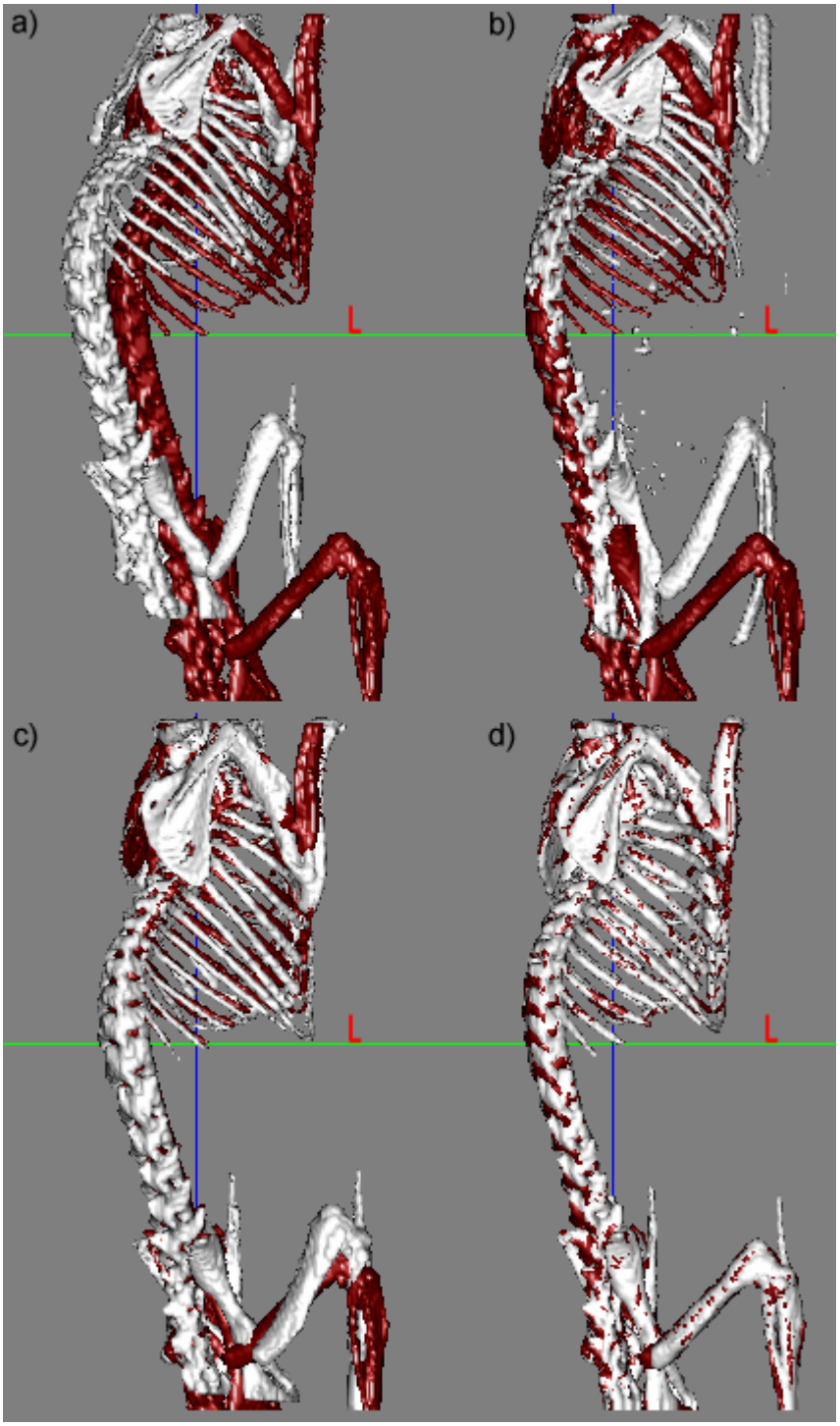

Fig. 19: Bony structures in two micro CT volumes a) before registration, b) after ABA registration only, c) using only the robust point-based registration algorithm, and d) using both the point-based registration and the ABA algorithms.

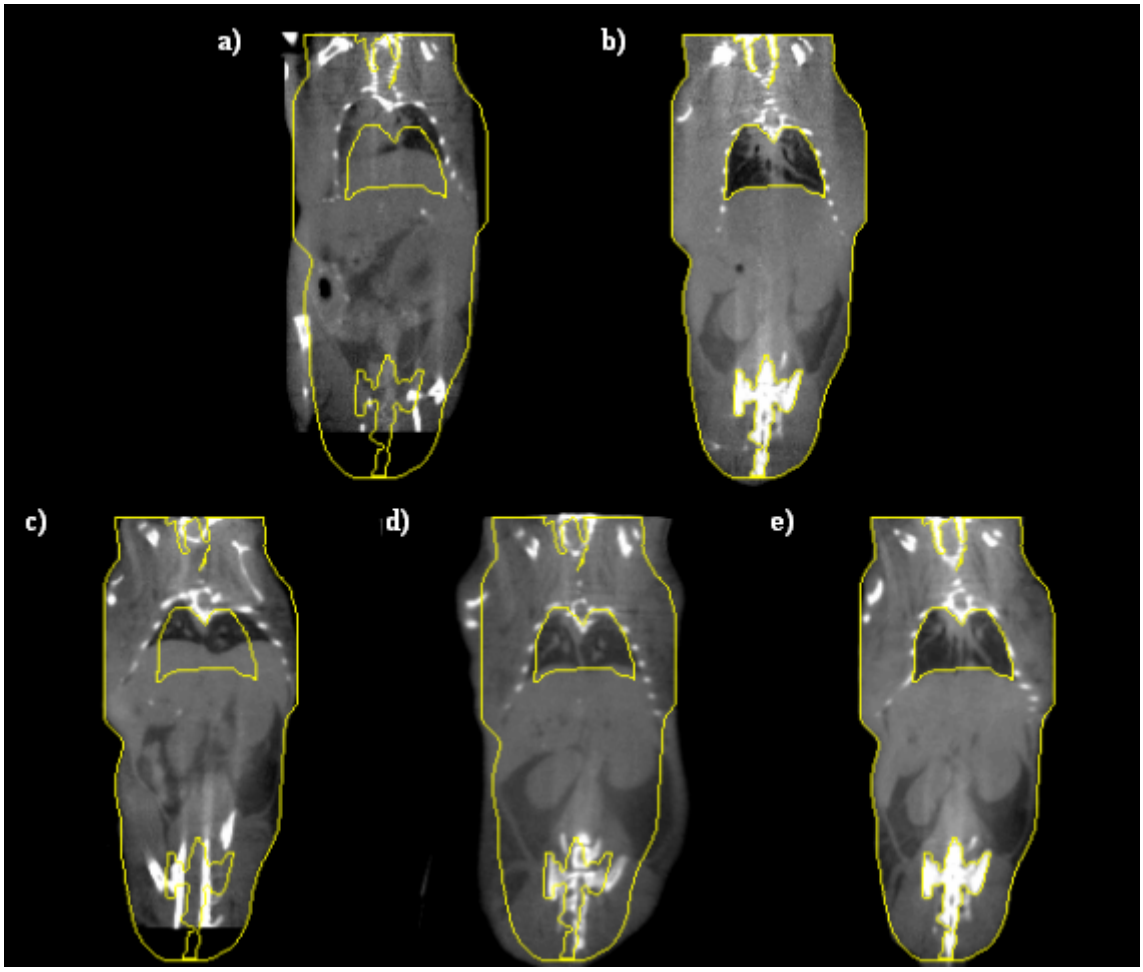

Fig. 20: a) One coronal slice in the source volume, b) the corresponding coronal slice in the target volume, c) the transformed source image after ABA only, d) the transformed image after robust point-based registration algorithm only, and e) the transformed image after the combination of the point-based registration and the ABA algorithms.

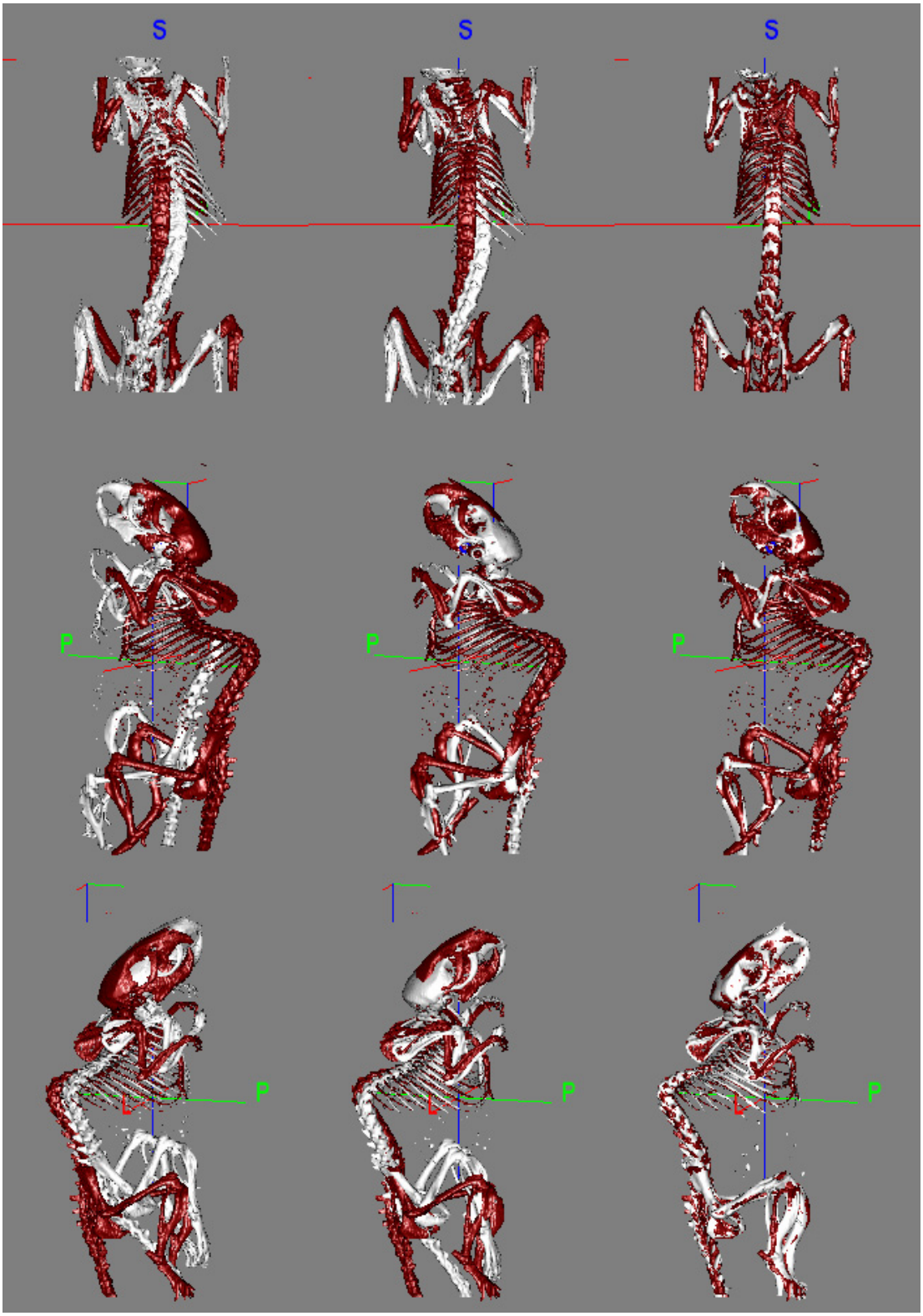

Fig. 21: Three pairs of inter-subject mice skeletons before registration (the 1st column), after the rigid body registration (the 2nd column) and the proposed method (the 3rd column).

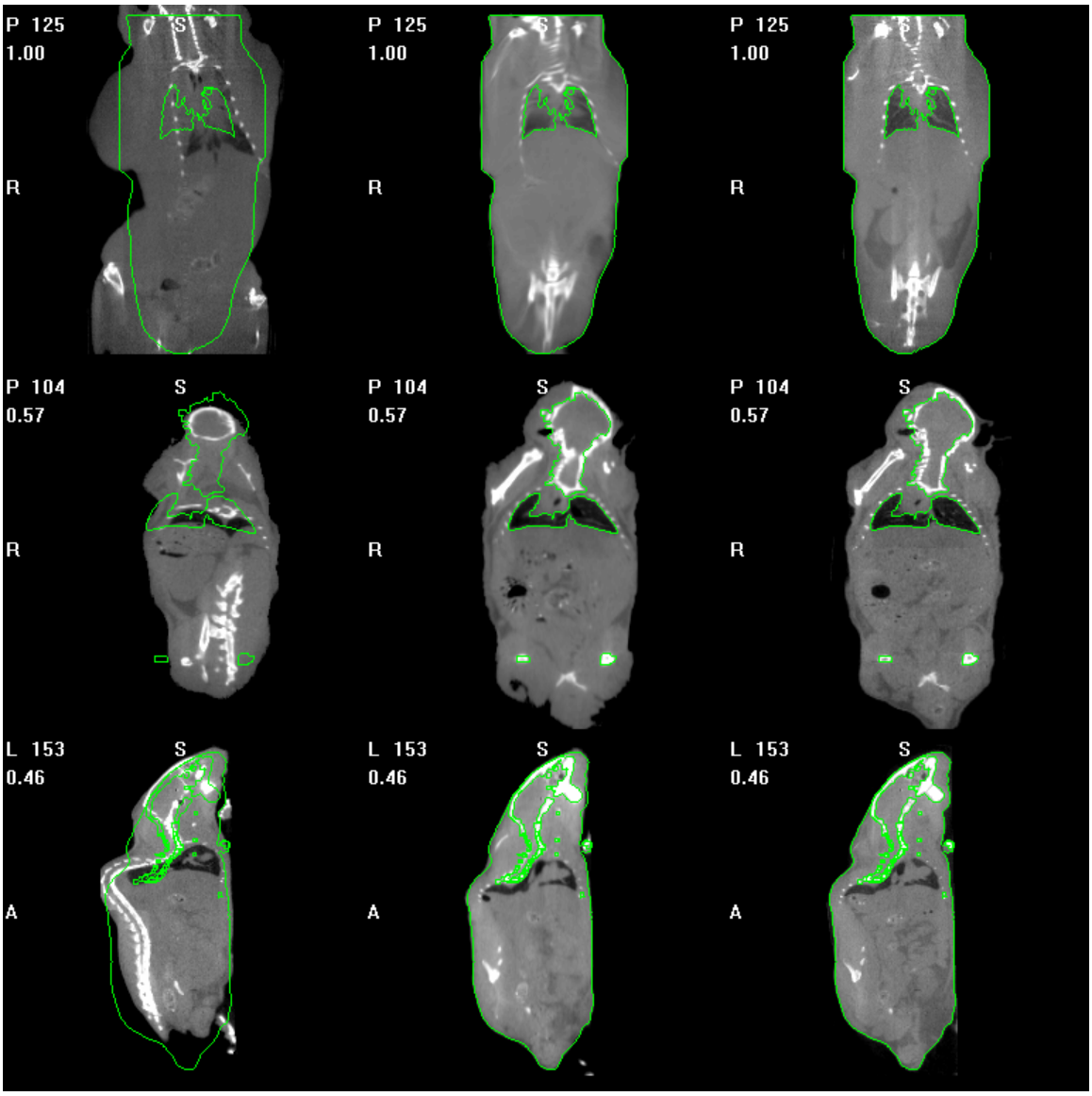

Fig. 22: The different slices from the three different reference mice (the 1st column), the deformed slices after the proposed method (the 2nd column) and the corresponding target mice (the 3rd column). The green lines are the contours of the target images.

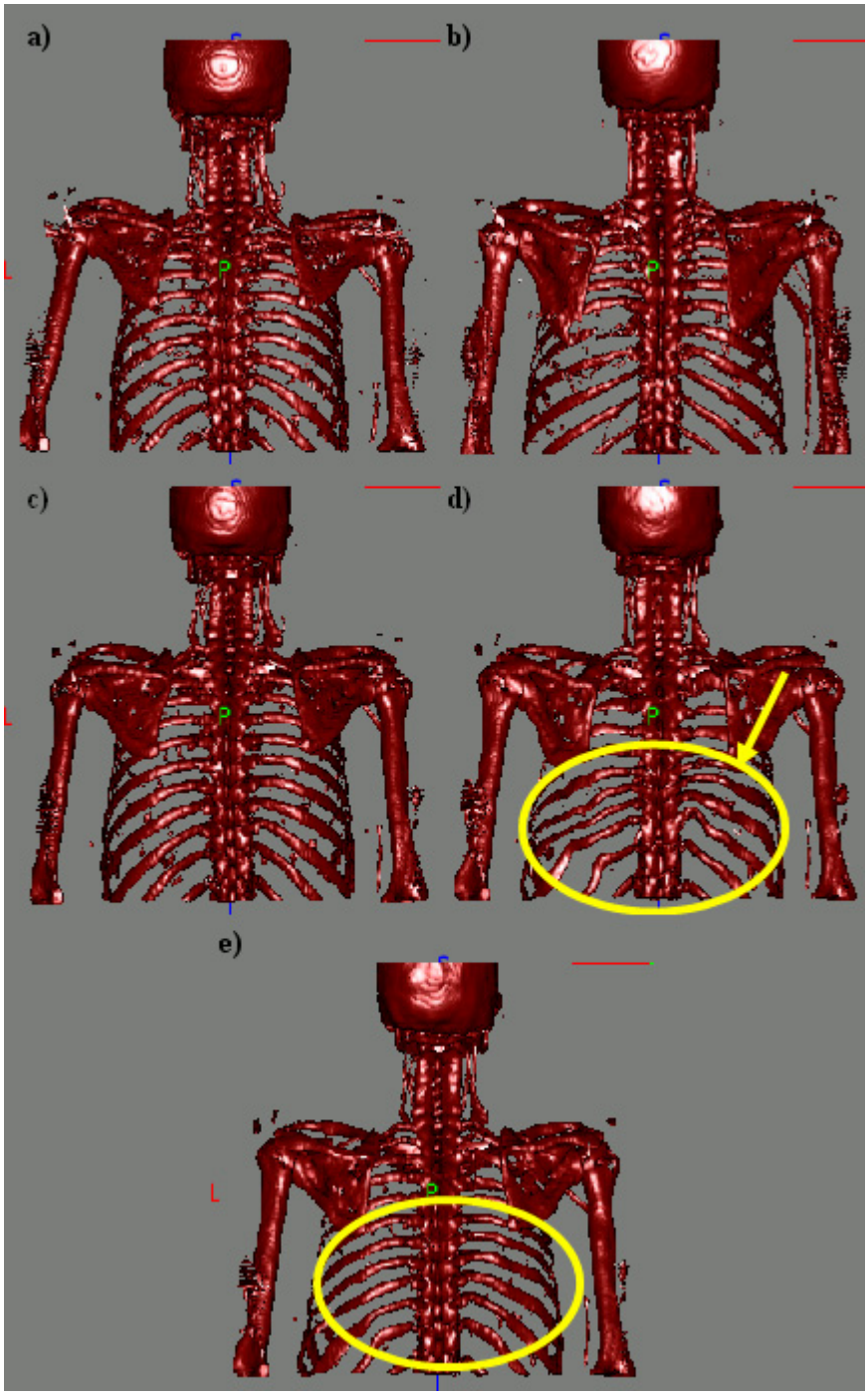

Fig. 23: a) Skeleton of the source image, b) skeleton of the target image. c), d), and e) source skeleton registered to target skeleton using a stiff transformation, a very elastic transformation, and two stiffness values, respectively.

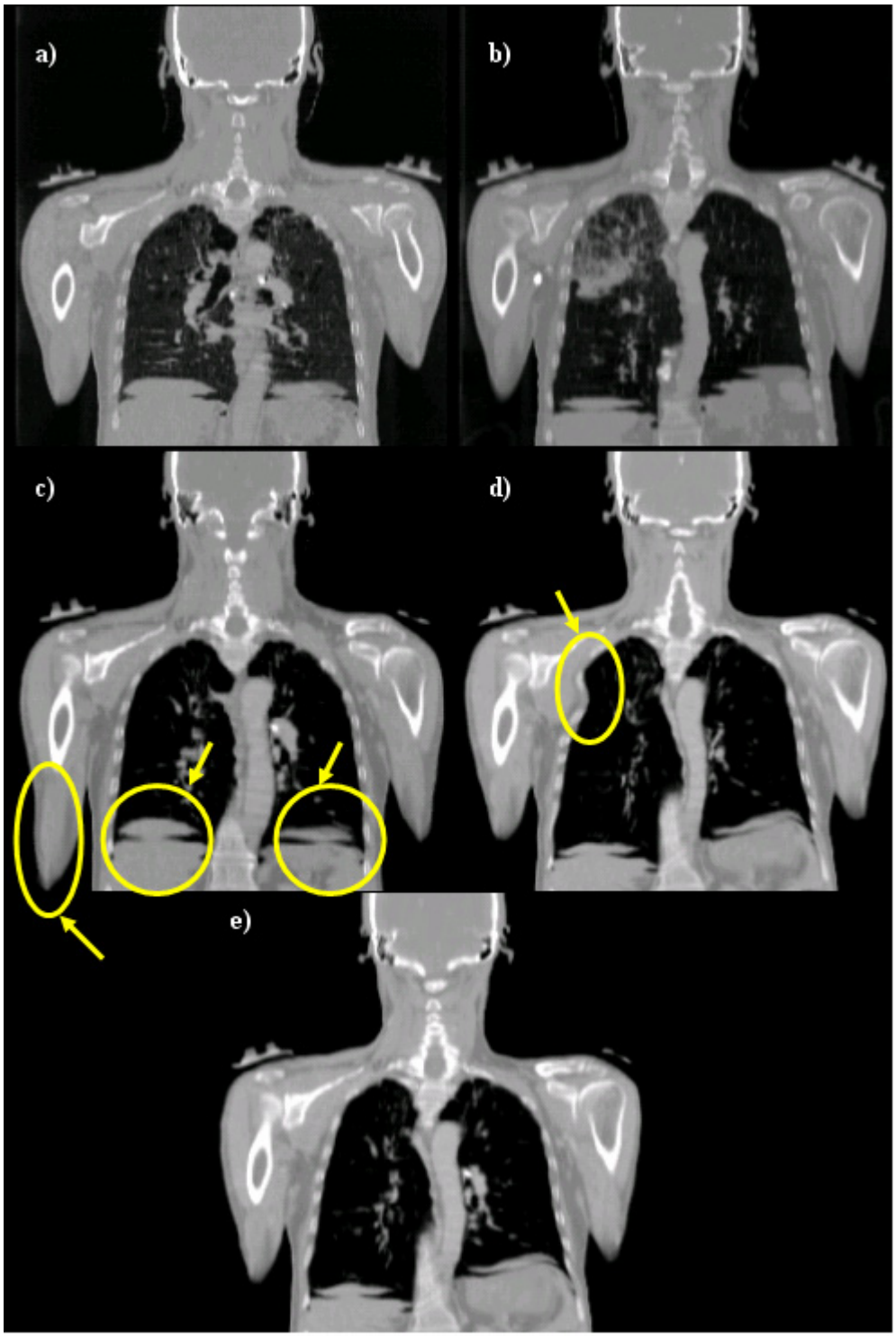

Fig. 24: a) One coronal slice in the source volume, b) corresponding slice in the target volume, c), d), and e) source image registered to target image using a stiff transformation, a very elastic transformation, and two stiffness values, respectively.

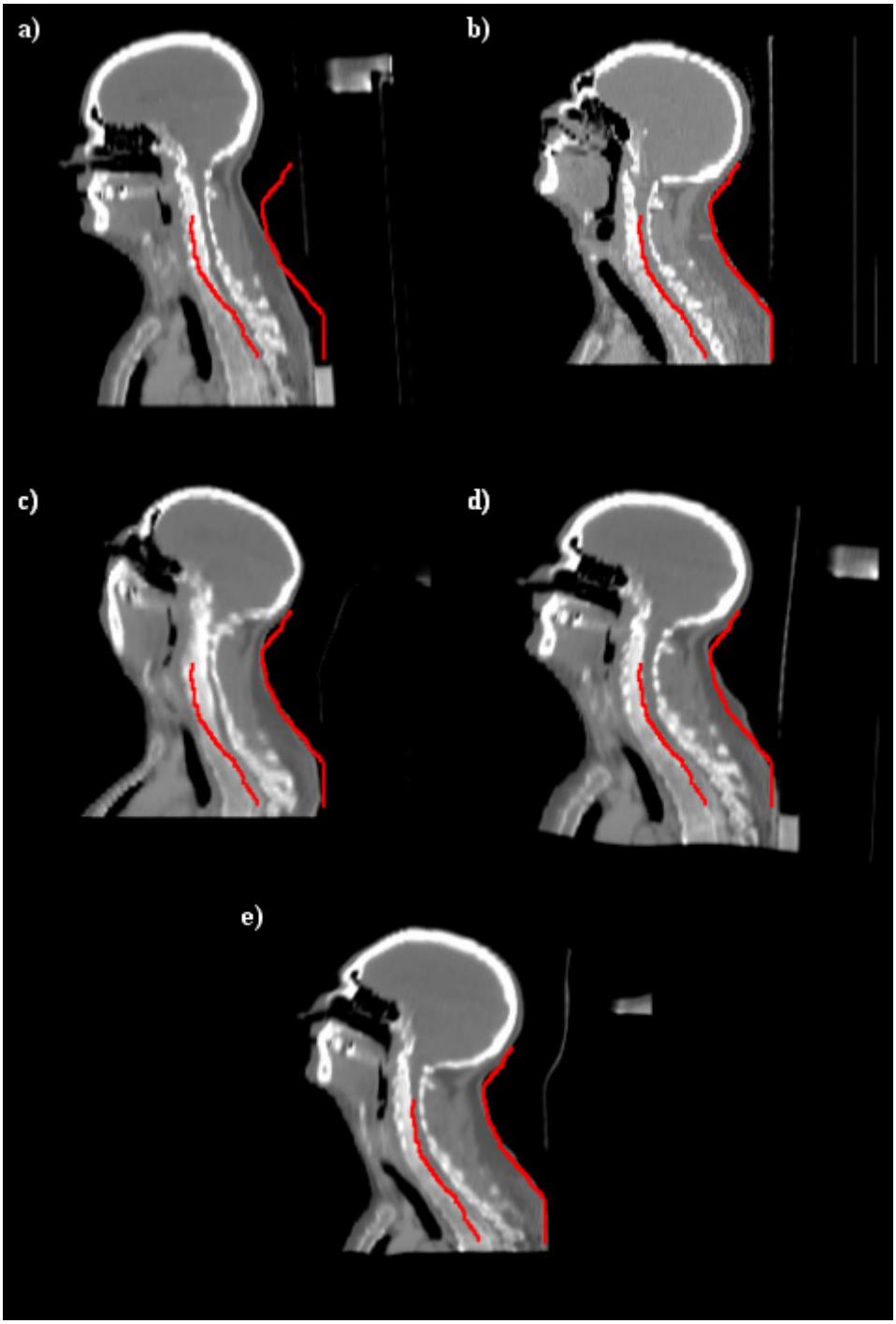

Fig. 25: a) One sagittal slice in the source volume, b) the corresponding slice in the target volume, c), d), and e) registration results obtained with intensities alone, points alone, and with the proposed algorithm, respectively.

Visual and qualitative validation of our approach indicates that it can be used to register whole body images. To validate this approach quantitatively, we have devised two experiments, one to test the algorithm on the skeletons and the other on soft tissue regions.

4.2 Quantitative Validation

The acquired data sets, described in Section 2, can be used to validate our method both on the skeletons and on soft tissue structures of the same mouse acquired twice in a different posture (longitudinal study) or of two different mice (inter-subject registration). We have 4 pairs of images to test our algorithm on intra-subject longitudinal tasks; e.g., mouse 1 acquired at time 1 is paired with mouse 1 acquired at time 2, etc. With the data set we have acquired, 24 pairs of images can be created to validate our algorithm on inter-subject tasks; i.e., mouse 1 at time 1 can be paired with mouse 2 at time 1, with mouse 2 at time 2, etc. Among these 24 pairs, 7 had to be eliminated because one of the data set covered the entire body while the other was missing the lower legs. This leaves us with 17 pairs of images to perform our inter-subject evaluation.

Because of acquisition artifacts, the boundary between the heart and the lungs could not be seen at all in one of the mice (mouse #3) CT volumes. In turn, this led to an inaccurate registration in this region when CT images alone were used. For this reason, mouse #3 was omitted for the quantitative evaluation of the heart. Validation results on both skeletons and soft tissues are reported in the following sections.

Validation on skeletons

To validate the algorithm on skeletons, the distance between each point on the deformed source surface and the closest point on the target surface is computed. Table II shows these distances at each step of the algorithm for both the longitudinal and the inter-subject registrations tasks. Hence, the distances are calculated before and after the rigid body registration, after the point matching algorithm, and after the intensity-based nonrigid registration. After the proposed algorithm, the mean distance for the intra-subject registration task is 0.24 mm. It is 0.3 mm for the inter-subject registration task. Because the inter-registration task involves accounting for morphological differences in addition to pose differences, observing a slightly larger error for the second task is to be expected.

Table II: Distances in mm between the source and target bone surfaces before rigid registration, after rigid registration, after registration using points only, and with the method we propose for both the intra- and inter-subject registration tasks.

		Before Rigid	After Rigid	After Point Matching	Proposed Method
Intra-subject	#01	1.7667	0.8175	0.4854	0.3008
	#02	0.6254	0.4151	0.3853	0.3290
	#03	0.8205	0.6778	0.2542	0.1422
	#04	0.7757	0.7164	0.4128	0.2080
	Mean	0.9971	0.6567	0.3844	0.245
Inter-subject	#01	2.4047	1.0170	0.7313	0.4368
	#02	2.2495	0.4799	0.4964	0.1769
	#03	1.5536	0.9060	0.5390	0.2530
	#04	1.0805	0.5425	0.5289	0.2054
	#05	2.6875	0.5525	0.464	0.2433
	#06	2.5321	0.5983	0.5878	0.3550
	#07	2.1083	0.6605	0.7416	0.3255
	#08	1.2474	0.6147	0.5736	0.2330
	#09	0.7904	0.5203	0.6069	0.2496
	#10	1.3014	1.2376	0.4989	0.3300
	#11	1.1262	1.0090	0.4056	0.2666
	#12	3.1736	1.0154	0.5111	0.3314
	#13	2.8424	1.0267	0.5936	0.3795
	#14	1.9231	0.8696	0.5501	0.3168
	#15	2.1204	0.9429	0.5337	0.2999
	#16	2.4757	0.9207	0.6521	0.3734
	#17	2.2350	0.7434	0.5715	0.3370
	Mean	1.9913	0.8034	0.5639	0.3008

Validation on soft tissue structures

The approach we have used to test our registration method on soft tissues both for the intra-subject and the inter-subject registration tasks is as follows.

Step (1): each MRI scan was registered to its corresponding CT scan with a rigid transformation;

Step (2): CT scans were then registered using the method we propose;

Step (3): the transformation computed in Step (2) was applied to the MRI scans. This permits evaluating the quality of the CT-based registration on structures that are not clearly visible in the CT images.

The heart, kidneys, and bladder were segmented manually in all the MR image volumes. The transformations that register the source to the targets were then applied to the structures segmented in the source image. This produced deformed structures that were compared to the segmented structures in each of the target images using the Dice similarity index [62] defined as:

$$\text{Dice Similarity} = 2 \times \frac{n\{A_1 \cap A_2\}}{n\{A_1\} + n\{A_2\}}, \tag{18}$$

where A_1 and A_2 are two regions and $n\{\}$ is the number of voxels in a region. Fig. 26 shows a few examples with manual and automatic contours superimposed. It also shows the value of the Dice index computed for these various cases to provide a sense of the correlation between the Dice value and the visual quality of the segmentation. As mentioned in the previous chapter, a value of 0.7 for the Dice value is generally accepted as a value for which two contours are in very good correspondence [80].

Two observers have segmented soft tissue structures in the images. Hence, three Dice values are computed and compared: the Dice value between the automatic contours and the manual contours drawn by the first observer, which we call AM1; the Dice values between the automatic contours and the manual contours drawn by the second observer, which we call AM2; and the Dice values between the contours drawn by the two observers, which we call M1M2. The value of the Dice similarity measure between two observers quantifies the inter-rater variability that can be expected for the various segmentation tasks. Although, as discussed above, our main objective is to develop a method for the registration of CT images, we also investigated whether or not using the MR images in the registration process would improve the results. To do so, we added one registration step. After the MR images have been registered to each other using the transformation generated to register the CT images, we registered them once more with the ABA algorithm.

Table III lists the Dice values for the longitudinal registration task with and without the last MR registration step. Our results show that Dice values are above 0.7 for the longitudinal registration task. Moreover, the Dice values between the automatic and manual contours are comparable to the Dice values between the two observers, which indicates that the variability between manual and automatic contours is similar to the variability observed between human raters. Fig. 27 and Fig. 28 show the results for the inter-subject registration tasks. For both the intra- and inter-subject registration tasks, the Dice values improve when the MR images are used. We also note that the bladder is the most difficult structure to register because of large inter-subject differences. This is most likely due to the volume of urine that is present in the bladder at the time of imaging.

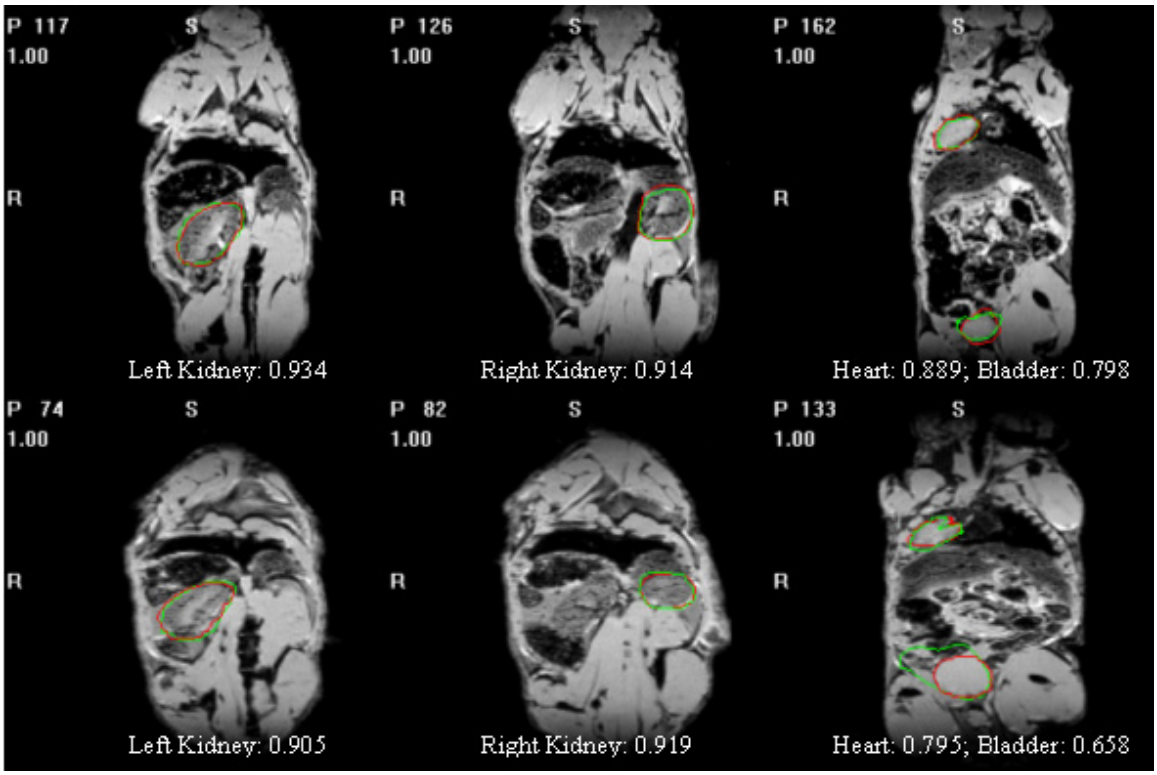

Fig. 26: The target images overlaid with contours of automatically segmented tissues in the deformed images (green) and contours of manually segmented tissues in the target images (red).

Table III: Dice similarity values between the two manual segmentations (M1M2), between the first manual segmentation and the automatic segmentation (AM1), and between the second manual segmentation and the automatic one (AM2) for the intra-subject registration task.

			Heart	Left Kidney	Right Kidney	Bladder
The proposed method	#1	AM1	0.9040	0.9150	0.8730	0.8120
		AM2	0.7997	0.8374	0.7699	0.7213
		M1M2	0.8758	0.9033	0.8958	0.8907
	#2	AM1	0.8530	0.8930	0.8840	0.8860
		AM2	0.8518	0.8926	0.8649	0.8529
		M1M2	0.8624	0.8810	0.8721	0.8707
	#3	AM1		0.8820	0.8520	0.7100
		AM2		0.8710	0.9103	0.7708
		M1M2		0.8966	0.8706	0.8364
	#4	AM1	0.8930	0.8900	0.8860	0.8040
		AM2	0.8684	0.9080	0.8646	0.7752
		M1M2	0.8458	0.9152	0.8878	0.8869
	Mean	AM1	0.8833	0.8950	0.8738	0.8030
		AM2	0.8400	0.8772	0.8524	0.7801
		M1M2	0.8613	0.8990	0.8816	0.8712
The extra step	#1	AM1	0.9220	0.9090	0.9180	0.7730
		AM2	0.7714	0.8055	0.7582	0.7393
		M1M2	0.8758	0.9033	0.8958	0.8907
	#2	AM1	0.9200	0.9230	0.9330	0.9510
		AM2	0.8987	0.9114	0.9002	0.8802
		M1M2	0.8624	0.8810	0.8721	0.8707
	#3	AM1		0.9040	0.8890	0.7650
		AM2		0.8965	0.9111	0.8020
		M1M2		0.8966	0.8706	0.8364
	#4	AM1	0.9160	0.9120	0.9230	0.8980
		AM2	0.8765	0.9212	0.8984	0.8553
		M1M2	0.8458	0.9152	0.8878	0.8869
	Mean	AM1	0.9193	0.9120	0.9158	0.8468
		AM2	0.8489	0.8837	0.8670	0.8192
		M1M2	0.8613	0.8990	0.8816	0.8712

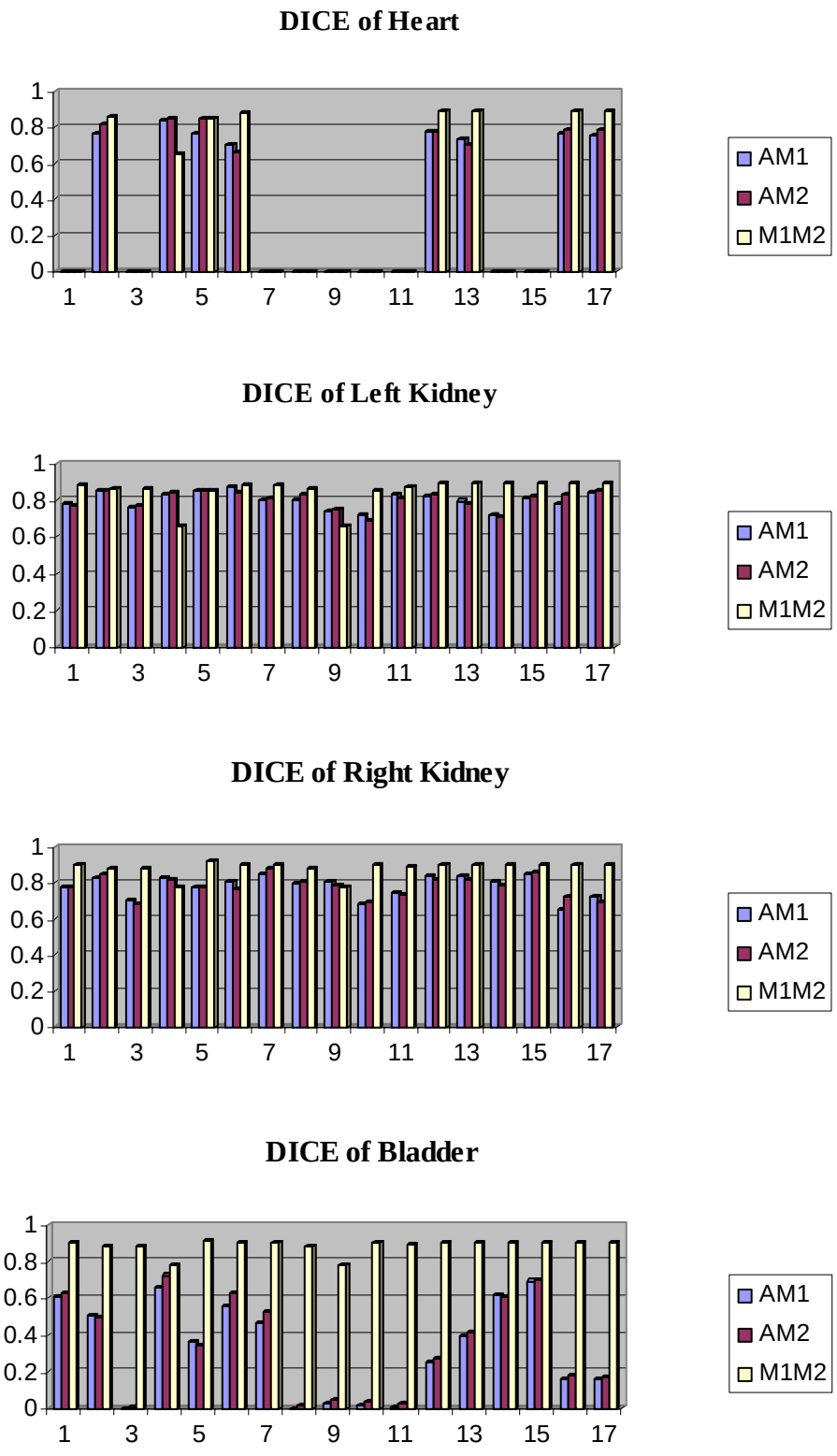

Fig. 27: Dice values for the inter-subject registration task without the last MR registration step.

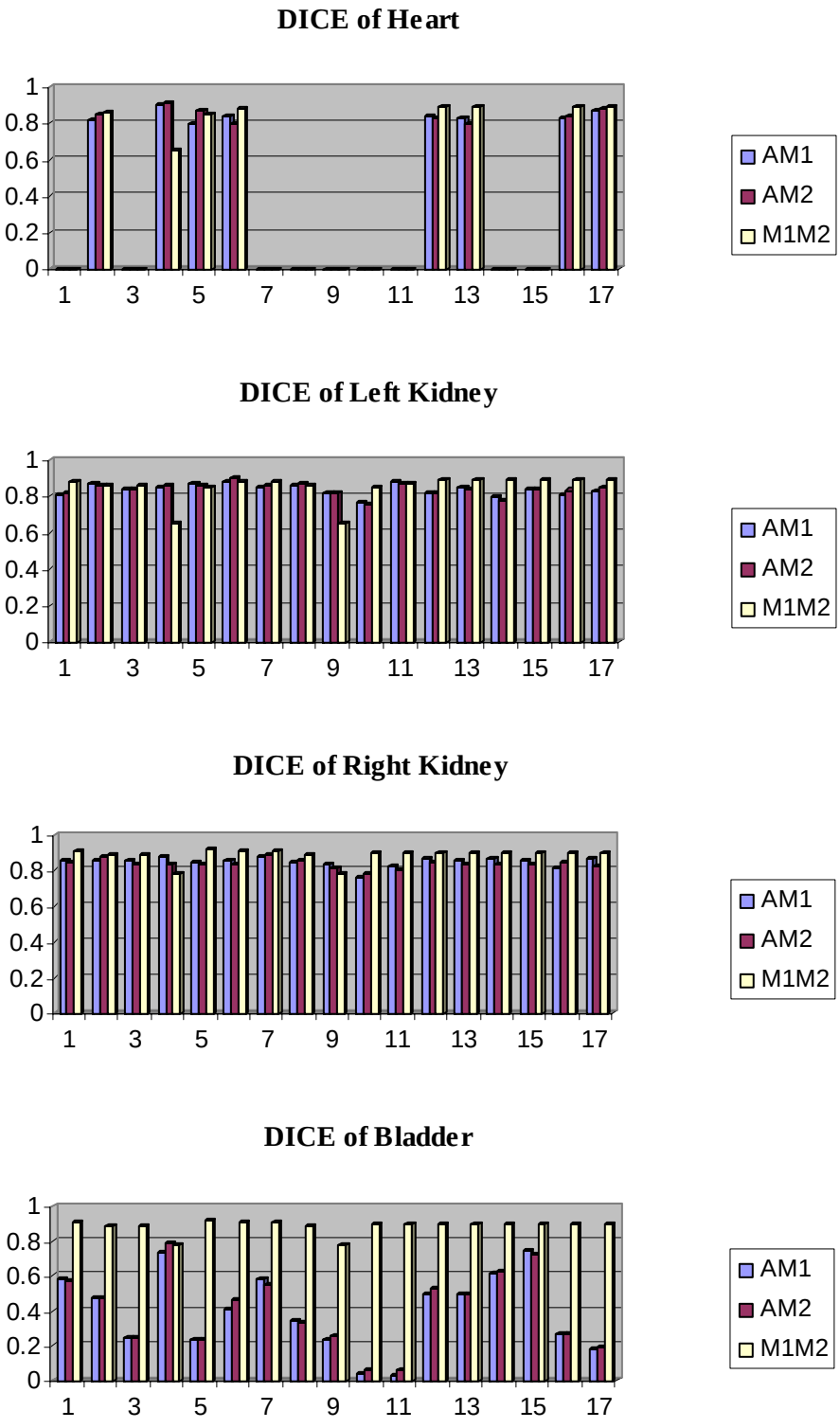

Fig. 28: Dice values for the inter-subject registration task with the last MR registration step.

5. Discussion and Conclusions

In this paper, we presented a novel and fully automatic approach for the registration of articulated structures applicable to intra- and inter-subject registration problems. While it may appear, at first, that registering articulated structures would require computing individual transformations for each element in the structure and combining these transformations, our experiments show that it is not the case. This is what differentiates our work from previously published work and it may have a significant impact because it greatly simplifies the solution to the problem. In particular, segmentation and identification of individual structure components is no longer necessary.

Results have shown that, while accurate registration of bony structures is possible with a robust point-matching method, registration of the entire volumes requires a second step. If, as is done in this work, the second step is based on an image intensity algorithm, special care needs to be taken to constrain the transformation locally to avoid deforming the bony structures inappropriately while registering the rest of the image volumes. Here we have addressed the issue with what we call stiffness maps that constrains the relative value of the coefficients of adjacent basis functions. We have found this scheme to be particularly useful for human images but less so for small animal images. This is so because basis functions have a pre-determined support and may cover a region that contains both bones and soft tissue; this is especially true for small animal images in which bones are small compared to the voxel dimensions. In the current version of our non-rigid registration algorithm, we use the position of the center of the basis function to determine its constraint which may produce inaccuracies; i.e., soft tissue close to the bones may not be deformed enough if the basis functions are centered on a bony structure

or bones may be deformed too much if the basis function is centered on soft tissue. We are currently addressing this issue by adding an additional constraint in our algorithm that will prevent this from happening. This strategy is introduced in Chapter IV in detail.

The results we have obtained on the skeletons show a submillimetric error for both the serial and the inter-subject registration task. The Dice values we have obtained with our approach using only CT images for the intra-subject registration task indicate an excellent agreement between manual and automatic contours. These results indicate that the method we propose could be used for longitudinal measurements using only CT images. A possible issue, which will need to be investigated further, is the effect a growing tumor will have on the intensity-based component of our approach. The possible solution will be discussed in the next chapter. The inter-subject registration results we have obtained imply that CT images alone, with their relatively poor soft tissue contrast, may not be sufficient to produce registrations that are accurate enough to measure small differences. Using MR images in addition to the CT images does, however, address the issue. One also notes that using MR images alone is unlikely to produce accurate results. Indeed, the skeletons that are easily identifiable in the CT images need to be used to produce transformations that are accurate enough to initialize MR-based registration algorithms.

Although we have focused our work on CT images of small animals, the results we present also show that the approach we propose is widely applicable. For instance, we have shown, albeit on a few cases, that it can be used for the registration of chest and head and neck images. Further evaluation on a larger data set will need to be performed to establish the robustness of our approach to this type of problem.

For the small animal studies, the average runtime of the robust point matching algorithm is 171 minutes. The average runtime of the adaptive basis algorithm is 89 minutes. All algorithms are run on a 2GHz Pentium PC with 1G memory.

CHAPTER IV

CONSTRAINED NON-RIGID REGISTRATION FOR WHOLE BODY IMAGE REGISTRATION: METHOD AND VALIDATION

1. Introduction

Medical image registration is an important tool in clinical research. Currently, the large majority of automatic methods that have been proposed have been applied to head images, because head images only contain one single major structure (the cranium). Non-rigid registration techniques for extra-cranial applications have been proposed for specific tasks, such as the registration of breast, abdomen, lung, or prostate images (see for instance [47][48][70]). But, as discussed earlier, very few methods have focused specifically on registering images that contain a large number of articulated structures, the relative position of which changes between images. These images pose a special challenge, because a single affine transformation is typically insufficient to initialize non-rigid registration algorithms.

In Chapter III we have reviewed methods that have been proposed to solve this problem and we have seen that they fall in one of the following categories: (1) applying a rigid body transformation to the rigid objects, followed by the interpolation of the deformation field to the entire image [49], (2) labeling landmarks manually in the images, aligning those landmarks in a piecewise fashion, and combining the elementary transformations [50], (3) identifying each single joint manually and then computing a continuous transformation at the interfaces of the piecewise transformations [52], (4) using a finite element method to propagate displacements, after articulating a set of rigid

body matrices [72], (5) matching both manually identified landmarks and the areas away from the landmarks through the Consistent Landmark and Intensity Registration Algorithm (CLI-TPS) [73], and (6) utilizing a hierarchical anatomical model of the mouse skeleton system for the articulated registration of 3D whole body data of mice [78].

Chapter III has discussed these solutions and their disadvantages. In a word, most existing methods require identifying various structures in the images such as joints or individual bones. Unfortunately this approach is often not practical. In Chapter III we also proposed a novel and automatic registration algorithm for whole-body images, which combines point-based and intensity-based registration algorithms [81][82] for CT images. In this fully automatic algorithm the skeletons are first aligned non-rigidly using a point-based registration algorithm, which provides a good initial position for the intensity-based registration step used next. Despite the very good results we have obtained with this approach, one weakness was identified: during the intensity-based registration step, bones can be deformed inaccurately because of surrounding structures. In this chapter, we present a modification of the previously proposed algorithm to constrain the displacement of bony structures. Results show that this improves the performance of our approach.

The remainder of this chapter is organized as follows. The constrained algorithm we propose is introduced and discussed in detail in the method section. The qualitative and quantitative results generated by both the new and the previous methods are reported and compared in the validation section. The algorithm and the results we have obtained are discussed in the last section.

2. Methods

The algorithm discussed in Chapter III contains three main parts: intensity-based rigid body registration, point-based nonrigid registration, and intensity-based nonrigid registration. An additional pre-processing step is used to eliminate the holders in small animal images. For the sake of completeness, this algorithm is covered rapidly in this section before we provide more details on the additional constrain scheme we propose.

In the pre-processing step the mouse body is segmented from the holder in which it is scanned. This segmentation task is difficult because the intensity values of the mouse and of the holder are very similar, and usually the mouse body is tightly connected to the holder. Manual segmentation is time-consuming, and thresholding or region-growing methods do not work well for this application. We solve the problem by segmenting the holder *via* registration. An empty holder is scanned and registered to the holder that contains a mouse using a mutual information based rigid body registration algorithm. The holder is then segmented by subtracting it from the image set that contains both the holder and the mouse.

In the previous algorithm, the first step consists in applying an MI-based rigid body registration algorithm to the source and target CT images. Hence, the rotation and translation parameters are calculated by maximizing the normalized mutual information between the two images.

Next, the skeleton is segmented using an intensity threshold. For each axial slice in the skeleton volume, the connected areas are detected and the center of each area is located. The set of central points approximately corresponds to the centerline of the skeleton, and they are used as input for the next step.

The sets of points extracted from the source and the target images are then registered using the RPM algorithm proposed by Chui et al. [74]. This algorithm takes as input two sets of points and iteratively computes a correspondence between these points and the transformation that registers them. Furthermore, a parameter, called the temperature T, is introduced to simulate physical annealing. T is set at a high value at the beginning, in order to generate a fuzzy correspondence between the two sets of points. The fuzziness of the correspondence is progressively reduced by decreasing T, and the transformation is computed iteratively. Finally, the transformation computed based on the points is applied to the entire image volume. This deformed volume is then used as input to the next step.

The last step in the previous method relies on an intensity-based registration algorithm we have proposed before, which we call ABA for adaptive bases algorithm [59], to refine the results. This algorithm models the deformation field v(x) that registers the two images as a linear combination of radial basis functions (RBFs) with finite support:

$$\mathbf{v}(\mathbf{x}) = \sum_{i=1}^{N} \mathbf{c}_i \Phi(\mathbf{x} - \mathbf{x}_i) \tag{19}$$

where Φ is one of Wu's compactly supported radial basis functions. The $c_i's$ are coefficients for these basis functions. The coefficients of the radial basis functions are computed through maximizing the Normalized Mutual Information.

There are two broad categories of structures in the images we need to register: bones and soft tissues. The amount of deformation typically observed for bony and soft tissue structures is very different, which suggests using transformations whose physical

properties vary spatially. These transformations should be relatively stiffer for bony structures than they are for soft tissue structures. In the previous method, one mechanism in the ABA algorithm is used to adjust the stiffness of the transformation, i.e., we impose a threshold on the difference between the coefficients c_i's associated with adjacent radial basis functions. The smaller the threshold, the stiffer the transformation is. To create spatially varying stiffness properties, stiffness maps are generated, which specify threshold values for various regions. An example of such a map is shown in Fig. 29. The bright area, which corresponds to bony structures, is associated with a small threshold; the dark area, which corresponds to soft tissue, is associated with a large threshold. While we have shown in Chapter III that this mechanism could indeed control the spatial properties of the transformation and improve registration results, this mechanism is imperfect. The right panel of Fig. 29 illustrates problems we have encountered. The value of the threshold is associated with the spatial location of the basis function. If, as is the case for the skeleton of small animals, regions associated with high stiffness values are narrow, very few basis functions will fall in high stiffness regions. As a result, the transformation will not be constrained as intended and bony structures will be deformed.

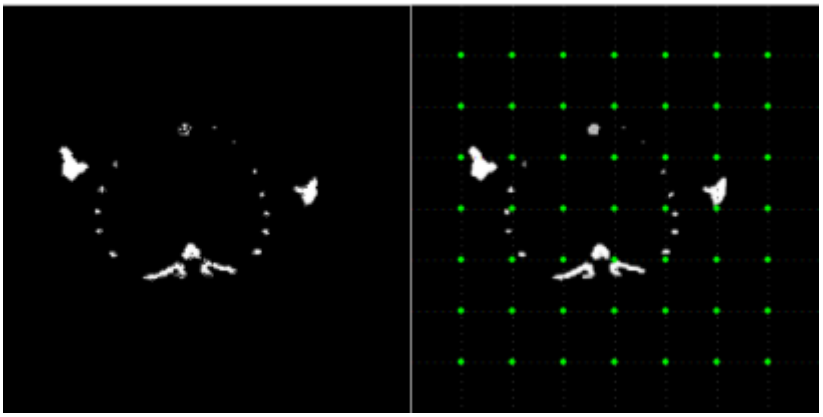

Fig. 29: The bony structures and the control points (green) on the image.

We note that others have proposed solutions to the same problem. Staring et al. [83] add a regularization term into the cost function. This term contains three conditions to keep a deformation rigid: linearity, orthonormality and properness. B-spline basis functions are used to parameterize the deformation. They apply this algorithm to CT and Digital Subtraction Angiography (DSA) images. However, if the rigid object is narrow, they need to dilate the object to make sure the control points of the B-splines are laying in the constrained regions. Ruan et al. [84] propose a cost function that includes a similarity term and a regularization term. In their regularization term, the local Jacobian of the deformation is constrained to be a nearly orthogonal matrix in rigid regions. But the quantitative evaluation of this approach on small animal images is lacking.

The approach we propose is as follows. Following the RPM algorithm, we first apply the ABA algorithm to the whole bony structures alone; this refines the results obtained with the RPM algorithm. The transformation computed based on the bony registration is then applied to the entire image volume. A constrained ABA algorithm with a new cost function is then applied to the entire volume. Instead of using only the negative of the NMI, the new cost function consists of two terms: a negative NMI term and a constraint term which is computed as the mean displacement of all bony pixels:

$$F_{\text{cost}} = -\frac{H(A)+H(B')}{H(A,B')} + \lambda \frac{1}{N}\sum_i \sqrt{dx(p_i)^2 + dy(p_i)^2 + dz(p_i)^2} \qquad (20)$$

where $H(\cdot)$ is still the entropy of the image, and $dx(p_i)$, $dy(p_i)$, and $dz(p_i)$ are the displacement of the voxels p_i on the skeleton, in the x, y, and z directions, respectively. λ is the parameter we use to weigh the second term. To minimize this cost function, the

algorithm thus needs to limit the deformation of the bony structures while maximizing the similarity between images in the soft tissue region.

3. Validation

In the following sections we present resutls we have obtained with our algorithm. First, we focus on the qualitative validation of the method. To do this, we use one data set that illustrates the advantage of our method for the analysis of image volumes in which changes occur over time. A male C57BL6 mouse was scanned with an Imtek MicroCAT II small animal scanner to generate one CT volume. CT imaging was at a voltage of 80kvp with an anode current of 500μA. Acquisition parameters of total 360^{o} projections in 0.632^{o} steps, exposure time 1400ms, and acquisition matrix 512×512×512 were employed. Total scan time is 22 minutes, and images have $0.125\times0.125\times0.125$ mm^3 isotropic voxels. The scans covered a region extending from the lower neck to about half of the back limbs. Next, approximately, 10^6 Lewis Lung Carcinoma (LLC) cells were injected through the tail vein of the mouse. This mouse with LLC tumor was imaged one more time eight days later on the microCT scanner, under the same imaging protocol described above.

The quantitative validation has been performed on the same data set that was used in the previous chapter. Four sacrificed mice were scanned twice. Each time we have obtained co-registered MR and CT scans and the position of the mice in the holder was modified between acquisitions. We report results we have obtained both for longitudinal and inter-subject registration tasks.

3.1 Qualitative Validation

Fig. 30 shows the skeletons before and after registration for the mouse with a lung tumor. The left panel of Fig. 30 shows the skeletons extracted from the first (bright) and the second (dark) CT volumes before registration. The right panel of Fig. 30 shows the registration result we obtain after we use the constrained algorithm we propose.

To examine the effectiveness of the constrained algorithm in detail, six different registration methods are applied to the mouse CT images and compared: (1) the ABA algorithm only, (2) the RPM algorithm only, (3) the ABA algorithm after the RPM algorithm, (4) the ABA algorithm with the stiffness map after the RPM algorithm, (5) the ABA algorithm with the stiffness map after the RPM and ABA applied to the bones, and (6) the new constrained ABA algorithm after the RPM and ABA applied to the bones. In these six methods, exactly the same parameters except for the constraint definitions have been used. Chapter III has described methods 1 – 4 and methods 5 – 6 are new strategies proposed in this chapter.

Fig. 31 shows the flowchart for the six methods. After the source data is pre-processed and transformed to the target volume using the rigid body registration algorithm, the six different methods are applied to it. In this figure, *ABA* means the ABA algorithm without stiffness map. *ABA_msk* means the ABA algorithm with the stiffness map as used in the previous chapter. *ABA_b* is the ABA algorithm applied only to the bones. The transformation computed after this step is applied to the entire volume. *ABA_con* is the ABA algorithm with the new constraint. Results obtained with these six methods are shown in Fig. 32 and Fig. 33.

The first two panels in Fig. 32 are the source and target images, respectively. Because of the tumor in the target image (marked by the circle in Fig. 32(b)), the ribs in the reference image are deformed and incorrectly attracted to the tumor, when method 1, 3, 4 and 5 are used (Fig. 32 (c), (e) ~ (g)). Because we apply method 2 (panel (d)) only to the bony structure, the ribs are not affected by the tumor. However, both the soft tissues and the bones are not registered accurately. The modified ABA algorithm keeps the ribs in place while registering the soft tissue areas (Fig. 32 (h)).

Fig. 33 shows the skeletons that correspond to the images shown in Fig. 32. This figure also shows that method 1, 3, 4 and 5 distort the mouse ribs incorrectly (shown in Fig. 33 (c), (e) ~ (g)), even if a very small stiffness parameter is used in the mask. Method 2 aligns the skeletons roughly (Fig. 33(d)). The modified ABA algorithm is the only one that preserves the shape of the ribs (Fig. 33 (h)).

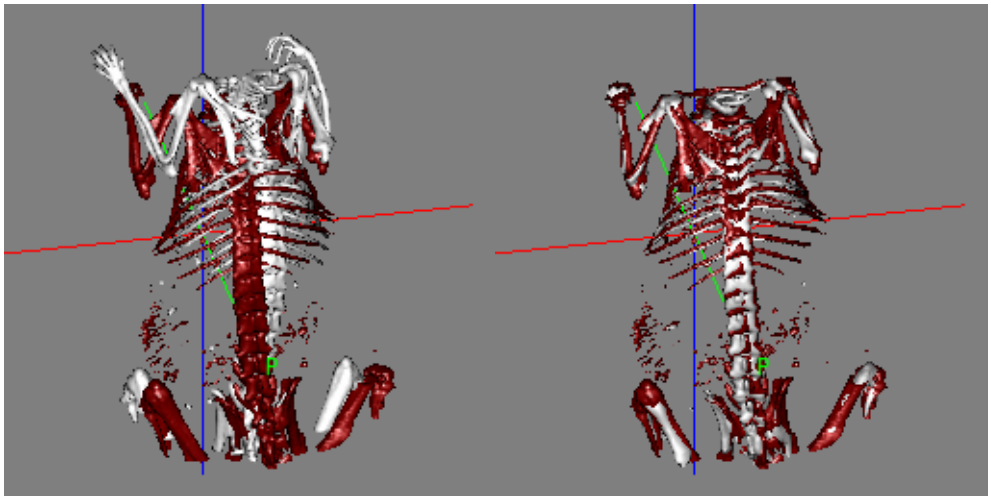

Fig. 30: Bony structures in two micro CT volumes before registration (left) and after registration (right).

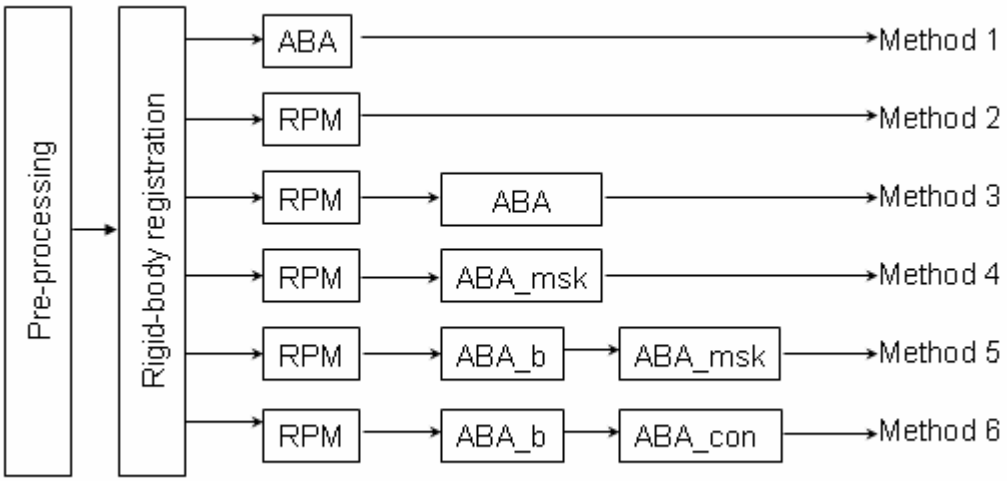

Fig. 31: Various combinations of algorithms that have been used in our validation study.

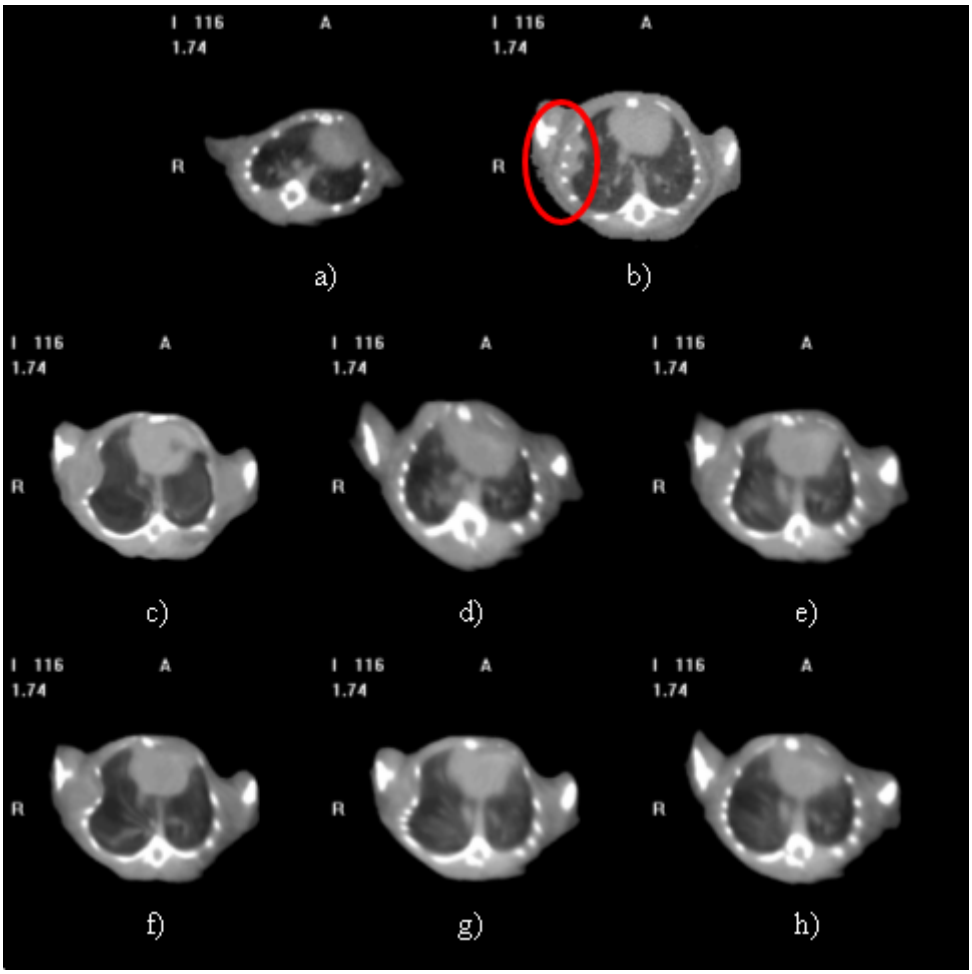

Fig. 32: One axial slice a) from the reference volume, b) the target volume, c) using ABA only, d) using RPM only, e) using RPM and ABA, f) using RPM and ABA with the mask, g) using RPM, ABA applied to bones, and ABA with the mask, and h) using RPM, ABA applied to bones, and the modified ABA.

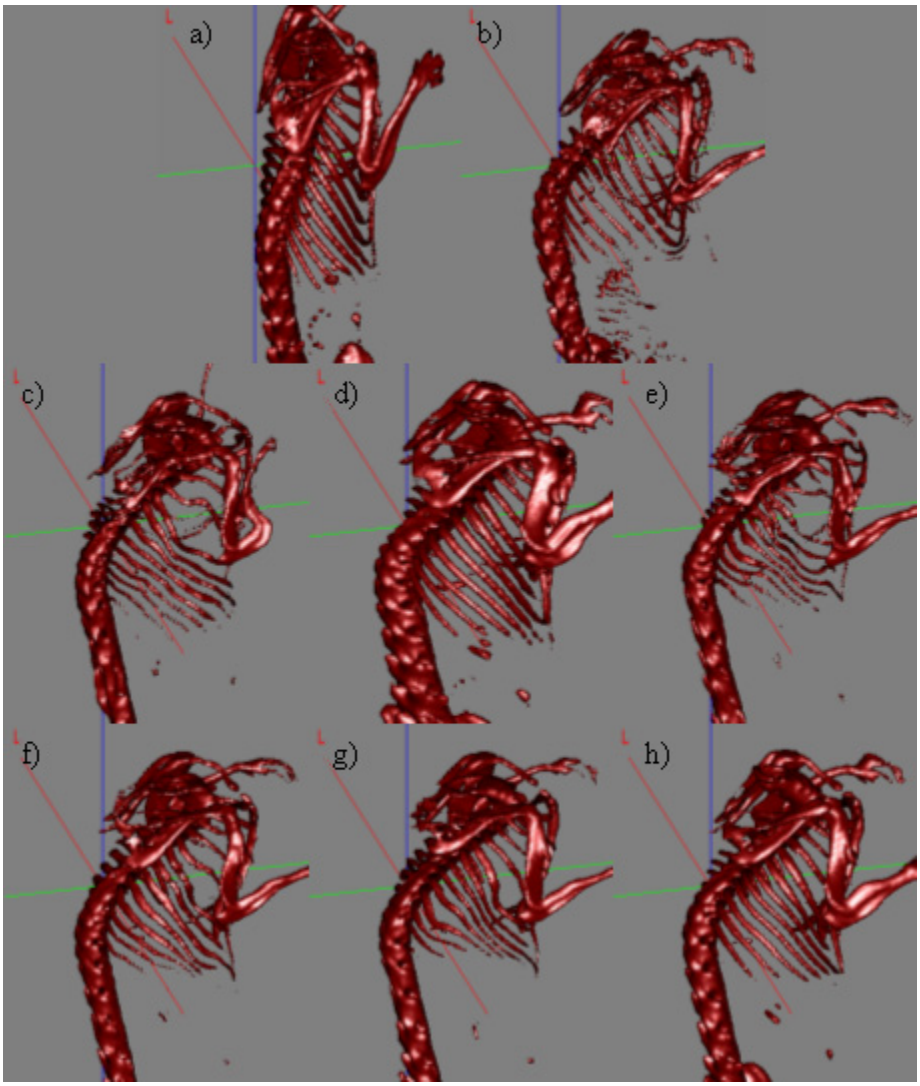

Fig. 33: The deformed skeleton from a) the reference and b) target volumes, c) using ABA only, d) using RPM only, e) using RPM and ABA, f) using RPM and ABA with the mask, g) using RPM, ABA applied to bones, and ABA with the mask, and h) using RPM, ABA applied to bones, and the modified ABA.

3.2 Quantitative Validation

The visual and qualitative validation of our approach presented in the last section indicate its potential for preventing the distortion of the skeletons when the entire image volumes are registered using an intensity-based method. To validate our algorithm quantitatively on both the skeletons and soft tissue structures, we use the same strategy we have used in the previous chapter.

Validation on bony structure

To examine the effect of the constrained algorithm on the registration of bony structures, the distance between each point on the transformed source skeleton surface and its closest point on the target skeleton surface is computed. This is done for Method 4 − 6 and results are compared. We have limited our comparison to these three methods because they all attempt to constrain the deformation of bony structures.

Table IV lists the mean distances obtained with the three methods for both intra- and inter-subjects (about 50,000 points/case are used to compute these averages). The results in Table IV show that all of these three methods lead to small errors (within 0.3mm). Surprisingly, the data in this table also show that the second method, which uses the ABA algorithm with the stiffness map after applying the RPM algorithm and the ABA algorithm to the bones, yields better results, than those obtained with the new method we propose. But, a closer look at the results shows that Method 5, while producing the smallest distance errors, also distorts the skeletons. This is shown in Fig. 34. This figure shows final skeletons obtained with method 5 (left column) and method 6 (right column). The top row shows a lower right leg. The bottom row shows a close up on

ribs. This figure shows that the mask approach we use in method 5 can not constrain the deformation of the bones and produces inaccurate transformations. The skeletons obtained with method 6 appear correct.

Table IV: The surface distances (mm) are computed for both the intra- and inter-subject registration tasks. For each data set, the distances between the transformed skeleton source surface and the closest point on the target surface are computed and averaged.

		ABA_msk	ABA_bone +ABA_msk	ABA_bone +ABA_con
Intra-subject	#01	0.3008	0.2794	0.292
	#02	0.329	0.3196	0.3188
	#03	0.1422	0.1254	0.1295
	#04	0.208	0.1786	0.2371
	Mean	0.245	0.2257	0.2443
Inter-subject	#01	0.4368	0.3859	0.4151
	#02	0.1769	0.16	0.1777
	#03	0.253	0.2205	0.2227
	#04	0.2054	0.1966	0.2323
	#05	0.2433	0.2072	0.2668
	#06	0.355	0.3137	0.3192
	#07	0.3255	0.2999	0.3721
	#08	0.233	0.202	0.2763
	#09	0.2496	0.2259	0.2898
	#10	0.33	0.2763	0.2829
	#11	0.2666	0.2431	0.2374
	#12	0.3314	0.3016	0.3237
	#13	0.3795	0.3504	0.3659
	#14	0.3168	0.2356	0.2177
	#15	0.2999	0.2807	0.3111
	#16	0.3734	0.3169	0.3723
	#17	0.337	0.3103	0.3655
	Mean	0.3008	0.2663	0.297

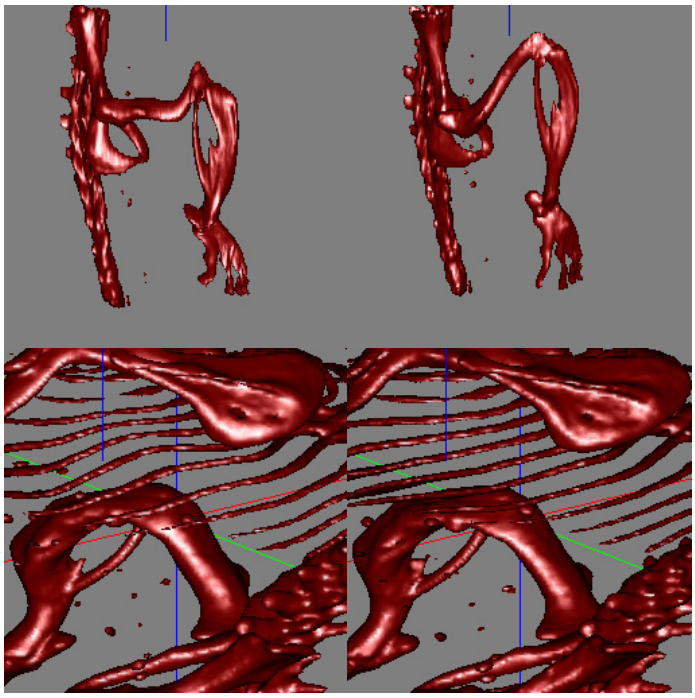

Fig. 34: Two examples of the deformed skeletons using Method 5 and 6 (left to right).

The purpose of methods 5 and 6 is the same: constrain the deformation of the bones to produce transformations that are physically correct. As shown in Fig. 34, method 6 appears to produce results that are better according to this criterion. To compare these two methods qualitatively, we measure the amount of bone distortion each of them produces. To do this, we evaluate for every bone voxel the value of the Jacobian determinant of the last transformation computed with methods 5 and 6. In the case of method 5, this is the transformation computed on the entire image with the ABA algorithm constrained with the skeleton mask. In the case of method 6, it is the transformation computed with the ABA algorithm and the new constraint we propose. In both cases, the bones should be deformed minimally and the Jacobian determinant should be close to one because the bones are rigid body structures. Fig. 35 shows the mean

values and the standard deviations of the Jacobian determinant obtained with these two methods. For the intra-subject data sets, the mean and standard deviation of the Jacobian determinant using methods 5 and 6 are 1.0216±0.1323 and 1.0003±0.0239, respectively. For the inter-subject, they are 1.0475±0.2296 and 1.0002±0.0214. These results confirm what has been observed visually, i.e., the proposed method is effective at constraining the deformation of the bones. While the mean values are close to each other, the standard deviations of the Jacobian determinant obtained with method 5 are substantially larger than those obtained with method 6, indicating that certain regions of the skeleton are deformed inappropriately when the former method is used.

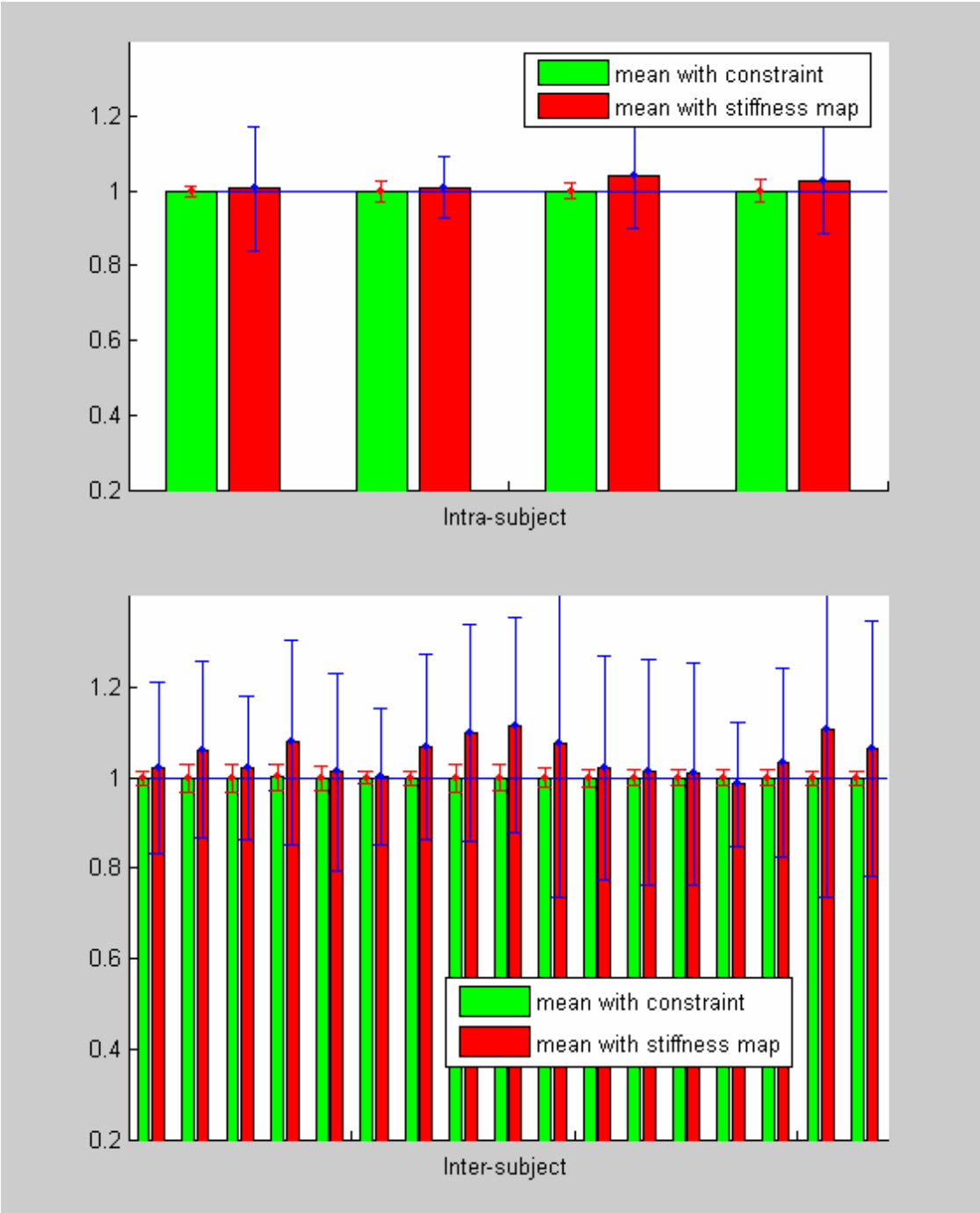

Fig. 35: The means and standard deviations of the Jacobian determinant for skeleton voxels obtained with different constraint schemes for both intra- and inter-subjects tasks.

Validation on soft tissues

Here, we have used the same approach as in the previous chapter to validate our method on soft tissues, except that we compare our automatic method to only one manual rater (rater 1). Following this approach, the heart, bladder and kidneys are segmented manually in the source and target images, respectively. The Dice similarity index is then computed for each structure to compare manual and automatic contours.

Table V lists the Dice values we have obtained for the longitudinal registration tasks, using the method described in Chapter III and the algorithm constrained with the scheme we propose in this chapter. The general trend these results show is that automatic and manual contours are in very good agreement with both methods but that the new constraint reduces the value of the Dice coefficient somewhat. As was the case in Chapter III, adding the extra step (i.e., using the MR image volume) improves the results.

Fig. 36 shows the Dice values obtained with the constrained algorithm for the 17 pairs of inter-subject mice data sets. Table VI shows the mean Dice values for all 17 inter-subject data sets for all four types of soft tissues, obtained with the two methods: the method in the previous chapter and the proposed constrained method. Again, we observe that the new constraint leads to slightly smaller Dice values for the soft tissue structures than the original algorithm presented in Chapter III.

Table V: Dice similarity values between manual and automatic contours obtained with the method described in Chapter III and with the new constraint scheme.

		Intra-subject				
		#1	#2	#3	#4	MEAN
Heart	Previous method	0.9040	0.8530		0.8930	0.8833
	without and with MR	0.9220	0.9200		0.9160	0.9193
	Constrained method	0.8227	0.8397		0.8455	0.8360
	without and with MR	0.9031	0.9147		0.919	0.9022
Left Kidney	Previous method	0.9150	0.8930	0.8820	0.8900	0.8950
	without and with MR	0.9090	0.9230	0.9040	0.9120	0.9120
	Constrained method	0.8941	0.8885	0.8982	0.8667	0.8869
	without and with MR	0.9078	0.9239	0.9143	0.9139	0.9150
Right Kidney	Previous method	0.8730	0.8840	0.8520	0.8860	0.8738
	without and with MR	0.9180	0.9330	0.8890	0.9230	0.9158
	Constrained method	0.8657	0.8899	0.8158	0.8401	0.8529
	without and with MR	0.9307	0.9327	0.8753	0.9149	0.9134
Bladder	Previous method	0.8120	0.8860	0.7100	0.8040	0.8030
	without and with MR	0.7730	0.9510	0.7650	0.8980	0.8468
	Constrained method	0.8492	0.8717	0.7327	0.8092	0.8157
	without and with MR	0.7657	0.9519	0.7832	0.8815	0.8456

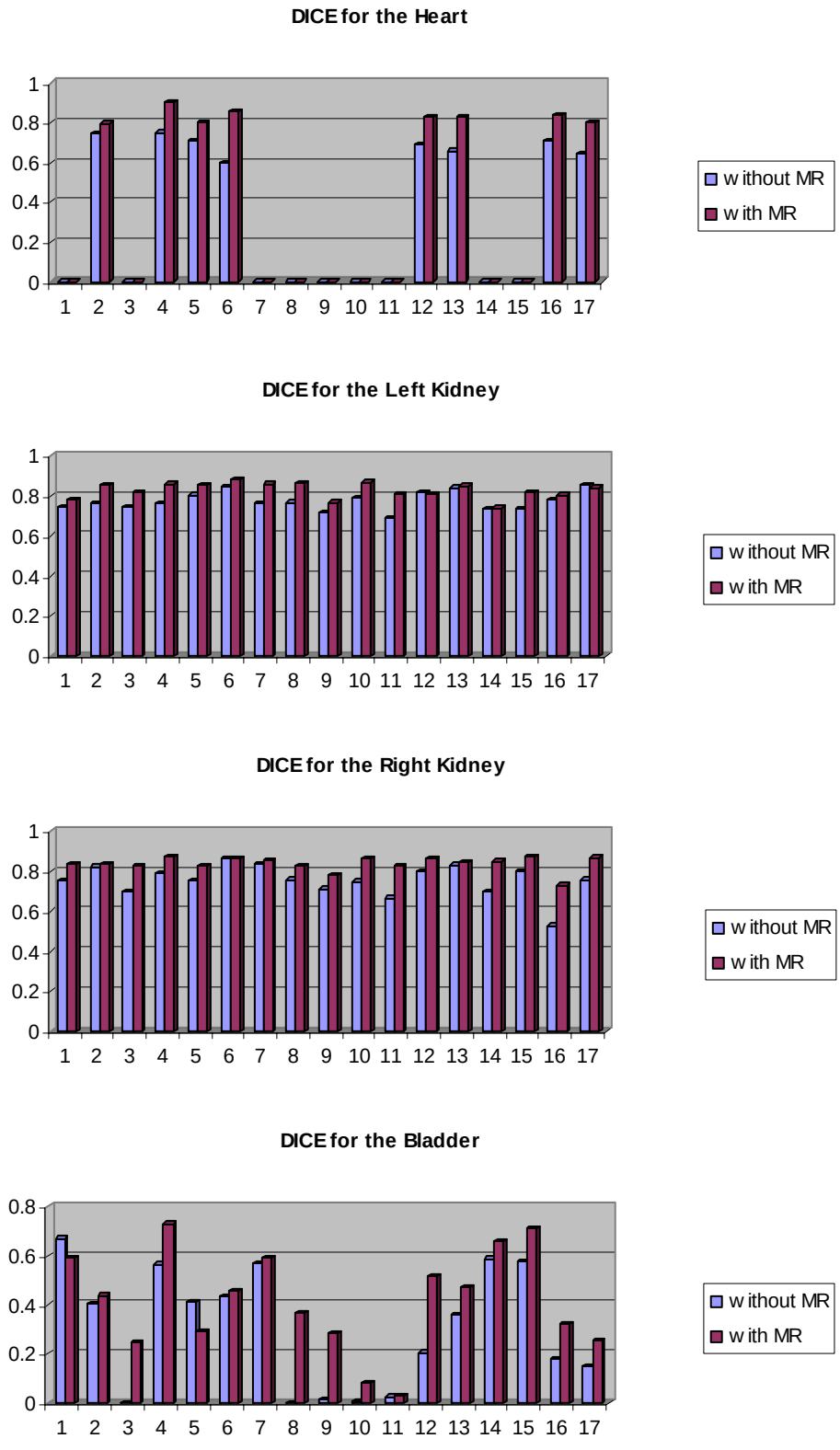

Fig. 36: Dice values for the inter-subject registration task after the proposed method and the extra step.

Table VI: Mean Dice coefficients for soft tissue structures for 17 data sets of inter-subject data sets. These results compare the method described in Chapter III and the constrained method proposed in this chapter.

		Inter-subject	
		Previous method	Contrained method
Heart	Proposed	0.64906	0.57388
	Extra	0.79989	0.77695
Left Kidney	Proposed	0.79958	0.77333
	Extra	0.83538	0.82813
Right Kidney	Proposed	0.78042	0.75319
	Extra	0.84662	0.83793
Bladder	Proposed	0.32232	0.30310
	Extra	0.39444	0.41392

4. Conclusion

In this chapter, we present a constrained automatic approach for the registration of articulated structures applicable to intra- and inter-subject registration problems. One rigid body registration and one non-rigid point matching algorithm are used to initialize an intensity based registration algorithm. The previously used intensity based algorithm (ABA) put control points on a regular grid. There is thus no guarantee that the control point will fall on bone voxels. Because of this, bony structures can be deformed in the same way as the soft tissue, which leads to unsatisfactory results. To overcome this weakness, we propose a modified ABA algorithm, in which a special constraint is introduced to prevent the transformation from deforming the bony structure inappropriately while registering the rest of the image volume as well as possible.

The results we have obtained illustrate typical compromises that have to be made when performing non-rigid registration tasks. The new constraint scheme we propose

essentially forces the bone to stay in place. By doing this, we limit the amount of soft tissue deformation the transformation can capture. Depending on the application, the value of the parameter λ, which was set to 1 in our experiments, could be adjusted to relax or emphasize the bone constraints. Another possibility, which has not yet been explored, is to increase the value of the threshold used to constrain the $c_i's$ (i.e., the coefficient of adjacent basis functions in the ABA algorithm). Doing so would produce transformations that are more elastic over the soft tissue regions while being constrained over the skeleton voxels. But, increasing the value of this threshold has one drawback. It reduces the regularity and overall smoothness of the transformation. The characteristics of a particular application will guide the choice of parameters. If, as is the case in the example shown earlier in this chapter, the purpose is to register images to measure tumor growth when the tumor is localized close to bony structures, the new constraint is important. If there is good contrast in the images to guide the registration process, the threshold used to constrain the value of the coefficients of adjacent basis functions can be raised. If, on the other hand, contrast is poor, the transformations will need to be regularized more and the value of this threshold will need to be reduced. Unfortunately, at this point there are no absolute rules to determine the optimal parameter values and a certain amount of experience is necessary to adjust these for specific applications. In our experience, however, once parameter values are determined for a specific problem and a specific type of images, these can be reused without adjustment. The new constraint we introduce also extends the range of applications for which intensity-based registration algorithms are useful.

CHAPTER V

SUMMARY AND FUTURE WORK

1. Summary

This dissertation presents several innovations in the area of small animal registration. We start with the problem of reconstructing 3D histological volumes from 2D histological slices. This is a complex process that involves a sequence of steps, each with its own challenges and difficulties. Our contributions start when the cross sections have been stained and have been placed on a glass plate. We have shown that the preparation process is such that contrast in the images changes from slice to slice. After a review of the literature, we have proposed a new method to normalize intensity across slices. We have shown on several volumes that this method is robust, automatic, and produces excellent results. But, 3D volumes reconstructed from 2D histological slices suffer from a number of defects that are caused by the slicing process. This is a well-documented problem and automatic solutions are not easy to develop for each individual case. Using our expertise in the area of non-rigid registration, we have proposed a solution that addresses the problem. Rather than attempting to improve each individual volume, we create a virtual volume using all the data sets we have. Because defects do not appear at the same location in each and every volume and because our non-rigid registration algorithm is capable of normalizing volumes accurately, we can produce a virtual volume in which the effect of these defects is attenuated. Our results have shown that with as few as four histological volumes we can produce one virtual volume that is substantially better than any of the volumes used to create it. The process we have

developed could easily be extended to study differences in populations. To accomplish this goal, one would need to create averages for each population, as we have done, and then register the population averages to each other. Information captured in the deformation fields could then reveal local differences between the populations due to, for instance, genetic alterations.

But, brain studies are only a small part of the studies being conducted with small animals. Studies that involve the entire body or parts of the body are common to monitor parameters such as response to therapy or growth. Registering these images brings a new set of challenges, and very little has been done in the area so far. As we have seen, registering small animal volumes requires registering volumes with articulated structures, i.e., rigid body structures the relative position of which can change over time. When dealing with inter-subject registration problems, one needs to develop methods, which not only change the shape of individual bones but also permit the registration of a series of bones that are in difference position, relative to each other. This is a complex problem and very little has been done in the area. To the best of our knowledge, our method is the first automatic method that permits the registration of skeletons fully automatically. But, skeletons are only a very small part of the entire volume and, ultimately, registering soft tissue structures is what is of interest. We have shown that using a sequence of steps in which we first register the skeletons to initialize an intensity-based registration algorithm leads to good results. But we have also shown that, because bones are small and do not weigh much in the similarity measure we use, our algorithms tend to produce results in which the skeletons are deformed inaccurately. In Chapter III, we use a constraint mechanism that allows us to adapt the mechanical properties of the transformation

spatially. This mechanism works very well for human data sets in which bones are large compared to the image resolution but less so for small animal images in which bones can be as small as a few pixels. In Chapter IV, we modify our similarity measure to produce transformations that constrain the displacement of the bones. Our results show that this constraint is effective and that the final skeletons we obtain are registered correctly. A direct application of this method is the measurement of tumor growth, when the tumor is located close to bony structures. Results shown in Chapter IV have demonstrated the difficulty non-rigid registration algorithms have with this problem. Because the tumor is not present in one of the volumes, the algorithm deforms normal tissue into a tumor to maximize the similarity between the images. We have shown that the constraint we propose in Chapter IV permits the registration of these images without erroneous displacement of the skeletons, thus facilitating the measurement of differences in longitudinal studies.

The results we have obtained in both Chapter III and IV show that the set of methods we have developed holds good promise for the automatic registration of small animal images both for longitudinal and inter-subject registration tasks. These results also show that accurate registration of soft tissues will, for the foreseeable future, require both CT and MR images. CT images do not have enough contrast and MR images alone are not sufficient because there is too much variation between the volumes. Non-rigid intensity-based algorithms need to be initialized to produce acceptable results. For head images, this is usually done with an affine transformation. For whole body images, affine transformations are insufficient. One solution is to compute an initial transformation manually. For instance, some points can be selected in both volumes and used to compute

a rough registration. The approach we propose requires acquiring an additional CT image but it has the distinct advantage of being automatic.

2. Future work

There is still plenty of room for further improvement. The two main algorithms used in this dissertation, the robust point matching algorithm and the adaptive bases algorithm, can be further developed to fit the characteristics and requirements of different modalities and applications.

Robust point matching is able to estimate both the correspondence and the nonlinear transformation between two sets of points. However, the algorithm only uses the spatial distance between two sets of points. More attributes could be added to compute the correspondence matrix, such as intensity, texture and other characteristic values. Hence, the correspondence matrix could become:

$$m_{ai} = \frac{1}{T}\exp\left(-\frac{(x_i - f(\upsilon_a))^T (x_i - f(\upsilon_a)) + \lambda (A(x_i) - A(f(\upsilon_a)))^T (A(x_i) - A(f(\upsilon_a)))}{2T}\right) \quad (21)$$

where *A()* denotes the attributes and λ balances two terms. The attributes can also be tailored to specific applications. For example, in the application of human breast cancer imaging, one attribute could be a biomechanical value, such as a stiffness property of breast tumors. One possible strategy to implement this scheme is to associate different values with different types of points. For example, assuming a breast tumor is harder than other soft tissues, such as adipose tissue in a breast, a larger value can be assigned to points on tumors, and a small value can be assigned to other points.

Similarly, the adaptive bases algorithm can be improved by adding more constraints. Currently, the constraint we are using is the mean displacement of the region of interest in the cost function. Future work includes designing more constraints for different requirements. One potential constraint is to preserve the tumor volume, because it is easy for the post-contrast MR breast images to shrink after it is registered to pre-contrast MR images. To maintain tumor volume constant is important for accurate registration. Similar work can be found in [97] and [98].

In addition to the improvement with respect to the algorithms, future work needs also to be done to apply, verify, and evaluate them on a larger number of images and evaluate its potential for a range of images acquired both for clinical and research purposes. One immediate and promising area of application that has been touched on but not explored fully is the registration and segmentation of head and neck images for the automatic segmentation of radio-sensitive structures. This is a lengthy procedure required for radiation therapy planning. The results we have shown in Chapter III suggest that our combination of point-based and intensity-based registration algorithms offer a viable solution.

REFERENCES

[1] M. Sonka and J. Michael Fitzpatrick, "Handbook of Medical Imaging, Volume 2: Medical Image Processing and Analysis," ISBN 0-8194-3622-4, SPIE, Belligham, WA, 1250 pages, (2000).

[2] J. V. Hajnal, J. V. Hajnal, "Medical Image Registration," ISBN-13: 9780849300646, 392 pages, CRC Press (2001).

[3] C. A. Pelizzari, G. T. Y. Chen, D. R. Spelbring, R. R. Weichselbaum, C. T. Chen, "Accurate three-dimensional registration of CT, PET, and/or MR images of the brain," J Comput Assist Tomogr, 13:20–26 (1989).

[4] E. L. Kramer, M. E. Noz, J. J. Sanger, A. J. Megibow, G. Q. Maguire, "CT-SPECT fusion to correlate radiolabeled monoclonal antibody uptake with abdominal CT findings," Radiology, 172:862–865 (1989).

[5] C. J. Henri, D. L. Collins, T. M. Peters, "Multimodality image integration for stereotactic surgical planning," Med Phys, 18:167–177 (1991).

[6] R. P. Woods, J. C. Mazziotta, S. R. Cherry, "MRI-PET registration with automated algorithm," J Comput Assist Tomogr, 17:536–546 (1993).

[7] P. A. van den Elsen and M. A. Viergever, "Automated CT and MR brain image registration using geometrical feature correlation," In Nuclear science symposium and medical imaging conference, 1827–1830 (1993).

[8] M. X. H. Yan, J. S. Karp, "Image registration of MR and PET based on surface matching and principal axes fitting," IEEE Med Imaging Conf, 4:1677–1681 (1994).

[9] L. Hui, B. S. Manjunath, and S. K. Mitra, "Registration of 3-D multimodality brain images by curve matching," Nuclear Science Symposium and Medical Imaging Conference, 3: 1744-1748 (1993).

[10] B. A. Ardekani, M. Braun, B. F. Hutton, I. Kanno, and H. Iida, "A fully-automatic multimodality image registration algorithm," J. Comput.Assist. Tomog., 19: 615–623 (1995).

[11] J. N. Yu, F. H. Fahey, H. D. Gage, "Intermodality retrospective image registration in the thorax," J Nucl Med. 36:2333–2338 (1995).

[12] W. M. Wells, P. Viola, H. Atsumi, S. Nakajima, and S. Kikinis, "Multi-modal volume registration by maximization of mutual information," Med. Image Anal, 1: 35–51 (1996).

[13] P. Viola and W. M. Wells III, "Alignment by maximization of mutual information," Int. J. Comput. Vision, 24(2): 137–154 (1997).

[14] F. Maes, A. Collignon, D. Vandermeulen, G. Marchal, and P. Suetens, "Multimodality image registration by maximization of mutual information,"IEEE Trans. Med. Imaging, 16:187–198 (1997).

[15] H. Pohjonen, P. Nikkinen, O. Sipila, J. Launes, E. Salli, O. Salonen, P. Karp, J. Ylä-Jääski, T. Katila1, and K. Liewendahl, "Registration and display of brain SPECT and MRI using external markers," Neuroradiology, 38:108–114 (1996).

[16] C. Pereault, C. Schvartz, H. Wampach, "Thoracic and abdominal SPECT-CT image fusion without external markers in endocrine carcinoma," J Nucl Med. 38:1234–1242 (1997).

[17] C. Studholme, D. L. G. Hill, and D. J. Hawkes, "Automated three-dimensional registration of magnetic resonance and positron emission tomography brain images by multiresolution optimization of voxel similarity measures," Med. Phys., 24(1): 25–35 (1997).

[18] C. R. Meyer, J. L. Boes, B. Kim, P. H. Bland, K. R. Zasadny, P. V. Kison,K. Koral, K. A. Frey, and R. L. Wahl, "Demonstration of accuracy and clinical versatility of mutual information for automatic multimodality image fusion using affine and thin-plate spline warped geometric deformations," Med. Image Anal., 1(3): 195–206 (1997).

[19] C. Chow, H. Lee and T. Lau, "Medical image registration and model construction using genetic algorithms," Proceedings of International Workshop on Medical Imaging and Augmented Reality, 174-179 (2001).

[20] N. Hayakawa, K. Uemura, K. Ishiwata, Y. Shimada, N. Ogi, and T. Nagaoka et al., "A PET-MRI registration technique for PET studies of the rat brain," Nucl. Med. Biol., 27:121–125 (2000).

[21] K. Rohr, H.S. Stiehl, R. Sprengel, T.M. Buzug, J.Weese, and M.H. Kuhn, "Landmark-based elastic registration using approximating thin-plate splines," IEEE Trans. on Medical Imaging, 20(6):526–534 (2001).

[22] J. P. W. Pluim, J. B. Maintz, M. A. Viergever, "Image Registration by Maximization of Combined Mutual Information and Gradient Information," IEEE Trans. Med. Imaging 19(8): 809-814 (2000).

[23] J. J. Vaquero, M. Desco, J. Pascau, A. Santos, I. Lee, J. Seidel, M. V. Green, "PET, CT and MR Image Registration of the Rat Brain and Skull," IEEE Trans Nucl Sci, 48(4): 1440-1445 (2001).

[24] D. Mattes, D. R. Haynor, H. Vesselle, T. K. Lewellen, and W. Eubank, "PET-CT image registration in the chest using free-form deformations," IEEE Transaction on Medical Imaging, 22(1):120–128 (2003).

[25] S. Periaswamy and H. Farid, "Elastic registration in the presence of intensity variations," IEEE Transactions on Medical Imaging, 22(7): 865-874 (2003).

[26] J. Mangin, V. Frouin, and B. Bendriem, "Nonsupervised 3D Registration of PET and MRI Data Using Chamfer Matching," Nuclear Science Symposium and Medical Imaging Conference, 2:1262-1264 (1993).

[27] M.H. Deverell, J.R. Salisbury, M.J. Cookson, J.G. Holman, E. Dykes, F. Whimster, "Three-dimensional reconstruction: methods of improving image registration and interpretation," Anal. Cell. Pathol. 5:253–263 (1993).

[28] A. Kreite (Ed.), "Visualization in Biomedical Microscopies: 3-D Imaging and Computer Applications," VCH, (1992).

[29] M. Rydmark, T. Jansson, C.-H. Berthold, T. Gustavsson, "Computer assisted realignment of light micrograph images from consecutive sections series of cat cerebral cortex," J. Microsc. 165:29–47 (1992).

[30] A. F. Goldszal, O. J. Tretiak, P. J. Hand, S. Bhasin, D. L. McEachron, "Three-dimensional reconstruction of activated columns from 2- [14C]deoxy-d-glucose data," Neuroimage 2:9–20 (1995).

[31] F. S. Cohen, Z. Yang, Z. Huang, J. Nissanov, "Automatic matching of homologous histological sections," IEEE Trans. Biomed. Engng 45(5):642–649 (1998).

[32] P.A. Kay, R.A. Robb, D.G. Bostwick, J.J. Camp, "Robust 3-D reconstruction and analysis of microstructures from serial histologic sections, with emphasis on microvessels in prostate cancer," in: K.H. Ho¨hne, R. Kikinis (Eds.), Visual. Biomed. Comput., Lecture Notes in Computer Science, 1131:129–134 (1996).

[33] A. Rangarajan, H. Chui, E. Mjolsness, S. Pappu, L. Davachi, P. Goldman-Rakic, J. Duncan, "A robust point-matching algorithm for autoradiograph alignment," Med. Image Anal. 1(4): 379–398(1997).

[34] A. li, W.S.I. and Cohen, F.S., "Registering coronal histological 2-D sections of a rat brain with coronal sections of a 3-D brain atlas using geometric curve invariants and B-spline representation," IEEE Trans. on Medical Imaging, 17(6): 957-966 (1998).

[35] S. Ourselin, A. Roche, G. Subsol, and X. Pennec, "Automatic Alignment of Histological Sections," In F. Pernus, S. Kovacic, H.S. Stiehl, and M.A. Viergever, editors, International Workshop on Biomedical Image Registration, WBIR'99, Bled (Slovénie), 1-13 (1999).

[36] S. Ourselin, A. Roche, G. Subsol, X. Pennec, N. Ayache, "Reconstructing a 3-D structure from serial histological sections," Image Vision Comput. 19 (1/2): 25-31 (2001).

[37] A. MacKenzie-Graham, E. Lee, I. D. Dinov, M. Bota, D. W. Shattuck, S. Ruffins, H. Yuan, F. Konstantinidis, A. Pitiot, Y. Ding, G. Hu, R. E.Jacobs and A. W. Toga, "A multimodal,multidimensional atlas of the C57BL/6J mouse brain," Journal of Anatomy, 204(2): 93-102 (2004).

[38] M.S. Mega, S.S. Chen, P.M. Thompson, R.P. Woods, T.J. Karaca, A.Tiwari, H.V. Vinters, G.W. Small, and A. W. Toga, "Mapping histology to metabolism: Coregistration of stained whole brain sections to premortem PET in Alzheimer's Disease," NeuroImage. 5: 147-153 (1997).

[39] P. M. Thompson, and A.W. Toga, "A surface-based technique for warping three dimensional images of the brain," IEEE Trans. Med. Imaging 15:1–16 (1996).

[40] S. Ourselin, E. Bardinet, D. Dormont, G. Malandain, A. Roche, N. Ayache, D. Tande, K. Parain, and J. Yelnik, "Fusion of Histological Sections and MR Images: Towards the Construction of an Atlas of the Human Basal Ganglia," In 4th International Conference on Medical Image Computing And Computer-Assisted Intervention (MICCAI'01), 2208:743-751 (2001).

[41] E. Bardinet, A.C.F Colchester, A. Roche, Y. Zhu, Y. He, S. Ourselin, B. Nailon, S.A. Hojjat, J. Ironside, S. Al-Sarraj, N. Ayache, and J. Wardlaw, "Registration of Reconstructed Post Mortem Optical Data with MR Scans of the Same Patient," In W.J. Niessen and M.A. Viergever, editors, 4th Int. Conf. on Medical Image Computing and Computer-Assisted Intervention (MICCAI'01), 2208: 957-965 (2001).

[42] E. Bardinet, S. Ourselin, D. Dormont, G. Malandain, D. Tandé, K. Parain, N. Ayache, and J. Yelnik, "Co-registration of histological, optical and MR data of the human brain," Medical Image Computing and Computer-Assisted Intervention (MICCAI'02), 2488:548-555 (2002).

[43] S. Gefen, O. Tretiak, J. Nissanov, "Elastic 3-D alignment of rat brain histological images," IEEE Transaction on Medical Imaging, 22(11):1480-1489 (2003).

[44] M. Mallar Chakravarty, G. Bertrand, M. Descouteaux, A. F. Sadikot and D. L. Collins, "The Creation of a Brain Atlas for Image Guided Neurosurgery Using Serial Histological Data," MICCAI , 343-350 (2003).

[45] M. Auer, P. Regitnig, Gerhard Holzapfel, "An automatic nonrigid registration for stained histological sections," IEEE Transactions on Image Progressing 14(4): 475-486 (2005).

[46] V. Arsigny, X. Pennec, N Ayache, "Polyrigid and polyaffine transformations: a novel geometrical tool to deal with non-rigid deformations - application to the registration of histological slices," Med Image Anal. 9(6):507-23 (2005).

[47] O. Camara, G. Delso, I. Bloch, "Free Form Deformations Guided by Gradient Vector Flow: A Surface Registration Method in Thoracic and Abdominal PET-CT Applications," WBIR 2003, 2717:224-233 (2003).

[48] D. Rueckert, L. Sonoda, C. Hayes, D. Hill, M. Leach and D. Hawkes, "Non-rigid registration using free-form deformations: application to breast MR images," IEEE Trans. Med. Imaging, 18: 712–21 (1999).

[49] J. A. Little, D. L. G. Hill, and D. J. Hawkes, "Deformations Incorporating Rigid Structures," Computer Vision and Image Understanding, 66(2): 223-232 (1997).

[50] MA Martin-Fernandez, E Munoz-Moreno, M Martin-Fernandez, C Alberola-Lopez, "Articulated registration: Elastic registration based on a wire-model," Medical Imaging 2005: Image Processing, SPIE, 182-191 (2005).

[51] V. Arsigny, X. Pennec, and N. Ayache, "Polyrigid and Polyaffine Transformations: A New Class of Diffeomorphisms for Locally Rigid or Affine Registration," Proc. of MICCAI'03, 829-837 (2003).

[52] X. Papademetris, D.P. Dione, L.W. Dobrucki, L.H. Staib, A.J. Sinusas, "Articulated Rigid Registration for Serial Lower-Limb Mouse Imaging," MICCAI'05, pp. 919-926 (2005).

[53] RP Woods, SR Cherry, JC Mazziotta, "Rapid automated algorithm for aligning and reslicing PET images," Journal of Computer Assisted Tomography, 16:620-633 (1992).

[54] G. Malandain, É. Bardinet, K. Nelissenc and W. Vanduffel, "Fusion of autoradiographs with an MR volume using 2-D and 3-D linear transformations," NeuroImage, 23:111-127 (2004).

[55] http://www.mbl.org/tutorials/MBLTrainingManual/index.html.

[56] B. M. Dawant, S. Pan, and R. Li , "Robust Segmentation of Medical Images Using Geometric Deformable Models and a Dynamic Speed Function," Lecture Notes in Computer Science (LNCS 2208) Medical Image Computing and Computer-assisted Intervention, 1040-1047(2001).

[57] W. Press, S. Teukolsky, W. Vetterling, and B. Flannery, "Numerical Recipes in C," The Art of Scientific Computing, 2nd ed. Cambridge, U.K.: Cambridge Univ. Press, 1994.

[58] A. Guimond, J. Meunier, and J.P. Thirion, "Average brain models: A convergence study," Comp. Vision Image Understand, 77: 192–210 (2000).

[59] G. K. Rohde, A. Aldroubi, and B. Dawant, "The adaptive bases algorithm for intensity-based nonrigid image registration," IEEE Trans Med Imaging, 22 (11): 1470-1479 (2003).

[60] V. Duay, P. D'Haese, R Li, B M. Dawant, "Non-Rigid Registration Algorithm With Spatially Varying Stiffness Properties," ISBI, 408-411 (2004).

[61] P. A. Yushkevich, B. Avants, L. Ng, M. Hawrylycz, P.D. Burstein, H. Zhang, and J.C. Gee, "3D Mouse Brain Reconstruction from Histology Using a Coarse-to-Fine Approach", Proc. Third International Workshop of WBIR, 230-237 (2006).

[62] A. P. Zijdenbos, B. M. Dawant, R. A. Margolin, and A. C. Palmer, "Morphometric analysis of white matter lesions in MR images: Method and validation," IEEE Trans. Med. Imag., 13(4): 716–724 (1994).

[63] J. Dauguet, J.-F. Mangin, T. Delzescaux, and V. Frouin, "Robust inter-slice intensity normalization using histogram scale-space analysis," Medical Image Computing and Computer Assisted Intervention, 3216:242-249 (2004).

[64] C. L. Brumwell, T. Curran, "Developmental mouse brain gene expression maps," J Physiol. 2006 Sep 1;575(Pt 2):343-6 (2006).

[65] S. E. Koester, T. R. Insel, "Mouse maps of gene expression in the brain," Genome Biol. 8(5):212 (2007).

[66] Lein ES, Hawrylycz MJ, Ao N, Ayres M, Bensinger A, et al., "Genome-wide atlas of gene expression in the adult mouse brain," Nature. 2007 Jan 11; 445(7124):168-76 (2007).

[67] E. Chan, N. Kovacevíc, S. K. Ho, R. M. Henkelman, J. T. Henderson, "Development of a high resolution three-dimensional surgical atlas of the murine head for strains 129S1/SvImJ and C57Bl/6J using magnetic resonance imaging and micro-computed tomography," Neuroscience. 2007 Jan 19; 144(2):604-15 (2007).

[68] Y. Ma, P. R. Hof, S. C. Grant, S. J. Blackband, R. Bennett, L. Slatest, M. D. McGuigan, Benveniste H., "A three-dimensional digital atlas database of the adult C57BL/6J mouse brain by magnetic resonance microscopy," Neuroscience, 135(4):1203-15 (2005).

[69] A. MacKenzie-Graham, E. F. Lee, I. D. Dinov, M. Bota, D. W. Shattuck, S. Ruffins, H. Yuan, F. Konstantinidis, A. Pitiot, Y. Ding, G. Hu, R. E. Jacobs, A. W. Toga, "A multimodal, multidimensional atlas of the C57BL/6J mouse brain," J Anat. 204(2):93-102 (2004).

[70] J. Cai, J.C.H. Chu, D. Recine, M. Sharma, C. Nguyen, R. Rodebaugh, V. Saxena, and A. Ali, "CT and PET Lung Image Registration and Fusion in Radiotherapy Treatment Planning Using Chamfer Matching Method," Int J Radiat Oncol Biol Phys. 43, 883–891 (1999).

[71] X. Papademetris, A. Jackowski, R. T. Schultz, L. H. Staib, and J. S. Duncan, "Integrated intensity and point-feature nonrigid registration," Proc. MICCAI'04, 763-770 (2004).

[72] A. du Bois d'Aische, M. De Craene, B. Macq, S.K. Warfield, "An articulated registration method," IEEE International Conference on Image Processing (ICIP), I-21-4 (2005).

[73] H. J. Johnson, and G. E. Christensen, "Consistent Landmark and Intensity-based Image Registration," IEEE Trans. Med. Imaging 21(5): 450-461 (2002).

[74] H. Chui and A. Rangarajan, "A new point matching algorithm for non-rigid registration," Computer Vision and Image Understanding, 114-141 (2003).

[75] S. Gold, A. Rangarajan, C.P. Lu, S. Pappu, E. Mjolsness, "New algorithms for 2D and 3D point matching: pose estimation and correspondence," Pattern Recognition, 31 (8), 1019-1031 (1998).

[76] Z. Wu , "Multivariate compactly supported positive definite radial functions," Adv. Comput. Math. 4: 283-292 (1995).

[77] D. J. Burr, "A dynamic model for image registration," Comp. Graph.Image Processing, 15(2): 102-112 (1981).

[78] M. Baiker, J. Milles, A.M. Vossepoel, I. Que, E.L. Kaijzel, C.W.G.M. Lowik, J.H.C. Reiber, J. Dijkstra and B.P.F. Lelieveldt, "Fully automated whole-body registration in mice using articulated skeleton atlas," IEEE International Symposium on Biomedical Imaging (ISBI): From Nano to Macro, 728-731 (2007).

[79] C. Studholme, D.L.G. Hill and D.J. Hawkes, "An overlap invariant entropy measure of 3D medical image alignment," Pattern Recognition, 32(1): 71–86 (1999).

[80] J. J. Bartko, "Measurement and reliability: Statistical thinking considerations," Schizophrenia Bullet., 17(3): 483-489 (1991).

[81] X. Li, T. E. Peterson, J. C. Gore, B. M. Dawant, "Automatic Registration of Whole Body Serial Micro CT Images with a Combination of Point-based and Intensity-based Registration Techniques," IEEE International Symposium on Biomedical Imaging: From Nano to Macro, 454-457 (2006).

[82] X. Li, T. E. Peterson, J. C. Gore, B. M. Dawant, "Automatic Inter-Subject Registration of Whole Body Images," Third International Workshop on Biomedical Image Registration (WBIR'06), 18-25 (2006).

[83] M. Staring, S. Klein, and J. P. W. Pluim, "Nonrigid Registration Using a Rigidity Constraint," Proc. of SPIE Medical Imaging, 6144:614413 (2006).

[84] D. Ruan, J. A. Fessler, M. Roberson, J. Balter, and M. Kessler, "Nonrigid Registration Using Regularization that Accomodates Local Tissue Rigidity," Proc. of SPIE Medical Imaging, 6144: 614412 (2006).

[85] X. Papademetris , P. Shkarin, L. H. Staib, and K. L. Behar, "Regional Whole Body Fat Quantification in Mice," IPMI 2005, LNCS 3565: 369-380 (2005).

[86] N.A. Bock, N. Kovacevic, T.V. Lipina, J.C. Roder, S.L. Ackerman, R.M. Henkelman, "InVivo Magnetic Resonance Imaging and Semi-Automated Image Analysis Extend the Brain Phenotype for cdf/cdf Mice," J. Neuroscience, 26:4455-4459 (2006).

[87] J. P. Thirion, "Image matching as a diffusion process: an analogy with Maxwell's demons," Medical Image Analysis, 2(3):243-60 (1998).

[88] A. Guimond, A. Roche, N. Ayache, and J. Meunier, "Three-dimensional multimodal brain warping using the demons algorithm and adaptive intensity corrections," IEEE Trans on Medical Imaging, 20(1):58-69 (2001).

[89] G. E. Christensen and H. J. Johnson, "Consistent image registration," IEEE Trans. Med. Imag., 20: 568–582 (2001).

[90] P. Hellier, C. Barillot, E. Mémin, and P. Pérez, "Hierarchical estimation of a dense deformation field for 3-D robust registration," IEEE Trans. Med. Imag., 20(5): 388–402 (2001).

[91] D. Rueckert, F. Frangi, and J. A. Schnabel, "Automatic construction of 3D statistical defomation models using nonrigid registration," in Proc. MICCAI'01, 2001, pp. 77–84.

[92] R. Bajcsy and S. Kovacic, "Multiresolution elastic matching," Comput. Vis., Graph., Image Processing, vol. 46, pp. 1–21 (1989).

[93] C. Davatzikos, "Spatial transformation and registration of brain images using elastically deformable models," Comput. Vis. Image Understanding, vol. 66, no. 2, pp. 207–222 (1997).

[94] J. C. Gee, M. Reivicj, and R. Bajcsy, "Elastically deforming 3-D atlas to match anatomical brain images," J. Comput. Assist. Tomogr., vol. 17, no. 2, pp. 225–236 (1993).

[95] M. Bro-Nielsen and C. Gramkow, "Fast fluid registration of medical images," in Proc. Visualization in Biomedical Computing, LNCS, 1131: 267–276 (1996).

[96] G. Christensen, R. Rabbit, and M. I. Miller, "Deformable templates using large deformation kinematics," IEEE Trans. Image Processing, vol. 5, pp. 1435–1447 (1996).

[97] T. Rohlfing, C. R. Jr. Maurer, D. A. Bluemke, M. A. Jacobs, "Volume-preserving nonrigid registration of MR breast images using free-form deformation with an incompressibility constraint," IEEE Trans Med Imaging;22:730–41 (2003).

[98] C. Tanner, J. A. Schnabel, A. Degenhard, A. D. Castellano-Smith, C. Hayes, M. O. Leach, et al. "Validation of volumepreserving non-rigid registration: application to contrastenhanced MR-mammography," Proceedings of MICCAI 2002, Lecture Notes in Computer Science; 2489:307–14 (2002).

[99] J. West, J. M. Fitzpatrick, M. Y. Wang, B. M. Dawant, C. R. Maurer, Jr., R. M. Kessler, R. J. Maciunas, et al., "Comparison and evaluation of retrospective intermodality image registration techniques," Journal of Computer Assisted Tomography 21, 554-566 (1997).